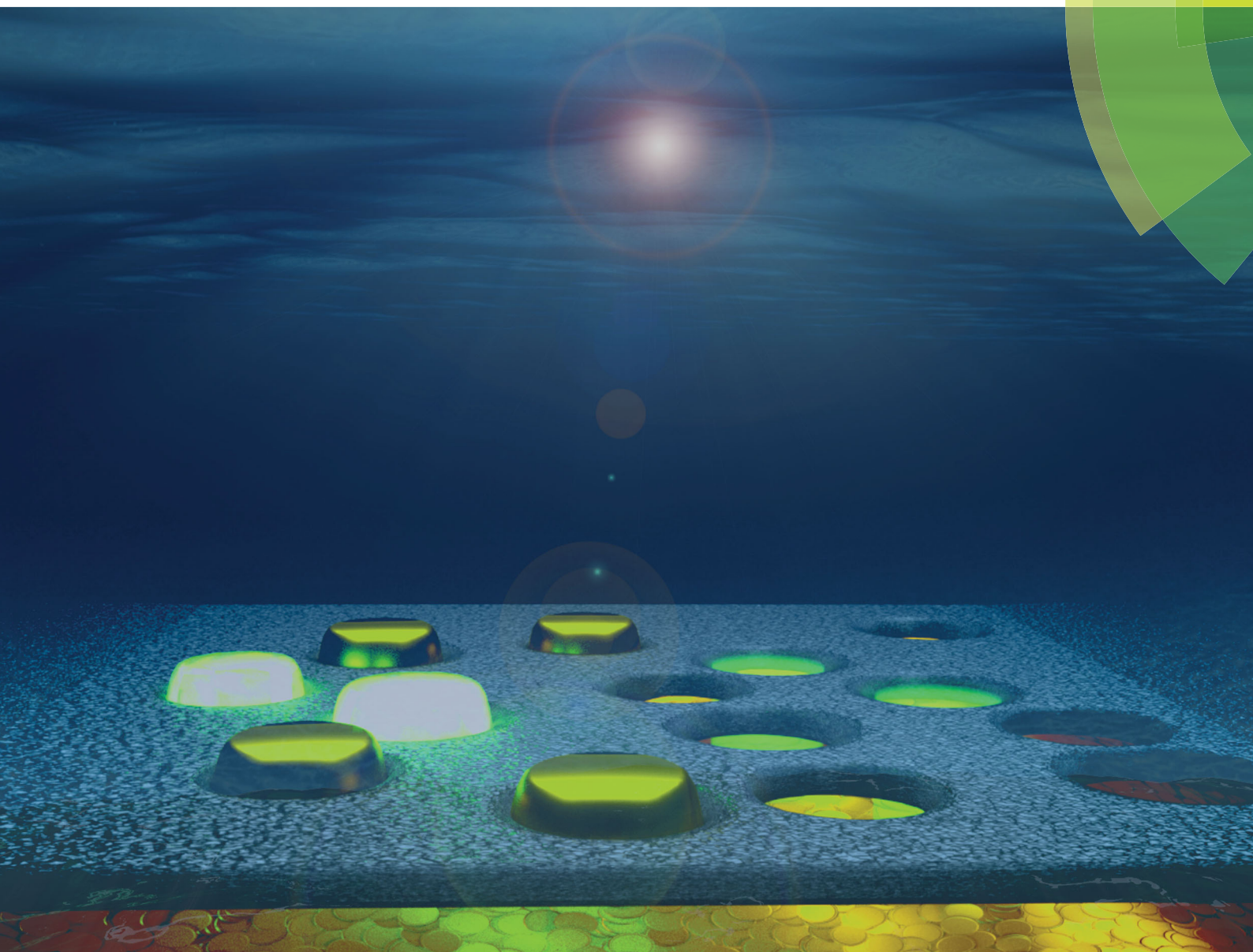


Chem Soc Rev

Chemical Society Reviews

rsc.li/chem-soc-rev



ISSN 0306-0012




REVIEW ARTICLE
Nam-Joon Cho *et al.*
Nanoplasmonic sensors for biointerfacial science



Cite this: *Chem. Soc. Rev.*, 2017, 46, 3615

Nanoplasmonic sensors for biointerfacial science

Joshua A. Jackman,^{†ab} Abdul Rahim Ferhan^{†ab} and Nam-Joon Cho  ^{*abc}

In recent years, nanoplasmonic sensors have become widely used for the label-free detection of biomolecules across medical, biotechnology, and environmental science applications. To date, many nanoplasmonic sensing strategies have been developed with outstanding measurement capabilities, enabling detection down to the single-molecule level. One of the most promising directions has been surface-based nanoplasmonic sensors, and the potential of such technologies is still emerging. Going beyond detection, surface-based nanoplasmonic sensors open the door to enhanced, quantitative measurement capabilities across the biointerfacial sciences by taking advantage of high surface sensitivity that pairs well with the size of medically important biomacromolecules and biological particulates such as viruses and exosomes. The goal of this review is to introduce the latest advances in nanoplasmonic sensors for the biointerfacial sciences, including ongoing development of nanoparticle and nanohole arrays for exploring different classes of biomacromolecules interacting at solid–liquid interfaces. The measurement principles for nanoplasmonic sensors based on utilizing the localized surface plasmon resonance (LSPR) and extraordinary optical transmission (EOT) phenomena are first introduced. The following sections are then categorized around different themes within the biointerfacial sciences, specifically protein binding and conformational changes, lipid membrane fabrication, membrane–protein interactions, exosome and virus detection and analysis, and probing nucleic acid conformations and binding interactions. Across these themes, we discuss the growing trend to utilize nanoplasmonic sensors for advanced measurement capabilities, including positional sensing, biomacromolecular conformation analysis, and real-time kinetic monitoring of complex biological interactions. Altogether, these advances highlight the rich potential of nanoplasmonic sensors and the future growth prospects of the community as a whole. With ongoing development of commercial nanoplasmonic sensors and analytical models to interpret corresponding measurement data in the context of biologically relevant interactions, there is significant opportunity to utilize nanoplasmonic sensing strategies for not only fundamental biointerfacial science, but also translational science applications related to clinical medicine and pharmaceutical drug development among countless possibilities.

Received 30th June 2016

DOI: 10.1039/c6cs00494f

rsc.li/chem-soc-rev

1. Introduction

Improving the real-time detection and characterization of biomacromolecules (*e.g.*, viruses,¹ exosomes,² liposomes,³ and proteins⁴) represents an important sensing goal with broad implications for a wide range of applications from healthcare diagnostics^{5–9} and drug discovery^{10–12} to environmental monitoring^{13,14} and food safety.^{15,16} One of the most promising approaches involves detection of biomacromolecules at solid–liquid interfaces, for which several ultrasensitive techniques have been established and are leading to commercial technologies that are capable of molecular detection down to extremely low analyte concentrations.¹⁷ Indeed, detection

strategies based on profiling biomacromolecules at solid–liquid interfaces are compatible with a wide range of surface-sensitive measurement techniques and can be coupled with microfluidics for minimal sample consumption.^{18,19} The sensor substrate can also be functionalized through various surface chemistries^{20–24} in order to increase detection specificity and sensitivity, either by promoting specific binding of the target analyte or by preventing nonspecific binding of interfering molecules based on molecular or steric features.^{25–27} Altogether, the detection of biomacromolecules at solid–liquid interfaces is a rapidly evolving field with a multitude of available sensor technologies.^{28,29}

As detection performances continue to improve through various established surface functionalization techniques and measurement strategies, there are growing opportunities to develop sensing technologies that go beyond relatively straightforward detection and enable more complex, quantitative measurement capabilities across the biointerfacial sciences. Understanding the dynamic behavior of adsorbed biomacromolecules at solid–liquid interfaces has long been recognized as an important goal of biological surface

^a School of Materials Science and Engineering, Nanyang Technological University, Singapore, 639798, Singapore. E-mail: njcho@ntu.edu.sg

^b Centre for Biomimetic Sensor Science, Nanyang Technological University, Singapore, 637553, Singapore

^c School of Chemical and Biomedical Engineering, Nanyang Technological University, Singapore, 637457, Singapore

[†] These authors contributed equally to this work.

science.^{30,31} In turn, a vast array of label-free acoustic and optical sensing techniques have been developed in order to characterize the mass and conformational properties of adsorbed biomacromolecules on a variety of surfaces.³² The most famous example is the surface plasmon resonance (SPR) biosensor, which was first commercialized by Biacore (and later acquired by GE Healthcare) and utilizes optical sensing principles to detect biomacromolecules in fundamental and applied research and clinical settings.³³ From a broader perspective, both acoustic and optical sensors have strong merits and provide complementary information about adsorbate properties.

Acoustic sensors such as the quartz crystal microbalance with dissipation (QCM-D) monitoring detect not only adsorbed biomacromolecules but also hydrodynamically-coupled solvent and can provide comprehensive information about the mass and viscoelastic properties of an adsorbate, which can to a certain extent be

correlated with conformational properties.^{34–36} However, the measurement response is sensitive to the coupled biomolecular and solvent mass, which is not directly proportional to the number of bound biomolecules.³⁷ Furthermore, hydrodynamic effects prove challenging for data interpretation,^{38,39} as reported in numerous examples of rigid nanoparticles.^{40–43} In addition, the conventional penetration depth of the probing volume for acoustic sensors is typically quite high (100–300 nm), which is approximately one order of magnitude greater than the length scale of biomacromolecules such as proteins.^{44,45} Collectively, these factors lead to difficulty in resolving the shape and conformational properties of adsorbed biomacromolecules because there is significant contribution from water trapped within the interior of the adsorbent (internal hydration) as well as water coupled externally to the adsorbate (external hydration) and there is a mismatch between the length scales of conventional biomacromolecules and the surface sensitivity of the QCM-D measurement approach.³⁷

On the other hand, evanescent optical sensors can extract the dry mass of adsorbates by directly measuring the total number of adsorbed molecules on planar noble metal surfaces within a relatively large probing volume.⁴⁶ While this approach may lead to excellent detection sensitivity, the capability to obtain information about conformational changes within or shape deformation of adsorbed biomacromolecules is limited.^{47,48} This challenge is due to the measurement principle which relies on refractive index changes near the metal surface. With a large penetration depth that typically extends to around 100–400 nm above the metal surface,^{49,50} the recorded shifts in the refractive index may not exclusively originate from molecules at the interface and, even so, will hardly be sensitive to the shape of the adsorbed biomacromolecules.^{51,52} Likewise, emerging technologies such as interferometric scattering can detect and track single particles, but only provide limited structural information.^{1,53,54} Collectively, these points highlight the need for innovative, highly surface-sensitive measurement approaches that can be utilized for applications across the biointerfacial sciences.



Joshua A. Jackman

Joshua A. Jackman is a Research Fellow in the group of Prof. Nam-Joon Cho at the School of Materials Science and Engineering, Nanyang Technological University, and is also affiliated with the Stanford University School of Medicine. He received his BS degree in Chemistry from the University of Florida and PhD degree in Materials Science and Engineering from Nanyang Technological University. He has received fellowships from the Arnold and Mabel Beckman Foundation, the National Science Foundation, and the American Liver Foundation. His research interests lay at the interface of materials science and biotechnology towards developing infectious disease diagnostics and therapeutics.

Joshua A. Jackman is a Research Fellow in the group of Prof. Nam-Joon Cho at the School of Materials Science and Engineering, Nanyang Technological University, and is also affiliated with the Stanford University School of Medicine. He received his BS degree in Chemistry from the University of Florida and PhD degree in Materials Science and Engineering from Nanyang Technological University. He has received fellowships from the Arnold and Mabel Beckman Foundation, the National Science Foundation, and the American Liver Foundation. His research interests lay at the interface of materials science and biotechnology towards developing infectious disease diagnostics and therapeutics.



Abdul Rahim Ferhan

Abdul Rahim Ferhan is a Research Fellow in the Engineering in Translational Science Group at the Centre for Biomimetic Sensor Science of Nanyang Technological University (NTU). He received his BEng degree in Chemical and Biomolecular Engineering and PhD degree in Biomedical Engineering from the School of Chemical and Biomedical Engineering, NTU. His research focuses on the development and application of novel nanoplasmonic sensing platforms for biomedical diagnostics and fundamental investigations into biomolecular interactions.

Abdul Rahim Ferhan is a Research Fellow in the Engineering in Translational Science Group at the Centre for Biomimetic Sensor Science of Nanyang Technological University (NTU). He received his BEng degree in Chemical and Biomolecular Engineering and PhD degree in Biomedical Engineering from the School of Chemical and Biomedical Engineering, NTU. His research focuses on the development and application of novel nanoplasmonic sensing platforms for biomedical diagnostics and fundamental investigations into biomolecular interactions.



Nam-Joon Cho

Nam-Joon Cho is Nanyang Associate Professor in the School of Materials Science and Engineering at Nanyang Technological University and Deputy Director of the Nanyang Institute of Technology in Health and Medicine. A recipient of the National Research Foundation Fellowship in Singapore, he received his PhD degree in Chemical Engineering from Stanford University, and completed a postdoctoral fellowship at the Stanford University School of Medicine. His research focuses on engineering artificial lipid membrane and tissue platforms to probe biological systems, and to develop enhanced therapeutic and drug delivery options that more effectively target infectious diseases, inflammatory disorders, and cancer.

Nam-Joon Cho is Nanyang Associate Professor in the School of Materials Science and Engineering at Nanyang Technological University and Deputy Director of the Nanyang Institute of Technology in Health and Medicine. A recipient of the National Research Foundation Fellowship in Singapore, he received his PhD degree in Chemical Engineering from Stanford University, and completed a postdoctoral fellowship at the Stanford University School of Medicine. His research focuses on engineering artificial lipid membrane and tissue platforms to probe biological systems, and to develop enhanced therapeutic and drug delivery options that more effectively target infectious diseases, inflammatory disorders, and cancer.

Towards this goal, nanoplasmonic sensor devices have demonstrated strong promise for addressing this need.^{55–57} The excitation of metallic nanostructures by light can lead to various optical phenomena, including localized surface plasmon resonance (LSPR)^{58,59} and extraordinary optical transmission (EOT),^{60–62} in some cases with tightly confined evanescent fields (<20 nm) that are highly sensitive to changes in the local refractive index. In the biosensing field, these features have been widely exploited for ultrasensitive detection of analytes,^{63,64} even reaching down to the single-molecule level.^{65–67} At the same time, the capabilities of surface-based nanoplasmonic sensors beyond conventional detection schemes are still emerging, with great potential for enhanced, quantitative measurement capabilities across the biointerfacial sciences. Indeed, the high surface-sensitivity of nanoplasmonic sensors couples well with the size of medically important biomacromolecules such as viruses and exosomes. With better control over the fabrication of nanoplasmonic transducer arrays on solid supports and greater understanding of the corresponding optical phenomena, there is rich potential for exploiting these measurement techniques in order to not only interrogate the structure and function of adsorbed biomacromolecules, but also apply this knowledge to develop improved sensors and diagnostics.

The goal of this review is to introduce the latest advances in nanoplasmonic sensors for the biointerfacial sciences, including ongoing developments for different classes of biomacromolecules and biological nanoparticles (*e.g.*, viruses, exosomes, and vesicles) interacting at solid–liquid interfaces. Although there have been several published review articles discussing the utilization of nanoplasmonic devices in biosensing applications, most of these articles

principally focus on the design aspects of nanoplasmonic sensing substrates, including detection sensitivity and integration of additional functionalities.^{57,68–78} A comprehensive review which discusses nanoplasmonic sensor applications across the biointerfacial sciences remains elusive, and we seek to fill this gap here. In particular, we discuss these ongoing developments in the context of different nanoplasmonic sensing strategies and advanced measurement capabilities, focusing on not only what has been achieved thus far but also what is possible to achieve in the near future. We begin by outlining the measurement principles of nanoplasmonic sensing based on the LSPR and EOT optical phenomena, and comparing the merits of these two sensing approaches. Then, we critically present recent examples of how nanoplasmonic sensors are being utilized across a wide range of biointerfacial science topics, including protein binding and conformational changes, lipid membrane fabrication, membrane–protein interactions, exosome and virus detection and analysis, and nucleic acid conformational and binding analysis. The scope of these examples includes fundamental scientific investigations as well as medical and biotechnological applications. Finally, we discuss the rich potential of nanoplasmonic sensors in the biointerfacial sciences as well as important needs, including the development of commercial sensors for widespread use with standardized outputs and analytical models for data interpretation in the context of biological systems. Considering the rapid progress of this field over the past few years, there are excellent growth prospects for nanoplasmonic sensing strategies to become a key part of not only fundamental biointerfacial science, but also translational science applications.

Box 1. Why nanoplasmonic sensors?

The interaction of light with noble metal surfaces has long been utilized for a wide range of sensing applications.^{56,63,79,80} When incident light excites a metal surface, plasmon resonances arise from the collective oscillation of free electrons in the conduction band of a metal. These coherent oscillations are known as surface plasmons (SPs), and contribute to one or more of several slightly varied optical phenomena depending on the geometry of the sensor surface and related factors.⁸¹ The SPR technique was the first example of using SPs for biosensing applications.^{82,83} Conventionally, SPR measurements are conducted on thin metal films and excitation gives rise to propagating SPs, which are electromagnetic waves that are bound at the sensor surface (the metal–dielectric interface) and the corresponding electromagnetic field is highly sensitive to the refractive index of the surrounding medium.^{49,84,85} As a result, SPR measurements can detect analytes with very low limits of detection.⁸⁶ At the same time, as nanofabrication capabilities improve, there has been further exploration of nanoplasmonic sensors in order to enhance measurement capabilities. While SPR is an excellent technique, there are some drawbacks. First, SPR excitation requires light coupling mechanisms that often entail specialized laboratory instrumentation and it is difficult to apply SPR measurement configurations to miniaturized, portable formats. Second, the high sensitivity to bulk refractive index changes makes SPR measurements susceptible to minor environmental variations (*e.g.*, temperature fluctuation) and therefore they must be operated in well-controlled environments. Third, while SPR is a surface-sensitive technique, the decay length of its electromagnetic field—a commonly used indicator of the field's penetration depth—is typically around 100–400 nm, which is much longer than the length scale of most biological macromolecules and hence SPR is only faintly sensitive to the orientation and conformation of adsorbed macromolecules and nanoscale biological particulates. In some cases, as the decay length of the evanescent field depends on the illumination wavelength, SPR measurements can also be conducted simultaneously at two wavelengths in order to characterize the size of adsorbed particles based on the relative measurement responses and appropriate formalisms.^{87,88} In general, SPR is more widely used to study the binding kinetics of biological macromolecules,⁸⁹ especially proteins⁹⁰ and nucleic acids.⁹¹ As an alternative option, nanoplasmonic sensors take advantage of the fact that, when the dimensions of metallic nanostructures become smaller than the wavelength of incident light, additional types of plasmon oscillations other than propagating SPs can be observed, which are locally confined by the nanostructure (nanoparticles or nanoholes) and collectively termed localized surface plasmon resonance (LSPR).⁵⁸ In comparison to SPR, LSPR is more highly surface sensitive, with the decay length of the electromagnetic field typically around 10–30 nm.⁹² At the same time, the sensitivity to bulk refractive index changes is lower so the measurements are more stable and less susceptible to environmental fluctuations.⁹³ In addition to LSPR, extraordinary optical transmission (EOT) is another related optical phenomenon that can arise from the interaction of light with periodic arrays of nanoholes and it involves a combination of propagating and localized SPs, sometimes called nanohole SPR. Nanoholes with short-range order correlations exhibit similar optical properties. One additional benefit of using nanohole arrays is the potential for trapping biological macromolecules and particulates (*e.g.*, viruses) within the holes as well as additional functionalities such as flow-through sensing. Importantly, nanoplasmonic sensors based on the LSPR and EOT phenomena do not require complex instrumentation and excitation of the nanostructures can be achieved using conventional laboratory spectrophotometers. As such, there is growing interest in the development of nanoplasmonic sensors on account of their relatively simple instrumental requirements, measurement stability, and high surface sensitivity. While the focus of most applications thus far has been analyte detection, one particularly compelling direction that is beginning to emerge for nanoplasmonic sensors lies in the biointerfacial sciences. This direction is significant because, while there is widespread debate about the sensing performance of SPR *versus* nanoplasmonic sensors, the capabilities of nanoplasmonic sensors for studying the biointerfacial sciences are unique and growing.

2. Nanoplasmonic sensing strategies

This section introduces the two main sensing strategies that are commonly utilized for nanoplasmonic sensor measurements at solid–liquid interfaces. The differences between these two sensing strategies are based on the type of nanostructures employed and the corresponding optical phenomena that underlie each strategy. We define these two sensing strategies based on the different optical phenomena, namely localized surface plasmon resonance (LSPR) and extraordinary optical transmission (EOT), which correspond to each strategy. LSPR arises from the interaction of light with deposited nanoparticles in random, non-interacting arrangements. On the other hand, EOT arises from the interaction of light with nanohole voids possessing long-range periodic or short-range ordering. For the purpose of this review, we focus on these general LSPR and EOT sensing strategies because they are the main ones discussed in the biointerfacial science literature and are the most relevant to broadly exploit the highly surface-sensitive measurement capabilities of nanoplasmonic sensors exhibiting localized plasmon modes. A schematic illustration of the two sensing strategies, including representative nanostructure architectures and spectral signatures, is presented in Fig. 1. Both nanoplasmonic sensing strategies are typically based on a single-spot optical extinction measurement across a large number of nanostructures on the sensor surface, and hence the resulting measurement responses are ensemble-averaged such that biointerfacial phenomena occurring on each nanostructure provide an individual contribution to the overall net response. However, the underlying optical phenomena of the two approaches have some differences and analytical methods to interpret experimental data vary accordingly, as discussed below in the following sections.

Understanding the different principles and capabilities of the two sensing strategies is important in order to contextualize the current state of research in the field as well as to appreciate

the potential of nanoplasmonic sensors to become a prominent surface-sensitive measurement approach for the biointerfacial sciences in general. With respect to measurement applications, the historical trend in the nanoplasmonic sensor field has been to optimize sensor performance for analyte detection. Table 1 presents a list of measurement characteristics that are widely considered for analyte detection and this list is mainly adapted from the SPR biosensing field. While SPR sensors typically have higher bulk refractive index sensitivities than nanoplasmonic sensors, the decay length of the SPR electromagnetic field is also longer as discussed above. Consequently, the shorter decay length of the electromagnetic field for nanoplasmonic sensors in general confers higher surface sensitivity (local refractive index changes).^{78,94–96} As a result, when an analyte is bound at the nanoplasmonic sensor surface, a larger proportion of the evanescent field is occupied by the analyte relative to the equivalent case for an SPR biosensor.^{92,97,98} General requirements of biosensing apply to the nanoplasmonic sensor case too, including proper consideration of measurement selectivity, response time, linearity, dynamic range, signal stability, and reliability. While impressive efforts have been made to increase detection limits, the general consensus from benchmark comparisons is that SPR and nanoplasmonic sensors have, at best, similar performance levels for analyte detection, although nanoplasmonic sensors do have simpler instrumentation requirements and reduced susceptibility to environmental perturbations (*e.g.*, temperature fluctuations) that make them particularly attractive for sensing applications. At the same time, there is growing attention to the wealth of information that nanoplasmonic sensors can obtain about processes relevant to the biointerfacial sciences, spanning across topics such as surface adhesion, macromolecular interactions, and conformational changes. Building on the measurement capabilities developed for detection applications, there is growing interest in understanding how measurement responses obtained by nanoplasmonic sensing experiments can be analyzed in order

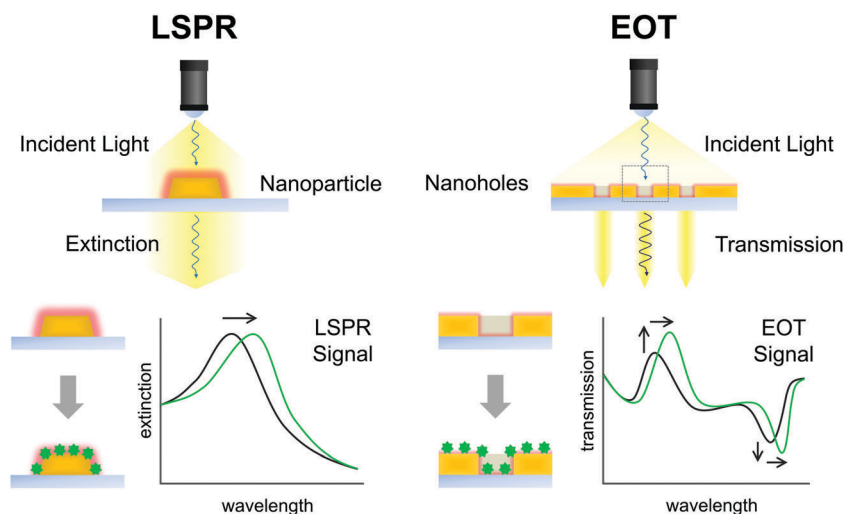


Fig. 1 Schematic illustration of the measurement principles, nanostructure architectures, and spectral information obtained from nanoplasmonic sensors based on the localized surface plasmon resonance (LSPR) and extraordinary optical transmission (EOT) phenomena.

Table 1 Overview of nanoplasmonic sensor concepts relevant to the biointerfacial sciences. Conventionally, nanoplasmonic sensors have been utilized for detection applications, and traditional biosensor characteristics, broadly defined as measurement capabilities, are important considerations for optimizing sensor performance. As nanoplasmonic sensors become increasingly utilized in the biointerfacial sciences, these characteristics remain important while additional scrutiny is placed on outputs which can be obtained from measurement analysis, defined as analytical capabilities. More detailed technical descriptions of biosensor characteristics can be found in ref. 99 and 100

Measurement capabilities	Sensitivity	Primarily refers to local refractive index sensitivity, which influences the probing volume and sensitivity to macromolecular adsorption.
	Selectivity	Detect target analyte in a selective manner while avoiding false signals from similar analytes or other interfering molecules.
	Response time	Time required for the sensor to yield an appreciable response indicating analyte detection.
	Linearity	The dynamic range of analyte concentrations over which the measurement signal is responsive and linearly proportional to concentration.
	Stability	Extent of variation in baseline signal and measurement response, both during a single measurement and during repeated uses (reproducibility).
Analytical capabilities	Adsorbate properties	Measurement responses are sensitive to the mass, thickness, conformation, and shape (deformation) of adsorbed molecules.
	Binding avidity	Measure the binding strength of one (affinity) or multiple (avidity) specific interactions between analyte and an immobilized molecule(s).
	Interaction kinetics	Track changes in adsorbate properties as a function of time during an interaction, either adsorbate–substrate, adsorbate–adsorbate, or a combination thereof.
	Environmental parameters	Understand how adsorbate-induced measurement responses depend on environmental parameters such as solution pH and ionic strength.

to obtain new insights into biointerfacial phenomena underpinning the interactions of these macromolecules with surfaces, the interactions between macromolecules, and the influence of environmental parameters (*e.g.*, solution pH, ionic strength) on the structure and function of adsorbed macromolecules. In this regard, the high surface sensitivity of nanoplasmonic sensors deserves particular attention because the decay length of the electromagnetic field pairs well with the size of biologically important macromolecules and particulates, including proteins, vesicles, exosomes, and viruses. Towards these goals, the practical utility of nanoplasmonic sensors for studying the biointerfacial sciences depends less on absolute sensitivity and more on the nanostructure geometry of sensor arrays and the short decay length of the corresponding electromagnetic field. Together with surface coating strategies, these features are opening the door to control the spatial localization of adhering macromolecules on sensor surfaces as well as enabling quantitative probing of structural and functional properties. Within this context, details of the operating principles of the LSPR and EOT sensing strategies are discussed along with a description of important sensing characteristics as well as an introduction to different surface functionalization options in the remaining parts of this section.

2.1. Localized surface plasmon resonance

In this section, we describe the general principles behind LSPR-based sensing strategies, including the optical properties giving rise to LSPRs, choices to design sensing platforms, measurement operation and data collection, and approaches to interpret experimental data. Where possible, we discuss these aspects in the context of the biointerfacial sciences, especially as they pertain to unique merits stemming from the high surface sensitivity.

2.1.1. Optical properties. LSPR generation occurs due to the interaction between incident light and discrete metallic nanostructures, whereby photons induce the collective

oscillation of free electrons in the conduction band of the metal. As a result, the electromagnetic field near the nanostructure's surface is greatly amplified and the maximum intensity of optical extinction (absorption plus elastic light scattering) occurs at the plasmon resonance frequency, which is in the visible wavelength range for noble metals (*e.g.*, gold and silver).¹⁰¹ According to Mie theory,¹⁰² in cases where nanoparticles are appreciably smaller than the wavelength of incident light (quasistatic approximation), scattering is negligible with respect to absorption and the extinction cross-section (σ) of an individual metal nanoparticle is described by^{103,104}

$$\sigma(\lambda) = \frac{18\pi V \epsilon_{\text{out}}^{3/2}}{\lambda} \left[\frac{\epsilon_i(\lambda)}{(\epsilon_r(\lambda) + \chi \epsilon_{\text{out}})^2 + \epsilon_i(\lambda)^2} \right] \quad (1)$$

where V is the nanoparticle volume, λ is the wavelength of light, ϵ_r and ϵ_i are the real and imaginary components of the metal dielectric function, respectively, ϵ_{out} is the dielectric constant of the external (medium) environment, and χ depends on the nanoparticle geometry (equal to 2 for a sphere and up to 20 for high-aspect ratio particles¹⁰⁵). The intensity (I) of light at a certain wavelength that passes through the sample is represented by¹⁰⁴

$$I = I_0 \exp(-N\sigma) \quad (2)$$

where I_0 is the intensity of incident light at the same wavelength and N is the number density of nanoparticles per unit area. The latter definition is applicable to nanoparticle clusters on a substrate as considered in this review, and can alternatively be expressed as the number concentration of nanoparticles for solution measurements.¹⁰⁴ In addition, the extinction of light (E) is related to the transmitted intensity as follows:^{104,106}

$$E = \log_{10}(I/I_0) \quad (3)$$

By combining eqn (1)–(3), it follows that, for clusters of spherical nanoparticles on a substrate, the extinction spectrum, expressed as $E(\lambda)$, is calculated by^{101,107}

$$E(\lambda) = \frac{24\pi^2 N a^3 \varepsilon_{\text{out}}^{3/2}}{\lambda \ln(10)} \left[\frac{\varepsilon_i(\lambda)}{(\varepsilon_r(\lambda) + 2\varepsilon_{\text{out}})^2 + \varepsilon_i(\lambda)^2} \right] \quad (4)$$

where a is the spherical radius. Of note, the metal dielectric function depends on the light wavelength. Compared to the incident field, the electromagnetic field of the metal nanoparticle is amplified when the dielectric constant of the metal is approximately equal to $-2\varepsilon_{\text{out}}$, and this condition is satisfied in the visible wavelength range for noble metals. The wavelength at maximum extinction is typically denoted as λ_{max} . Also, with increasing nanoparticle size, the relative contribution of scattering to the extinction increases.¹⁰⁸

As localized SPs are confined to the metallic nanostructure, the amplified electromagnetic field distribution is highly localized near the metallic surface and the decay length of the electromagnetic field is very short, on the order of 10–30 nm.⁹² If a process occurs near the sensor surface that affects the polarizability of the sensing material, the LSPR frequency changes slightly, in turn shifting features in its optical extinction spectrum. Typically, organic molecules have a greater refractive index than the surrounding aqueous medium so their presence near the sensor surface perturbs the local dielectric environment.¹⁰⁹ This high surface sensitivity provides the basis for characterizing biomacromolecular interactions, not only involving adsorption events but also conformational changes and structural transformations that influence the spatial proximity of an adsorbate to the sensor surface.

2.1.2. Platform design. The general design of a LSPR sensing platform entails choice of the (i) plasmonic material, (ii) geometrical properties of the nanostructures (typically nanoparticles), (iii) fabrication method, and (iv) surface coating. A wide variety of metals and metal-like materials support localized SP generation at visible wavelengths, although most commonly employed systems involve gold and silver. Gold is the most common material because it is chemically inert and stable, while silver is generally believed to have superior plasmonic properties but is prone to oxidation in ambient conditions.¹¹⁰ Among other options, aluminum has been widely studied in recent works due to its abundance, low cost, stability, processing ease, and tunable plasmonic properties.^{111,112} The shape and size of the nanoparticles are additional key parameters influencing the plasmonic properties. In general, nanoparticles that have higher aspect-ratio features such as nanorods have greater sensitivity to bulk refractive index changes but lower surface sensitivity on account of longer field decay lengths.¹¹³ In some cases, analyte binding is directed to “hot spots” with highly amplified electromagnetic fields between pairs of nanoparticles.¹¹⁴ When nanoparticles are deposited on a solid support, often a silica-based material, optical properties such as the electromagnetic field distribution and field intensity are strongly influenced by interactions between the nanoparticles and substrate, in turn influencing LSPR measurement sensitivity.¹¹⁵ For nanoparticles exhibiting particularly high refractive index sensitivities

in solution, there can be a significant loss in sensitivity when attached to a solid support and hence strategies to fabricate and immobilize nanoplasmonic transducers on solid supports are important considerations for nanoplasmonic devices.¹¹⁶ This is particularly true for nanocubes and nanoplates that have large areas of contact with the substrate, whereas spherical nanoparticles are less affected.¹¹⁶ In general, it is preferable to use low refractive index substrates and minimize the thickness of adhesion layers in order to preserve high measurement sensitivity of immobilized nanostructures.¹¹⁷

To fabricate LSPR sensing platforms, a wide variety of options exist based on either wet chemical synthesis of nanoparticles in solution followed by their deposition onto the substrate, or fabricating the nanoparticles directly on the substrate. In general, it is preferable to prepare randomly arranged, noninteracting nanoparticle arrays where high surface sensitivity is in demand. For disordered arrays of this kind, scattered fields influence the scattering and absorption properties of nanoparticles at the single-particle level in comparison to isolated nanoparticles, however, the scattering and absorption properties of the nanoparticles at the array level retain single-particle-like spectra.¹¹⁸ While not further discussed in this review article, it is also possible to fabricate periodic arrays of nanoparticles in which diffractive (far-field) coupling of the LSPR of individual nanostructures increases bulk sensitivity but decreases surface sensitivity.¹¹⁹ Towards fabricating random, noninteracting arrays of surface-bound nanoparticles, one of the most straightforward methods to prepare substrate-based LSPR sensors is through the deposition of nanostructures that have been prepared separately through wet chemical synthesis.^{120,121} Nanostructures with well-defined shape, size and uniformity can be assembled on a substrate with controllable surface coverage through simple immersion or spin-coating of the substrate in a solution containing the nanostructures.¹²² To facilitate nanoparticle adhesion, the substrate is sometimes pre-coated with a self-assembled monolayer bearing charged or polar functional groups (*e.g.*, amine or mercapto groups),^{123,124} a metallic adhesion layer (*e.g.*, chromium, titanium),¹²⁵ or surfactants.¹²⁶

While promoting adhesion is relatively simple, it is often-times difficult to control the orientation of adsorbed nanostructures, in turn causing detriment to measurement responses and interpretation of experimental data. Drop-casting techniques can sometimes be used to orientate anisotropic nanostructures, while it is possible to use the Langmuir–Blodgett technique to obtain a high-density coverage of nanostructures.¹²⁷ To obtain well-defined arrays, nanostructures can be fabricated on the substrate using nanosphere lithography (NSL).¹²⁸ NSL is a process in which a colloidal monolayer of spherical nanoparticles provides a mask for the vapor deposition of metal. Although this process is typically used to generate triangular prism nanoparticles, through either thermal annealing or variation in the angle of the masking nanosphere layer, a variety of nanoparticle shapes can also be formed. In some cases, hole-mask colloidal lithography is also employed to produce non-uniform surfaces with nanostructures on top,¹²⁹ or embedded nanostructures with some modifications to the fabrication protocol.¹³⁰ This fabrication technique is

reminiscent of NSL, but with the addition of a sacrificial layer and the masking is instead done by a thin film perforated with nanoholes that define an etching or evaporation pattern. The film is removed with the sacrificial layer after the etch/evaporation step, leading to the formation of a deposited nanodisk array on the target substrate. All of these techniques allow fabrication of a wide variety of LSPR sensors with complex and varied design features, from different nanoparticle shapes to varying surface coverages and arrangements of nanoparticles. Furthermore, simple immersion-based deposition techniques can easily be modified or scaled up to allow high-throughput production of sensor substrates.¹³¹ In addition, suspended nanodisks with improved measurement sensitivity were demonstrated by Sepulveda and co-workers by performing an isotropic chemical etch of the supporting substrate.¹³²

One remaining element of the platform design concerns the option to add a surface coating on top of the nanoplasmonic sensor. In traditional formats, the metallic sensing element is exposed to the bulk solvent, a format called “direct” nanoplasmonic sensing. One advantage of this approach is that the solid-liquid interface is in the region of highest electromagnetic field intensity and hence it is the most sensitive measurement approach. On the other hand, it is possible to add a thin dielectric layer on top of nanoparticles in order to stabilize the nanoparticles¹³⁵ and thereby utilize nanoplasmonic sensing with other material interfaces.⁷¹ The latter approach also carries the added advantage of improved sensor stability and hence measurement reproducibility. In this “indirect” nanoplasmonic sensing case, the resonance conditions for the LSPR will change slightly (*e.g.*, typically a redshift in the resonance maximum, λ_{\max}) while a portion of the electromagnetic field penetrates through the dielectric layer, which becomes the active sensor surface, albeit with some degree of reduced surface sensitivity due to the lower field intensity at the contacting surface.¹³⁴ Examples of direct and indirect nanoplasmonic sensing platforms are presented in Fig. 2. Conventionally, oxide-based coatings have been utilized although other possibilities are available, including diamond¹³⁶ and amorphous silicon-carbon alloy thin films¹³⁷ as well as embedding nanoparticles in a dielectric matrix.^{138–141} In addition, topographically flat LSPR sensors have been reported based on embedding gold nanodisks in an optical epoxy followed by coating with a silica overlayer.¹³³ On the other hand, surface functionalization strategies involving non-fouling polymers, for example, can be introduced in order to guide analyte binding to certain regions of the substrate while passivating other regions.¹⁴²

It should also be noted that individual, isolated nanohole voids also exhibit LSPR properties and behave similarly to discrete nanoparticles of equivalent dimensions.^{143,144} However, nanohole arrays typically exhibit EOT-like optical properties. The details of nanohole fabrication will be explained in Section 2.2.2, in relation to short-range and long-range ordered arrays of nanoholes.

2.1.3. Measurement operation. Conventional experimental strategies in ensemble-averaged configurations involve measurement of the optical extinction spectrum. The most typical approach

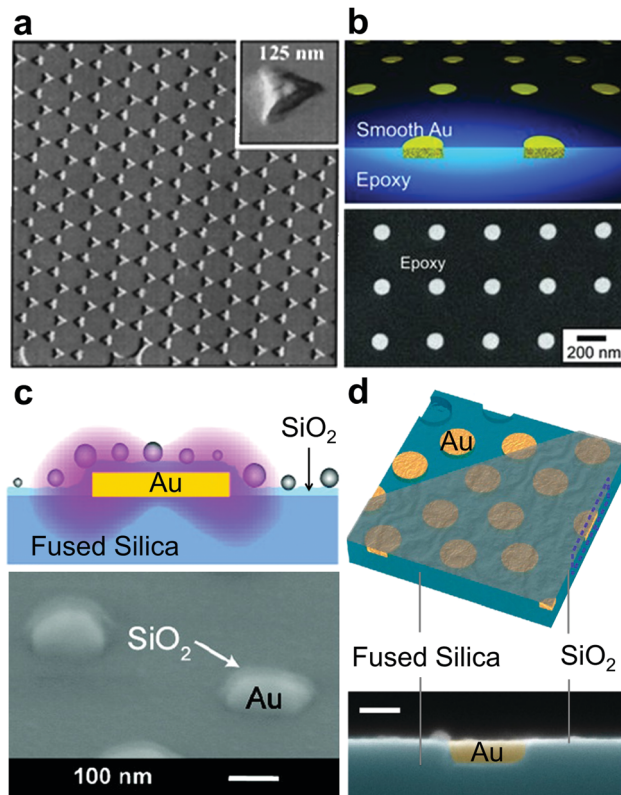


Fig. 2 (a and b) Examples of direct nanoplasmonic sensing platforms. (a) Atomic force microscopy (AFM) image of single layer periodic particle arrays of Ag nanotriangles obtained via nanosphere lithography. Reprinted (adapted) with permission from ref. 128. Copyright 2001 American Chemical Society. (b) Schematic illustration of embedded gold nanodisks in epoxy (top) and a top view SEM micrograph of 27 nm thick gold nanodisks in epoxy on a glass substrate. Reprinted (adapted) with permission from ref. 133. Copyright 2013 Wiley-VCH. (c and d) Examples of indirect nanoplasmonic sensing platforms. (c) Schematic depiction of the nanoarchitecture of an indirect nanoplasmonic sensing platform (top) and a tilted-view SEM micrograph of a sensor chip decorated with Au nanodisks coated with a silica layer (bottom). Reprinted (adapted) with permission from ref. 134. Copyright 2010 American Chemical Society. (d) A 3D schematic illustration of a topographically flat nanoplasmonic sensor with an embedded array of plasmonic Au nanodisks along with a cross-sectional SEM micrograph of the platform. The scale bar represents 50 nm. Reprinted (adapted) with permission from ref. 130. Copyright 2016 American Chemical Society.

involves transmission ultraviolet-visible spectroscopic measurements, obtained by using a standard UV-vis spectrophotometer, in which light passes through the sample, which is on a transparent substrate (*e.g.*, glass), and the extinction spectrum is acquired based on the transmitted light. In addition to planar substrates, it is also possible to conduct transmission measurements by using more compact and portable optical fiber platforms, in which case the fiber tip is functionalized with nanoparticles.^{145–147} Alternatively, it is possible to conduct LSPR measurements on non-transparent substrates by using a reflective geometry, in some cases with improved sensitivity.¹⁴⁸ In such cases, an optical fiber bundle is used to excite the nanostructures with incident light as well as collect light reflected from the sensor surface.¹⁴⁹ The spectral information obtained by measurements in transmission

versus reflection modes can have some variation because both absorption and scattering contribute to extinction in transmission measurements, whereas, in reflection measurements, absorption is not detected and only back scattering contributes to the measured extinction.⁹⁸ In reflection mode, there can also be an additional contribution to the measurement response from the reflectance of the substrate such that the reflectance spectrum exhibits a characteristic wavelength that is close, but not identical, to the LSPR wavelength.¹⁵⁰ As a result, in transmission measurements, the LSPR wavelength is observed as the maximum intensity in the extinction spectrum; the relative contribution of absorption and scattering depends on the nanoparticle size as discussed above. On the other hand, in reflection measurements, the LSPR signal is commonly observed as the minimum intensity in the reflectance spectrum.^{63,101} Such measurements are often realized by UV-vis diffuse reflectance spectroscopy, for example.¹⁵¹ In some cases involving optical fiber systems operated in reflection mode, relatively large nanoparticles have been utilized whereby scattering contributes significantly to extinction and the maximum intensity in the extinction spectra is monitored.^{149,152,153}

In general, one benefit of acquiring the entire spectrum is that detailed analysis of various spectral features can be done simultaneously with data acquisition or later after the experiment. Dahlin *et al.* developed a widely used curve fitting procedure to improve the spectral resolution to 0.01 nm by reducing the signal-to-noise ratio of the measurement readout and calculating the centroid position (interpreted as the LSPR wavelength and intensity) in the extinction spectra¹⁵⁴ (also known as high-resolution LSPR¹⁵⁵). The most common parameter to analyze is the position of the LSPR wavelength (λ_{max}) or its corresponding intensity.¹⁵⁶ Changes in the full-width-at-half-maximum (ΔFWHM) are also possible to obtain from the measurement data,¹⁵⁷ and all three of these parameters are sensitive to the bulk and local refractive indices. Among them, it has been suggested that the change in relative intensity per change in refractive index unit is perhaps the most appropriate metric for evaluating sensitivity^{158,159} as the change in light intensity is the actual parameter that is measured by the photodetector.^{97,160} On the other hand, an ΔFWHM shift is sometimes observed coincident with an $\Delta\lambda_{\text{max}}$ shift for adsorption events, whereas in other cases, $\Delta\lambda_{\text{max}}$ shifts can occur without a corresponding ΔFWHM shift.¹⁵⁷ Recently, Chen *et al.* also reported that the inflection point at the long wavelength side of the LSPR peak has higher bulk and local refractive index sensitivities than $\Delta\lambda_{\text{max}}$ shifts.¹⁶¹

Of note, while there is typically one intensity peak in the extinction spectra of spherical metal nanoparticles, this is not a general rule for all shapes of nanoparticles and the extinction spectra for other types of nanoparticles, such as prolate and oblate spheroidal nanoparticles, may have more than one intensity peak and due attention is warranted for picking the appropriate spectral signature for data analysis.¹⁶² For example, the plasmon resonance of gold nanorods is split into two modes, namely the transverse and longitudinal modes along the short and long axes of the nanorod, respectively.¹⁶³ In most biosensing cases, the longitudinal mode is used when studying nanorods as it is considered to be the more sensitive mode.¹⁶⁴

While spectroscopic measurements provide a wealth of information for detailed analysis, they are typically low-throughput and there is growing interest to develop high-throughput LSPR measurement capabilities. One promising approach involves LSPR imaging, whereby the scattering intensity can be obtained with high temporal and spatial resolution by a charge-coupled device (CCD) camera detector.¹⁶⁵ In this imaging format, the pixel count is a sum over all the LSPR peak wavelengths (weighted by the quantum efficiency of the detector at each wavelength), but the resulting data lacks spectral details in the conventional format. To address this gap, a liquid crystal tunable filter has been used to perform single-wavelength optical measurements, which were recorded over a series of wavelengths in order to establish intensity maps from which extinction spectra were constructed in a multiplexed format.¹⁶⁶ On the other hand, detection can also be done with angle-resolved spectroscopy,¹⁶⁷ but this technique is less popular. Reflection-based refractive index sensing measurements based on measuring both the intensity and phase of the reflected beam is also possible and can increase the bulk refractive index sensitivity and corresponding figure of merit (see Section 2.3 for formal definitions).^{168,169} While not further discussed in this article except where noted in specific instances of particularly intriguing sensor design, it is noted that other variations of LSPR-based nanoplasmonic sensing strategies are also possible, including measurements characterizing the scattered light of individual nanoparticles *via* dark-field illumination.^{80,170,171} One particularly promising example of dark-field illumination involves hyperspectral imaging whereby a high-resolution spectrum is acquired for each pixel in an image, thereby enabling simultaneous spatial and spectroscopic characterization of the sample.^{172–175}

2.1.4. Data interpretation. Conventionally, LSPR measurement data analysis is based on tracking the wavelength or intensity shift as a function of time or after a set period of incubation time. The wavelength shift is typically recorded at the extinction maximum although it is also possible to measure the intensity at a fixed wavelength depending on the particular system and measurement configuration. In general, an increase in the position of the extinction maximum is associated with the adsorption of biomacromolecules and the corresponding LSPR-tracked kinetics are monitored. As LSPR is highly sensitive to the local refractive index change, a larger measurement response is understood to be proportional to a greater number of bound molecules. As such, the kinetic data can provide quantitative estimates of the association and disassociation rate constants for binding interactions. Taking into consideration that the adsorption rate of biomacromolecules is typically limited by the rate of bulk diffusion, it is also possible to extract the surface coverage at saturation from the wavelength shift data by accounting for the time scale of adsorption and defining the flow conditions in the measurement chamber. While other surface-sensitive techniques can also provide information about the adsorption kinetics, LSPR has unique merits due to its particularly high surface sensitivity and the fact that the decay length of its electromagnetic field is within the size range of biological macromolecules.

From the perspective of characterizing adsorbed biomacromolecules, there is also interest in extracting quantitative information about the mass and shape properties of adsorbates. Guiding influences for data interpretation originate from the SPR biosensing field.⁴⁶ Jung *et al.* first presented a quantitative mathematical formalism for interpreting SPR measurement responses arising from a uniform layer of an adsorbed film,¹⁷⁶ as described by

$$\Delta R = m \times (n_a - n_m) \times [1 - \exp(-2t/l_d)] \quad (5)$$

where ΔR is the measured sensor response (which can be defined as either the shift in wavelength or angle of the SPR minimum in reflected light intensity¹⁷⁶), n_a and n_m are the refractive index values of the adsorbate and the surrounding medium, respectively, t is the thickness of the adsorbate, l_d is the decay length of the evanescent electromagnetic field, and m is the sensitivity factor which is equal to the bulk refractive index sensitivity of the chosen measurement response as t approaches infinity. By applying this formalism, it is possible to estimate the thickness of adsorbed films in addition to surface coverages and concentrations of known biomacromolecules in SPR experiments. A similar approach has also been outlined for analyzing LSPR spectral shifts,^{63,101} and it has been quite successful as an approximation, as described by

$$\Delta\lambda_{\max} = m \times (n_a - n_m) \times [1 - \exp(-2t/l_d)] \quad (6)$$

in the case of tracking a shift in the resonance maximum. At the same time, there is growing interest to refine the model as it is recognized that the original formalism was intended to describe propagating SPs, whereas localized SPs of nanostructures have more complex electromagnetic field distributions.^{177,178} Indeed, the decay of the electromagnetic field around metal nanoparticles is of the power-law type, rather than exponential, and its dependence on coordinates can be complex. For relatively simple geometries such as nanodisks,^{179,180} the nanodisk can be approximated by an ellipsoid and its electromagnetic field is fairly well-described in analogy with spherical nanoparticles.^{181,182} By applying these mathematical treatments, it has been possible to develop sophisticated approaches for estimating the contribution of adsorbate molecules to $\Delta\lambda_{\max}$ shifts. To date, the most extensive efforts of this kind have focused on characterizing the adsorption of phospholipid vesicles onto solid supports as discussed below, and estimate the dependence of the measurement responses on total lipid concentration and vesicle size although the approach is generalizable to other classes of biological macromolecules as well. In addition to $\Delta\lambda_{\max}$ shifts, the ΔFWHM shift is also sensitive to macromolecular adsorption and its broadening is influenced by the average number of adsorbate molecules contacting a nanoparticle surface.¹⁸³

Perhaps the most unique feature that can be obtained from LSPR measurements relates to probing the shape of adsorbed macromolecules. As described below, pioneering studies identified that the LSPR electromagnetic field is sensitive to the conformation of phospholipid molecules, for example. Specifically, an increase in the sensor response arises from the spatial proximity of lipids near the sensor surface, including the possibility to

distinguish between lipids in adsorbed vesicles and a supported lipid bilayer. By applying biointerfacial science concepts to interpret LSPR measurement data, it has been possible to further develop models for interpreting the relative deformation/conformation of adsorbed biomacromolecules. In particular, a wealth of information can be obtained from analyzing the initial stages of macromolecular adsorption. Since the rate of adsorption is typically limited by the rate of bulk diffusion, there is a linear rate of change in the LSPR measurement signal at low surface coverages, which is proportional to the diffusion rate. This benchmark provides the basis for analyzing the extent of conformational changes in response to surface adsorption. These measurement capabilities are particularly useful when comparing macromolecular adsorption on different sensor surfaces, in which cases the relative strength of the adsorbate–substrate interaction varies. If the adsorbate binds more strongly to one substrate, it is possible that the adsorbate deforms more greatly and spreads across the surface (*e.g.*, inducing a conformational change) in order to maximize interactions with the surface. In such cases, the measurement response (the rate of change in the LSPR signal) would be greater for the more-deformed adsorbate because its molecular mass is, on average, closer to the sensor surface than in a case where the adsorbate–substrate interaction is weaker. The key advantage here is that LSPR is sensitive to the shape of adsorbed macromolecules in the requisite size range, unlike other common surface-sensitive techniques such as QCM-D and SPR for which the probing volumes are much larger. Such capabilities can also be extended to investigate how environmental parameters (*e.g.*, solution pH, ionic strength, temperature) influence adsorption processes and corresponding conformational changes in macromolecules. Indeed, temperature-dependent adsorption processes can be easily followed by LSPR measurements because of its relatively low sensitivity to bulk refractive index changes.

From a design perspective, optimizing the architecture of the sensor surface for sensing performance is also important for biointerfacial science applications because appropriate choice of the decay length of the electromagnetic field can improve detection of conformational changes in adsorbed biological macromolecules. Using eqn (6), the decay length can be estimated by coating the nanodisk surface with varying thicknesses of a dielectric layer (*e.g.*, *via* atomic layer deposition) and measuring the corresponding changes in the LSPR spectral properties, including the $\Delta\lambda_{\max}$ shift.⁹²

2.2. Extraordinary optical transmission

In this section, we describe the general principles behind EOT-based sensing strategies, including the optical properties giving rise to the EOT effect, choices to design sensing platforms, measurement operation and data collection, and approaches to interpret experimental data. Where possible, we discuss these aspects in the context of the biointerfacial sciences, especially as it pertains to unique merits stemming from the geometrical configuration of nanohole arrays and especially the simultaneous measurement of spectral features associated with propagating and localized plasmon modes.

2.2.1. Optical properties. EOT describes an optical phenomenon whereby light transmits through an array of nanoholes of dimensions smaller than the wavelength of incident light, in a metallic film at appreciably higher magnitudes than what classical aperture theory predicts.⁶¹ The enhanced transmission is caused by the interplay of localized modes associated with individual nanoholes together with grating-type coupling (Bloch wave) to propagating surface modes due to the periodicity along with cavity modes.^{184–186} As a result, the EOT spectral signatures exhibit wavelength-dependent transmission enhancement, resulting in multiple transmission maxima and minima.¹⁸⁷ In this regard, both localized and propagating SPs influence EOT spectral signatures, and particular transmission maxima and minima are attributed to different plasmon modes, which can be sensitive to different regions of the nanohole geometry as well as possess different surface sensitivities.¹⁸⁸

In general, the transmission spectra of nanohole arrays show at least two transmission maxima (denoted as λ_{SP}) and their spectral positions can be predicted based on the relationship to the lattice constant (periodicity) of the array (p), the scattering orders of the nanohole array (i and j), and the real parts of the dielectric constant of the surrounding medium and the metal (ϵ_{out} and $\epsilon_r(\lambda)$, respectively), as described by the following equation⁶¹

$$\lambda_{SP}(i, j) = \frac{p}{\sqrt{i^2 + j^2}} \sqrt{\frac{\epsilon_r(\lambda)\epsilon_{out}}{\epsilon_r(\lambda) + \epsilon_{out}}} \quad (7)$$

Of note, the metal dielectric constant depends on the light wavelength (λ). In cases of very high ordering, there is an additional third transmission peak that is attributed to a cavity resonant mode.^{189,190} Indeed, while EOT is most commonly discussed for periodic arrays of nanoholes with long-range ordering, EOT also occurs in short-range ordered nanohole arrays.^{191,192} As disorder in the periodic structure increases, the intensities of the transmission peaks decrease and the FWHM of each transmission peak increases.^{193,194} With increasing disorder approaching randomness, the EOT effect becomes attenuated although short-range correlations still give rise to hole-hole interactions that result in different optical properties between single nanoholes and random arrays of nanoholes. As such, EOT effects lead to complex spectral features that provide many sensing opportunities in various contexts relevant to the biointerfacial sciences. Of particular interest, in response to local or bulk refractive index changes, different spectral features can be sensitive depending on the system, and hence appropriate consideration of the optical properties is warranted when optimizing sensor performance.

2.2.2. Platform design. As with LSPR-based sensors, the general design of an EOT sensing platform entails choice of the (i) plasmonic material, (ii) geometrical properties of the nanoholes, (iii) fabrication method, (iv) surface coating, and (v) flow conditions. However, the design and fabrication of nanohole arrays entails more options and complexities, hence necessitating a detailed discussion of these factors as they pertain to biointerfacial science measurements, including additional

consideration of flow configuration in nanoholes *versus* nanopores. Here, we define nanoholes as porous metallic thin films supported on one side by a continuous, non-porous dielectric film that is impervious to liquid flow. On the other hand, nanopores are defined as porous metallic films through which fluids can flow across two compartments. Examples of the different EOT-based sensing platforms are presented in Fig. 3. Typically, nanohole systems are comprised of a thin metal film on a dielectric substrate, with gold the most popular metal on account of its optical properties and chemical stability.¹⁹⁵ Dielectric supports with lower refractive index values are typically favored because they increase measurement sensitivity over conventional glass substrates.¹⁹⁶ Other options include silver¹⁹⁷ and aluminum; when silver is used, it is generally coated with a thin layer of a dielectric material in order to prevent its tarnishing.^{198,199} More complex structures are also possible, including a metal–dielectric double film,²⁰⁰ multiple layers of

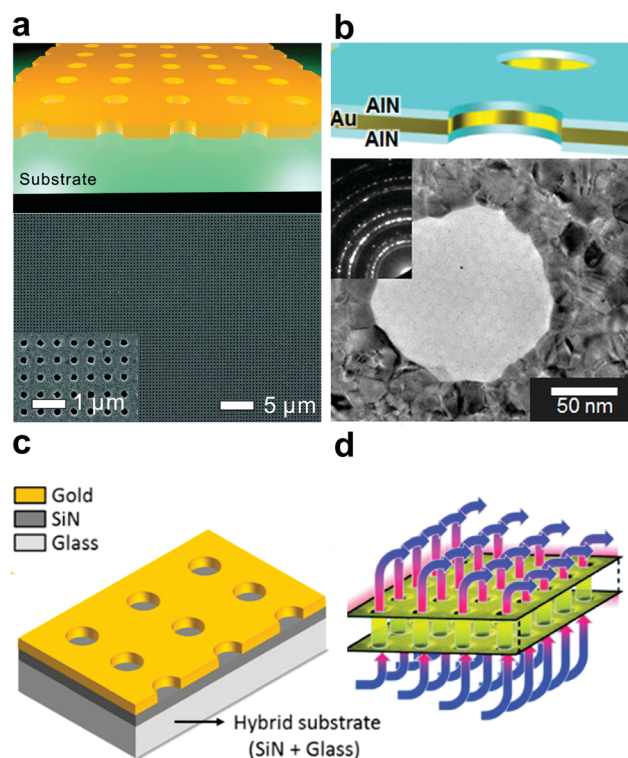


Fig. 3 (a) Schematic illustration of large-area smooth Ag nanohole arrays fabricated *via* template-stripping (top) along with an SEM micrograph of the template-stripped Ag periodic nanohole array (bottom). The inset shows a zoomed-in micrograph of the template stripped Ag nanoholes. Reprinted (adapted) with permission from ref. 206. Copyright 2011 American Chemical Society. (b) Schematic illustration of AIN/Au/AIN trilayer pores (top) along with TEM micrograph of the trilayer pores and corresponding diffraction pattern in the inset (bottom). Reprinted (adapted) with permission from ref. 205. Copyright 2014 American Chemical Society. (c) Schematic illustration of gold nanohole arrays on hybrid substrate of silicon nitride and glass. Reprinted (adapted) with permission from ref. 203. Copyright 2015 American Chemical Society. (d) Schematic illustration showing the direction of fluid flow through nanopores in a gold-on-silicon nitride membrane. Arrows depict flow direction. Reprinted (adapted) with permission from ref. 207. Copyright 2009 American Chemical Society.

aluminum and aluminum nitride²⁰¹ as well as metal–insulator–metal systems,²⁰² and the optical properties of these systems are actively being explored. While nanoholes are conventionally formed on transparent material supports, it was demonstrated that inclusion of a high refractive index dielectric interlayer increased measurement sensitivity.²⁰³ For nanopores, the dielectric support is typically a silicon nitride membrane,²⁰⁴ while one report showed that a thin gold nanopore film could be fabricated without a dielectric support.²⁰⁵

Aside from the material composition, the geometrical dimensions of nanohole arrays are critical determinants of the optical properties. As mentioned above, the EOT effect is greatest for nanohole arrays with long-range periodic ordering and progressively lower as the degree of disorder increases. Typically, the metallic thin film is less than 100 nm thickness. Otherwise, in significantly thicker films, propagation of modes along the aperture is the dominant optical effect¹⁸⁶ and the films are optically opaque.¹⁸⁸ The optimal film thickness for well-defined optical properties is around 10–50 nm and is sufficiently thin to allow light to pass through the film.^{56,188,208} Typically, circular nanoholes are around 100 nm diameter in order to facilitate coupling to plasmon modes.⁷⁶ On the lower end, Xiong *et al.* recently reported the fabrication of short-range-ordered arrays with 50 nm diameter nanoholes, with greater sensitivity localized to the interior of the holes whereas the bulk refractive index sensitivity was unchanged as compared to larger nanoholes.²⁰⁹ On the other hand, plasmon excitation was not achieved in smaller holes below 50 nm diameter.²⁰⁹ The specific wavelengths at which different spectral features manifest themselves strongly depends on the geometrical arrangement of the nanoholes and various square, rectangular, and hexagonal lattices have been explored among other options.^{210–212} In a recent theoretical study,²¹² it was identified that the hexagonal lattice contributes to a larger figure of merit (FoM) value than the conventional square lattice due to a narrower spectral response as well as a higher surface sensitivity based on a model, thin dielectric film (for more information and formal definitions of FoM, see discussion in Section 2.3 below).

To produce nanohole arrays, several top-down fabrication strategies can be employed, including electron beam (e-beam) lithography and focused ion beam (FIB). An in-depth discussion of these fabrication strategies is described in ref. 195 and 213. E-beam lithography is capable of producing homogenous nanoholes but is low throughput, expensive, and is not suitable for patterning large areas. In early generations, FIB was a more popular option to prepare nanohole arrays based on milling, but is also low throughput.¹⁴⁴ More recently, improved methods based on nanoimprinting²¹⁴ and template-stripping²¹⁵ have also been developed in order to permit fabrication over a wider surface area in a more high-throughput fashion. Alternatively, bottom-up fabrication approaches based on colloidal self-assembly can be employed to produce short-range or long-range ordered nanohole arrays, and particular examples are described by Dahlin in ref. 76. In all cases, ultrasoft surfaces are preferred as surface roughness and other imperfections can limit sensor performance.^{216,217} Aside from chemical

stability, dielectric overlayers can further enhance sensing possibilities by applying nanoplasmonic transducing elements to study biointerfacial processes at other material interfaces; see, *e.g.*, ref. 206. Nanohole fabrication is also achievable on optical fibers for EOT-based sensing applications.^{218–220} In another interesting direction, Peer and Biswas recently demonstrated that a continuous, corrugated gold film on a periodically textured substrate can exhibit EOT effects arising from variations in the gold thickness even though there were no holes in the film.²²¹

While the general features of nanoholes and nanopores are quite similar, one distinct feature of nanopores is their flow-through geometry and compatibility with microfluidic systems.²²² Indeed, the method of bringing the analyte into contact with the sensing surface from the bulk solution is an important factor in determining the time resolution for detection applications. In most cases, the analyte is suspended within a liquid medium, which is located above the sensor substrate. However, relying solely on passive diffusion of the analyte to the sensing surface results in relatively poor temporal resolution with a strong dependence on the analyte concentration. One fairly simple solution in the case of nanopore-based sensors is to place the sensing surface in a suspended configuration between two layers of a liquid medium and invoke flow through the nanohole arrays, thereby actively delivering the analyte to the substrate.^{207,223} With an increased analyte flow perpendicular to the surface, the time scale of the measurement response with respect to changes in analyte concentration is significantly improved, especially in optofluidic configurations.²²⁴ Another innovation demonstrated by Barik *et al.* employs dielectrophoresis (DEP).²²⁵ In this case, a strong electromagnetic field gradient is produced near the sensing surface in order to attract and trap electromagnetically polarizable analytes at locations of the greatest local sensitivity, whereby the rims of each nanohole concentrate charge and simultaneously act as a DEP electrode and a sensor transducer. Taken together, EOT-based arrays possess a wide range of tunable properties in order to design systems that are optimized for various applications. Of note, the scale of the nanohole geometry is appropriate for incorporating biological particulates such as vesicles and virus particles into the measurement configurations.

2.2.3. Measurement operation. Conventional experimental strategies involve the measurement of an optical transmission spectrum by a conventional spectrophotometer.²²⁶ As light is incident on one side of the sensor and detected on the other, the spectral features are analyzed based on the transmitted light intensity as a function of wavelength. Shifts in the wavelengths of one or more of these spectral features occur due to changes in the local or bulk refractive indices, and can be monitored as a function of time along with intensity and FWHM changes.²²⁷ Of note, the angle of incidence can influence the dispersion of transmission processes related to SPPs, whereas processes related to localized SP and cavity modes are expected to be less affected. As a result, it is possible in some cases to increase the surface sensitivity (shorter decay length of the electromagnetic field) by using a larger angle of incidence.²²⁸ A 96-well plasmonic sensing platform based on periodic nanohole arrays was recently

reported, and the angle of incidence was optimized to increase measurement sensitivity for detecting refractometric shifts in a transmission minima.²²⁹ It is also possible to perform measurements in reflection-mode, which allows better integration with other measurement techniques.^{220,230–232} As an alternative option, Couture *et al.* showed that sensing experiments with periodic nanohole arrays can also be conducted in the Krestchmann configuration, which increased the decay length of the electromagnetic field from approximately 140 nm (in EOT operation) to 200–300 nm, with a nearly seven-fold increase in sensitivity to bulk refractive index changes.²³³ The reflection phase and amplitude for a short-range ordered gold nanohole array has also been measured using an interferometric substrate.²³⁴

Multiplexing capabilities have been actively explored for periodic nanohole arrays,⁷⁷ with one of the earliest reports describing measurements on over one million sensor spots based on imaging bandpass filter-amplified changes in spectral intensity after an incubation period.²³⁵ It has also been possible to develop parallel real-time measurement capabilities for intensity-based measurements, with reference channels serving as negative controls to account for fluctuations and a packing density of 10^6 sensing elements per square centimeter.²³⁶ In order to collect more detailed information, an advanced multiplexed format was developed in which simultaneous measurements were performed on 50 parallel microfluidic channels with full-spectral imaging capability.²³⁷ Seiler *et al.* recently reported the direct spectral imaging of plasmonic nanohole arrays by using a CMOS imager chip to measure the intensity distribution across a wide area without requiring a microscope or spectrophotometer.²³⁸ Based on a lens-free computational microscopy approach, Cetin *et al.* also developed a hand-held, plasmonic biosensor comprising periodic arrays of nanoholes,²³⁹ and another version that included dual-color on-chip imaging was capable of real-time monitoring of molecular binding events as well.²⁴⁰ As such, the operation of EOT-based nanoplasmonic sensors has largely been aimed at detection while the full exploration of spectral features in the context of the biointerfacial sciences is continuing to evolve.

2.2.4. Data interpretation. One benefit of EOT-based sensing strategies is the rich collection of spectral information that is recorded in the measured transmission spectra. Indeed, the EOT-related spectral features correspond to numerous localized and propagating modes that have varying surface sensitivities and are sensitive to different interfaces/regions of the nanohole geometry. From this perspective, periodic arrays of nanoholes with long-range ordering are desirable because more spectral features are discernible, including transmission minima as well as the appearance of additional peaks in some cases.²⁴¹ However, EOT-based nanoplasmonic sensing studies typically report only the spectral feature (either the wavelength position or intensity of a spectral feature) that yields the highest measurement sensitivity for detection of a binding event. This approach is justifiable for analyte detection applications but a deeper understanding of the spectral responses is warranted for the quantitative biointerfacial sciences. Indeed, as Dahlin points out,⁷⁶ some outstanding questions remain about the relationship between certain spectral features

and the corresponding plasmon modes as well as how the optical properties of short-range and long-range ordered nanoholes fully compare. In one interesting recent study, Ballard *et al.* used machine learning approaches to identify that the highest sensitivity spectral features did not necessarily correspond to wavelengths at which transmission maxima or minima occur.²⁴²

In terms of quantifying adsorbate-induced measurement responses, we recall the discussion in Section 2.1.4 regarding how an exponential decay model is insufficient to describe the electromagnetic field surrounding metal nanoparticles. A similar issue arises for nanoholes and it should also be stressed that the decay length of the electromagnetic field depends on the plasmon mode under consideration.¹⁸⁸ For localized plasmon modes, the decay length is on the order of 20–40 nm whereas the decay length approaches comparable values to conventional SPR measurements for propagating plasmon modes (hundreds of nm). Hence, analyte detection has conventionally used spectral features that arise from propagating plasmon modes because they are sensitive to larger probing volumes and therefore have greater sensitivity to bulk refractive index changes, hence the name “nanohole SPR”. On the other hand, there is significant potential for further investigating spectral features that are sensitive to localized plasmon modes as well as comparing measurement responses across different spectral features. As will be explained in the following sections, such information can provide insight into the location of bound adsorbate molecules on the sensor surface as well as provide real-time monitoring of biomacromolecular interactions occurring inside nanoholes. These findings are just the latest examples of the unique capabilities of nanoplasmonic sensors to probe topics within the biointerfacial sciences, and interpretation of the experimental data obtained remains full of possibilities.

2.3. Sensing characteristics

With the ongoing development of LSPR- and EOT-based nanoplasmonic sensors to study biointerfacial phenomena at solid-liquid interfaces, there is growing interest to establish a measurement framework to define sensing performance, especially to understand how probing volume influences bulk *versus* surface sensitivity. Historically, a defining feature of optical biosensors has been their performance to measure changes in the refractive index (RI) of a bulk solution and the corresponding bulk refractive index sensitivity, S_B , is defined as

$$S_B = \frac{\Delta R}{\Delta n} \quad (8)$$

where R is the measurement response and n is the refractive index of the medium. In nanoplasmonic sensors, the measurement response can be essentially any parameter that is obtained from the spectral signature, and is typically either the position of a wavelength maximum or minimum, or the intensity at a certain wavelength. Ideally, as expressed in eqn (8), there will be a linear relationship between ΔR and Δn within the tested range of RI values, *i.e.*, S_B is a constant value. As part of data analysis, different spectral features can be evaluated in order to identify the

parameter with the highest S_B and this feature is commonly analyzed for detection applications. Indeed, the SPR technique is widely known to support sensor configurations with high S_B values and hence very small changes in the refractive index of the bulk solution can be detected. Likewise, many nanoplasmonic sensors have been developed to have high S_B values as well. A popular method to quantify detection performance is the figure of merit (FoM), and its bulk sensitivity version, FoM_B, that is defined as

$$\text{FoM}_B = \frac{S_B}{w} \quad (9)$$

where w is the width of the spectral feature (conventionally the FWHM) under analysis. While S_B can be difficult to compare across different systems due to variations in wavelength and energy scales, FoM normalizes these factors to facilitate direct comparison of sensing performance.¹¹⁷ In general, it is appreciated in the literature that a larger FoM_B, which is reflective of a narrow FWHM, leads to higher spectral resolution.²⁴³ At the same time, as Dahlin *et al.* point out,⁵⁶ the implementation of curve-fitting algorithms and noise reduction strategies can allow measurement of very small measurement features from even relatively wide spectral features.¹⁵⁴ Furthermore, an important distinction is that sensor systems with large S_B values have large probing volumes, *i.e.*, the decay length of the evanescent electromagnetic field is comparatively long. For studying biointerfacial phenomena at solid–liquid interfaces, it has become increasingly apparent that a large S_B value can actually result in lower measurement sensitivity because, when adsorbed biomacromolecules are only at the solid–liquid interface, the vast majority of the evanescent electromagnetic field is not occupied by biomacromolecules in such cases. A pertinent example is found in ref. 244 where the sensitivity to changes in local refractive index due to protein adsorption was inversely related to the FoM_B value of the nanoplasmonic sensor system.

Hence, it is desirable to develop nanoplasmonic sensors with shorter decay lengths that have higher surface sensitivities. Indeed, while a shorter decay length would translate into a lower S_B value,^{245,246} the probing volume would be smaller and hence highly surface-sensitive nanoplasmonic sensors would maintain similar signal-to-noise ratios for detecting biomacromolecules at low analyte concentrations.^{92,94} Formally, the surface sensitivity, S_s , can be expressed as follows²⁴⁷

$$S_s \approx S_B \exp(-2d/l_d)[1 - \exp(-2t/l_d)] \quad (10)$$

where l_d is the decay length of the amplified electromagnetic field, t is the thickness of the layer over which the refractive index change occurs, and d is the distance of the layer from the sensor surface. Inspection of eqn (10) identifies that S_s is correlated with S_B and that l_d is an important factor. The geometrical properties of the biomacromolecules as well as its spatial proximity to the sensor surface in the bound state should also be considered for optimal performance. Recently, the Van Dorpe group introduced the concept of second-order surface sensitivity that is calculated as the second-order

derivative of the wavelength shift, $\Delta\lambda$, in eqn (6) and described as follows^{178,244}

$$\frac{\partial^2 \Delta\lambda}{\partial n_a \partial t} = \frac{2S_B}{l_d} [\exp(-2t/l_d)]. \quad (11)$$

The corresponding surface sensitivity version of FoM is labeled as FoM_S, and formally defined as¹⁷⁸

$$\text{FoM}_S = \frac{\frac{2S_B}{l_d} [\exp(-2t/l_d)]}{w} \quad (12)$$

The inverse dependence on l_d in eqn (11) underscores that, for a fixed S_B value, longer decay lengths result in lower surface sensitivity. As Li *et al.* described in their work,¹⁷⁸ the ideal design would encompass the largest possible value of $\frac{2S_B}{l_d}$ and a l_d value that matches the size of the target biomacromolecules (Fig. 4). For example, a relatively short l_d might be preferable for the detection of small biomacromolecules such as proteins, whereas a relatively longer l_d could be useful for detecting larger biological particulates such as viruses and exosomes or detecting biomacromolecules of various kind when the sensor surface is modified with a passivation coating (as discussed in Section 2.4 below). Even so, as will be explained below in the following sections, there are cases in the biointerfacial sciences where it is preferable to have an l_d value that is smaller than the size of biomacromolecules under investigation (*e.g.*, lipid vesicles) in order to study shape deformation of the adsorbed biomacromolecules, for example.

At present, as Špačková *et al.* described in a recent work,⁷⁸ there is limited basis for comparison of FoM_S values reported in the literature due to the lack of methodological standards and most contributions to this subject have been theoretical studies.^{245,248} Hence, for biointerfacial science applications, the main parameter to consider is l_d since it directly affects the probing volume and in turn influences not only measurement sensitivity but also the scope of application possibilities. Aside from directly varying the l_d value, another important aspect of nanoplasmonic sensor design is adopting appropriate surface functionalization strategies so that a large fraction of the evanescent electromagnetic field is occupied by the target biomacromolecules.

2.4. Surface functionalization

Before proceeding to discuss different examples of how nanoplasmonic sensors are being applied to study the biointerfacial sciences, a conceptual introduction to various surface functionalization strategies that are used within the field is presented. A detailed description of surface modification for nanoscale sensor applications in general is provided in ref. 249. Compared to other classes of biosensors with flat, uniform surfaces, surface functionalization of nanoplasmonic sensors is particularly challenging because the sensor surfaces are often comprised of more than one material (*e.g.*, gold nanoparticles on a glass substrate) and have curved geometrical features.⁷⁸ The selection of appropriate design choices for surface functionalization is equally important for LSPR- and EOT-based nanoplasmonic sensors.

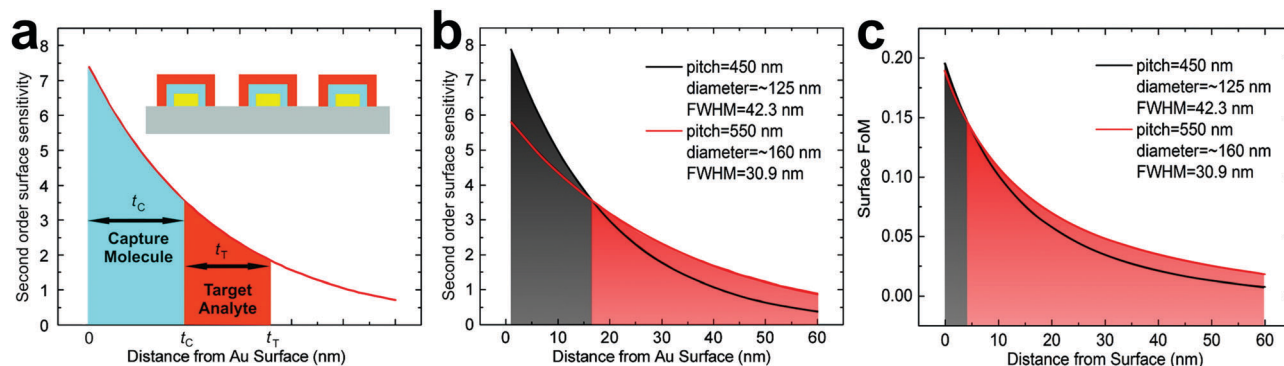


Fig. 4 (a) Second-order surface sensitivity applied for a common biosensing scheme. The thicknesses of the attached biorecognition molecule and target analyte are t_c and t_T , respectively. The blue/orange areas indicate the sensitivity to refractive index change in the thickness range specific to the capture molecule/target analyte. Comparisons of (b) the second-order surface sensitivity curve and (c) FoM_s (labeled as surface FoM) for two sensing arrays. The shadowed areas show the thickness ranges in which the curves in corresponding colors have the higher surface sensitivity or FoM_s . Reprinted (adapted) with permission from ref. 178. Copyright 2015 American Chemical Society.

These design requirements also highlight the different needs for classical detection applications *versus* emerging applications in the biointerfacial sciences. To some extent, indirect nanoplasmonic sensing platforms based on conformal layers of a dielectric coating as well as topographically flat substrates have simplified these challenges, and extensive efforts have been placed at achieving the two complementary goals of suppressing nonspecific adsorption and selectively recognizing target biomacromolecules with high sensitivity. One popular approach to achieve these goals in the biosensor field is to immobilize natural or synthetic biomacromolecules on the sensor surface in order to act as recognition molecules (receptors) that selectively bind to target molecules *via* interactions such as antibody–antibody binding and nucleic acid hybridization.

A conventional route to immobilize biomacromolecules on a sensor surface involves passive adsorption (termed “physisorption”). While the coating process is simple in this case, the resulting interactions between the biomacromolecules and sensor surface are weak (noncovalent) and can cause surface-induced denaturation and/or conformational changes that alter the biological activity (*e.g.*, recognition capabilities) of the adsorbing species.²⁵⁰ For detection applications, such features are disadvantageous for immobilizing receptors onto sensor surfaces because they often impair functionality and hence this modification strategy likely will not meet key measurement needs such as selectivity and stability. At the same time, characterizing the passive adsorption of biomacromolecules onto sensor surfaces is highly relevant to the biointerfacial sciences and a promising area of research for nanoplasmonic sensors in its own right, as explained below. Another option to immobilize biomacromolecules acting as receptors involves chemical adsorption (termed “chemisorption”) whereby specific functional groups of biomacromolecules form covalent bonds with functional groups on the sensor surface.²⁵⁰ Common functional groups that are useful for chemisorption include thiols (*e.g.*, thiolated nucleic acids²⁵¹) and sulfhydryls (*e.g.*, found in cysteine residues of proteins²⁵²). Depending on the location of these functional groups, it is possible to covalently immobilize a

particular region of the biomacromolecule to the sensor surface while leaving other biologically active regions accessible to participate in binding interactions.

An alternative modification strategy involves the immobilization of a passivation layer such as a polymer, proteins, or amphiphiles, followed by attachment of the recognition molecules *via* interactions with the passivation layer. A popular example is poly(L-lysine)-*graft*-poly(ethylene glycol) (PLL-*g*-PEG) in which case the positively charged PLL backbone noncovalently adsorbs onto negatively charged sensor surfaces (*e.g.*, silicon oxide) while the PEG chains prevent nonspecific adsorption of fouling molecules onto the sensor surface.²⁵³ Some fraction of the PEG chains can be functionalized with a chemical moiety (*e.g.*, biotin or amino groups) to facilitate covalent or noncovalent conjugation of recognition molecules.^{254,255} Protein adlayers can also be formed through covalent or noncovalent attachment schemes²⁵⁰ (and sometimes aided by a subsequent cross-linking step to stabilize bound proteins²⁵⁶), and one example is streptavidin, which can then recognize biotinylated molecules and bind to them *via* streptavidin–biotin pairing.²⁵⁷ Other options based on amphipathic molecules include self-assembled monolayers and supported lipid membranes. Self-assembled monolayers are composed of amphipathic molecules that possess appropriate functional groups to covalently bond to the sensor surface (*e.g.*, sulfhydryl groups that bind to gold surfaces) and self-assemble to form the monolayer.^{258,259} The exposed side of these molecules can possess other functional groups such as carboxylic acids to facilitate the immobilization of recognition molecules like antibodies.²⁶⁰ Supported lipid membranes such as conformal lipid bilayer coatings are another promising option as the lipid composition can be tuned to incorporate a fraction of lipids with reactive/recognition headgroups¹³³ whereas other lipids in the composition are generally resistant to nonspecific adsorption events.^{261,262}

As with inorganic coatings described above in the preceding sections, surface functionalization strategies involving biomacromolecules, especially passivation layers, inevitably affect sensing performance as the bound recognition molecules reside within the region of highest field intensity.²⁶³ Hence, thin coatings are

preferable in order to keep the region of highest field intensity accessible to analyte molecules. Another noteworthy point concerns the fact that, as the nanoplasmonic sensing field expands beyond detection applications to a broader range of biointerfacial science applications, the role of surface functionalization will continue to evolve from preventing nonspecific adsorption of interfering molecules to achieving spatial control over the location of functional biomacromolecules on the sensor surface. Indeed, there is growing attention to orthogonal strategies aimed at selectively functionalizing parts of the sensor surface based on advances in lithographic patterning, contact printing, direct writing, and material-selective functionalization among other possibilities.²⁶⁴

In the following sections, we present the latest advances in applications of nanoplasmonic sensors for quantitative biointerfacial science applications, including important foundation studies and ongoing developments for different classes of biomacromolecules interacting at solid-liquid interfaces.

3. Protein studies

This section is divided into sub-sections describing trends from the origins of nanoplasmonic sensor studies for proteins to recent developments. Table 2 presents an overview of the relevant nanoplasmonic sensing strategies, including the fundamental measurement concepts underpinning sensor design and experimental outcomes for each study.

3.1. Foundation work

Early work by the Van Duyne group involved the fabrication of noble metal nanoprisms on a substrate, which were then functionalized with a variety of protein recognition elements in order to enable detection of protein binding *via* LSPR peak shifts^{4,247,265–268} (Fig. 5a–c). Successful detection of biotin-streptavidin binding²⁴⁷ was demonstrated along with protein binding to sugars,²⁶⁸ ions^{4,266} and pharmaceutical drugs.²⁶⁵ Besides nanostructures that lie on the surface, nanoholes can also serve as plasmonic transducers. Brolo *et al.* introduced the first sub-wavelength holes in gold films for biosensing based on the EOT effect.²⁶⁹ The use of nanoholes allowed SPR detection to be performed in transmission mode. Hence, the optical arrangement was simplified and provided a smaller probing area, which led to sensor miniaturization. They showed that the wavelength of the maximum transmission of normally incident white light shifted by around 4 nm after the gold film was modified with mercaptoundecanoic acid (MUA) and further shifted around 9 nm upon the adsorption of 100 μM bovine serum albumin (BSA). On the other hand, the addition of cytochrome *c* (Cyt *c*) resulted in a shift of around 8 nm. Hence, the detection scheme enabled the first nanoplasmonic measurements of protein adsorption onto a nanohole array.

Yang *et al.* demonstrated real-time monitoring of protein binding kinetics through the use of small-dimension ordered arrays of nanoholes perforated on an ultrasurface²⁷⁰

(Fig. 5d–h). The arrays enabled multiplexed and real-time binding affinity analysis. By varying the size of the arrays between 1 to 20 μm^2 , it was discovered that increasing the gold-solution contact area results in higher plasmonic detection sensitivity. Using 1 μm^2 nanohole arrays, the authors analyzed the binding kinetics of anti-Gluthathione *S*-Transferase (GST) antibody to immobilized GST. This work paved the way for quantitative antibody screening, which has become a major theme in recent years. For example, by combining nanohole arrays with a 12-channel microfluidic flow cell and a portable spectrophotometer, Im *et al.* quantified the binding kinetics of a family of single-chain variable fragment (scFv) antibodies that bind to anthrax toxin protective antigen (PA).²⁷¹ By immobilizing PA on the gold surface and injecting the antibodies through the channels, the instrument was capable of quantifying binding kinetics at antibody concentrations as low as 1 nM. Antibodies which had similar affinities were easily differentiated because the setup could resolve different dissociation constants (K_D) ranging from 200 pM to 40 nM and dissociation rate constants (k_d) ranging from 10^{-2} to 10^{-4} s^{-1} . Aside from antibody-antigen binding, protein-protein interactions can be investigated *via* a similar measurement principle. Bhagawati *et al.* showed that by immobilizing the ectodomain of the type I interferon receptor sub-unit IFNAR2 on micropatterned gold nanoparticles, rapid association and dissociation with its ligand IFN α 2 could be quantified in real-time by LSPR measurements.²⁷² The interaction between protein and sugars can also be monitored using a similar detection format.^{268,286,290} For example, Yonzon *et al.* tracked conformational changes in concanavilin A (Con A) immobilized on silver nanoprisms upon interactions with mannose and galactose *via* LSPR extinction peak shifts.^{268,292} Kitano *et al.* have also utilized LSPR sensing to study the binding kinetics of Con A binding to mannose-presenting glycopolymer chains attached in a polymer brush configuration to gold nanoparticles on a glass substrate.²⁹¹ In another work, Nagatsuka *et al.* investigated the respective binding kinetics of ricin, Shiga toxin, and Cholera toxin with lactose, Gb3 trisaccharide and GM1, by monitoring changes in the absorbance intensity at a fixed wavelength from a non-periodic array of deposited gold nanoparticles.²⁸⁶ Since the three toxins have different molecular sizes and subunit structures and recognize different oligosaccharides, they showed that it is crucial to control the nanoparticle diameter in order to obtain the optimal response for each interaction system. As earlier discussed in the previous section, such optimization is important in nanoplasmonic sensing in order to match the electromagnetic field decay length of the plasmonic transducer to the biomacromolecular target of interest. Hence, while both LSPR- and EOT-based sensing strategies are capable of detecting protein binding, LSPR is particularly well-suited for studying protein adsorption on account of the short decay length of its electromagnetic field.

3.2. Conformational changes

Besides the quantification of protein binding through kinetic parameters, nanoplasmonic sensors also facilitate analysis of protein conformational changes in real-time. Chah *et al.* first demonstrated the exploitation of LSPR signals arising from

Table 2 Highlighted works that involve surface-based nanoplasmonic sensors for studying protein-related biointerfacial science topics

Biomacromolecules of interest	Type of interaction	Plasmonic transducer platform	Information obtained	Sensing principle	Signal readout	Ref.
Biotin-streptavidin	Protein-protein	Ag nanoprism on glass	Binding avidity (concentration dependency, thermodynamic binding constant)	LSPR	Wavelength shift of the extinction maxima	247
Mannose & galactose-concanavalin A (ConA)	Protein-sugar	Ag nanoprism on glass	Binding avidity & interaction kinetics (real-time binding kinetics)	LSPR	Wavelength shift of the extinction maxima	268
Cutinase-calmodulin-cutinase-Ca ²⁺	Protein-ion	Ag nanoprism on glass	Adsorbate properties (real-time conformational changes)	LSPR	Wavelength shift of the extinction maxima & change in extinction intensity	4
Cutinase-calmodulin-cutinase-Ca ²⁺	Protein-ion	Ag nanoprism on glass	Adsorbate properties (real-time conformational changes, dynamics & structure of protein)	LSPR	Wavelength shift of the extinction maxima	266
Human CYP3A4-several drugs (12)	Protein-drug	Ag nanoprism on glass	Binding avidity (end-point detection)	LSPR	Wavelength shift of the extinction maxima (LSPR peak shift - shift direction and magnitude)	265
BSA and Cyt c	Protein-surface (protein adsorption)	Nanohole in Au film on glass	Binding avidity (end-point detection)	EOT	Wavelength shift of the transmission maxima (transmission spectral shift)	269
GST-anti GST	Protein-protein	Nanohole in Au film on fluoropolymer	Binding avidity and interaction kinetics (real-time binding kinetics, association and dissociation rate constants)	EOT	Change in transmission intensity	270
PA-scFv family	Protein-protein	Nanohole in Au film on glass	Binding avidity and interaction kinetics (real-time binding kinetics, association and dissociation rate constants)	EOT	Wavelength shift of the transmission maxima	271
IFNAR2-H10-IFN α 2	Protein-protein	Au nanoparticle on glass	Binding avidity and interaction kinetics (real-time binding kinetics, association and dissociation rate constants)	LSPR	Change in reflectance intensity at fixed wavelength	272
c-myc peptide-anti-c-myc antibody	Protein-protein	Au nanodisk on glass	Interaction kinetics (real-time kinetic mapping, fractional occupancy)	LSPR	Change in transmission intensity, brightness changes <i>via</i> LSPR and transmitted light imaging	273
Biotin-antibiotin	Protein-protein	Ag nanoprism on glass	Binding avidity (concentration dependency, thermodynamic binding constant)	LSPR	Wavelength shift of the extinction maxima	267
BSA	Protein-surface	Nanohole in Au film on silicon nitride	Binding avidity and interaction kinetics (real-time binding kinetics)	EOT	Wavelength shift of the transmission maxima	224
Biotin-streptavidin	Protein-protein	Nanohole in silicon oxide-Au film on glass	Binding avidity (end-point detection)	EOT	Wavelength shift of the transmission maxima	274
Biotin-streptavidin	Protein-protein	Nanohole in Au film on glass	Binding avidity and interaction kinetics (real-time binding kinetics)	EOT	Change in transmission intensity	236
Biotin-streptavidin, AFP, PSA	Protein-protein, protein detection	Au nanorod on glass	Binding avidity and interaction kinetics (real-time binding kinetics, concentration dependency)	LSPR	Wavelength shift of the extinction maxima	275
Antibiotin-biotin	Protein-protein	Au nanodisk on glass	Binding avidity (end-point detection, concentration dependency)	LSPR	Wavelength shift of the extinction maxima	166
BSA	Protein corona formation	Au core-silica shell nanoparticle on fused silica	Interaction kinetics (real-time adsorption kinetics)	LSPR	Wavelength shift of the extinction maxima	276
BSA, IgG, bovine serum, IgG-depleted bovine serum	Protein corona formation	Au core-silica shell nanoparticle on fused silica	Interaction kinetics (real-time adsorption kinetics)	LSPR	Wavelength shift of the extinction maxima	277
Biotin-avidin	Protein-protein	Nanohole in Au film on glass	Binding avidity and interaction kinetics (real-time binding kinetics)	EOT	Wavelength shifts of extinction peak & minima	209
Phosphorylation of myelin basic protein (MBP) by PKC- α in presence of ATP-S	Protein phosphorylation	Au nanoparticles added post-reaction on glass	Binding avidity (end-point detection)	LSPR	Wavelength shift of the extinction maxima	278
IgG-A/G	Protein-protein	Nanohole in Au film on SiN on glass	Binding avidity and interaction kinetics (real-time binding kinetics, association and dissociation rate constants)	EOT	Wavelength shift of the extinction maxima	203

Table 2 (continued)

Biomacromolecules of interest	Type of interaction	Plasmonic transducer platform	Information obtained	Sensing principle	Signal readout	Ref.
Complex protein matrix-polyphenols (PGG, B3, catechin) PGG- α amylase	Protein-small molecule Protein-small molecule	Molecular imprinted polymer-coated Au nanodisk on glass Au nanodisk on glass	Binding avidity (binding affinities)	LSPR	Wavelength shift of the extinction maxima	279
β -Ionone-OBP	Protein-small molecule	Nanohole in Au film on (poly)ethylene terephthalate decorated with Au nanoparticles Au nanoparticle on glass	Binding avidity and adsorbate properties (end-point detection, concentration dependency and conformational changes) Binding avidity (end-point detection, concentration dependency)	LSPR	Wavelength shift of the extinction maxima	280
IL10, MMP-3, TNF- α , BSA, anti-biotin, streptavidin Biotin-streptavidin	Protein-protein Protein-protein	Nanohole in Au film on glass Au nanoparticle on glass	Binding avidity (end-point detection, concentration dependency) Binding avidity (end-point detection)	LSPR	Wavelength shift of the absorbance maxima	282
Biotin-streptavidin	Protein-protein	Nanohole in Au film on glass	Binding avidity (end-point detection)	EOT	Wavelength shift of the transmission maxima	230
Biotin-streptavidin	Protein-protein	Nanohole in Au film on glass	Binding avidity and interaction kinetics (real-time binding kinetics)	EOT	Change in transmission intensity (pixel intensity)	283
Biotin-streptavidin	Protein-protein	Nanohole in Au film on glass, with Bragg mirrors	Binding avidity and interaction kinetics (real-time binding kinetics)	EOT	Change in transmission intensity (pixel intensity)	284
BSA	Protein-surface (protein adsorption) Protein-sugar	Nanohole in Au film on glass Au nanoparticle on glass	Binding avidity and interaction kinetics (real-time binding kinetics, association and dissociation rate constants) Binding avidity and interaction kinetics (real-time binding kinetics)	LSPR	Wavelength shift of the transmission maxima	285
Ricin-lactose, Shiba Toxin 1 (Stx1-1)-Glb3 trisaccharide, CTX-GM1 Biotin-avidin, anti-5-FU-5-FU BSA	Protein-protein, protein-small molecule Protein-protein (antibody-antigen) Protein-small molecule	Au nanoparticle on porous Al ₂ O ₃ on Al Ag nanoprism on glass	Binding avidity (end-point detection, concentration dependency)	LSPR (iLSPR)	Change in reflectance intensity at fixed wavelength	287
NU-1 antibody-ADDL	Protein-protein (antibody-antigen)	Ag nanoprism on glass	Binding avidity and interaction kinetics (real-time binding kinetics)	LSPR	Wavelength shift of the extinction maxima	288
α -Synuclein (<i>wt</i>)-EGCG	Protein-small molecule	Au nanopyrramids on ITO	Adsorbate properties (real-time conformational changes)	LSPR	Wavelength shift of the extinction maxima	289
Concanavilin A (Con A)-mannose	Protein-sugar	Au island films on glass	Binding avidity and interaction kinetics (real-time binding kinetics, association and dissociation rate constants)	LSPR	Change in extinction intensity	290
Con A-mannose	Protein-sugar	Au nanoparticle on glass	Binding avidity and interaction kinetics (real-time binding kinetics, association and dissociation rate constants)	LSPR	Change in absorbance intensity at fixed wavelength	291
IgG, PSA antibodies, MTX-hDFHR	Protein-protein, protein-drug	Nanohole in Au film on glass	Binding avidity (end-point detection, concentration dependency)	EOT	Wavelength shift of the transmission minima	229

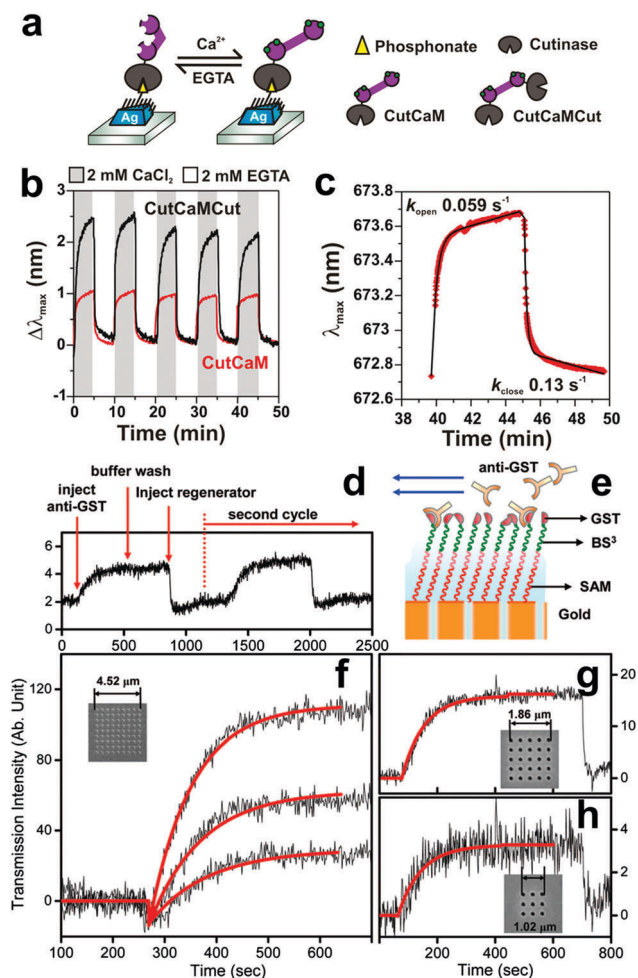


Fig. 5 (a) Schematic representation of the reversible conformational changes calmodulin undergoes in response to changing calcium concentration. In the presence of calcium (green circles) calmodulin adopts a rigid, extended structure. (b) Reversible conformational changes of calmodulin recorded as LSPR λ_{max} variations over time. LSPR response corresponding to calmodulin conformational changes as a result of interaction with CutCaM (red trace) is compared to conformational changes due to interaction with CutCaM/Cut construct (black trace). (c) Fitted data (based on first-order kinetics) of CutCaM-induced λ_{max} changes occurring between 40 and 50 min from the plot in (b). Reprinted (adapted) with permission from ref. 4. Copyright 2011 American Chemical Society. (d) Sensing response upon injecting 615 nM anti-GST and subsequently the regenerator. (e) Schematic illustration of surface chemistry on nanohole arrays (drawing not to scale). (f) Sensing response (black plot) of a 9 × 9 nanohole array ($d = 200 \text{ nm}$, $P = 540 \text{ nm}$) upon injecting three different concentrations of anti-GST. Red plot: fitting with a bimolecular reaction model. (g) Sensing response (black plot) of a 5 × 5 nanohole array ($d = 180 \text{ nm}$, $P = 419 \text{ nm}$) upon injecting 615 nM anti-GST and subsequently the regenerator. (h) Sensing response (black plot) of a 3 × 3 nanohole array ($d = 180 \text{ nm}$, $P = 419 \text{ nm}$) upon injecting 615 nM anti-GST and subsequently the regenerator. Reprinted (adapted) with permission from ref. 270. Copyright 2008 American Chemical Society.

gold nanoparticles for detection of protein conformational changes.²⁹³ They first covalently attached Cyt *c* to the surface of gold nanoparticles. Since Cyt *c* unfolds at low pH and refolds at high pH, changes in pH caused measurable shifts in the LSPR signals obtained *via* a standard UV-vis spectrophotometer.

More importantly, the extinction peak shifts were manifested as changes in the color of the gold nanoparticle solution, allowing direct real-time monitoring of the folding-related conformational changes. Similarly, Teichroeb *et al.* studied the thermal denaturation of BSA adsorbed on gold nanoparticles by plotting the extinction peak shifts against time when the sample was incubated at an elevated temperature (60–70 °C).²⁹⁴ By doing so, they were able to determine the fraction of thermally denatured proteins after a certain period of duration, and found that the denaturation kinetics vary depending on nanoparticle size. In addition, as presented in Fig. 5a–c, Hall *et al.* demonstrated the detection of Ca²⁺-induced conformational changes of calmodulin immobilized on silver nanoprisms.⁴ The conformational changes produced a detectable and reversible shift in the LSPR extinction maximum, with a signal-to-noise ratio of *ca.* 500. The limit of detection for Ca²⁺ ions was 23 μM in the system.

Recently, nanoplasmonic sensing techniques have been employed in combination with mass spectroscopy and electrochemical techniques for protein sensing, leading to detailed insights into protein conformational changes. The work by Anker *et al.* represents one of the earlier demonstrations of this kind when they combined LSPR with matrix assisted laser desorption ionization mass spectrometry (MALDI-MS) to study the binding kinetics of NU-1 antibody with amyloid-beta derived diffusible ligands (ADDL).²⁸⁸ In brief, LSPR provided real-time detection of the molecular adsorption event while MALDI-MS enabled identification of the adsorbed molecules. In a separate contribution, Guerreiro *et al.* combined LSPR with circular dichroism spectroscopy (CD) to probe conformational changes associated with pentagalloyl glucose (PGG) binding to amylase.²⁸⁰ Gold nanodisks acted as both LSPR transducers as well as chiral sensors, which allowed *in situ* measurement of conformational changes for bound amylase acquired indirectly *via* plasmonically enhanced CD spectroscopy. The chirality changes were correlated to structural alterations of the amylase observed upon PGG binding. On a side note, the combination with CD spectroscopy also enabled investigations into the differences in structural transformations associated with PGG-amylase binding in solution *versus* binding on a substrate. More recently, nanoplasmonic sensing techniques have also been combined with electrochemical sensing techniques. For example, in monitoring the conformational change associated with the interaction between α -synuclein (αs) oligomers and (–)-epigallocatechin-3-gallate (EGCG), Cheng *et al.* obtained cyclic voltammetry (CV) and differential pulse voltammetry (DPV) signals alongside LSPR peak shifts.²⁸⁹ The aggregation of αs oligomers was characterized electrochemically using the redox probe $[\text{Fe}(\text{CN})_6]^{3-/4-}$, before being confirmed by the LSPR measurements. Lazar *et al.* combined LSPR with electrochemical impedance spectroscopy (EIS) to study the real-time kinetics of nonspecific BSA adsorption on nanohole arrays to determine the association–dissociation rate constants.²⁸⁵ Through the combined system, they concluded that the origin of LSPR signals strongly depends on the surface coverage and can be specified by simultaneously carrying out EIS measurements. Hence, there is broad potential for utilizing nanoplasmonic

sensors to track protein conformational changes in independent and combined measurement formats.

3.3. Improvements in detection sensitivity

Over the past few years, significant effort has also been invested to continually improve the sensitivity of nanoplasmonic sensing platforms for protein detection. Li *et al.* recently conducted a fundamental study, which showed that the refractive index of the substrate plays a central role in determining the measurement sensitivity of the platform.²⁴⁴ They recommended the use of a low refractive index polymer coating in order to obtain LSPR spectra with a narrow FWHM. They also proposed the use of a second-order derivative model over the conventional exponential decay length model (see also Section 2.3) in order to explain the sensitivity of isolated nanostructures. Several enhancement strategies have also been proposed including the use of nanoparticle-antibody conjugates. By labelling antibodies with gold nanoparticles, binding to antigens immobilized on plasmonic nanostructures resulted in an enhancement of up to 400% in terms of the LSPR peak shift magnitude,²⁶⁷ as reported by Hall *et al.* using a biotin-antibody pair. This improvement translates into an increase in binding constant by 2 orders of magnitude and a decrease in the limit-of-detection by nearly 3 orders of magnitude. The increase in binding constant is interestingly due to a polyvalency effect whereby polyvalent antibodies bind to the antigen with higher affinity than monovalent antibodies. In this case, it was found that the binding of gold nanoparticles to the nanostructures is mediated by more than one antibody molecule. In a similar fashion, Bellapadrona *et al.* reported enhancement in the signal-to-noise by using secondary binding of gold nanoparticle-labelled mannose, during the real-time monitoring of concanavilin A (which has 4 carbohydrate binding sites) binding to mannose immobilized on gold island films.²⁹⁰ The secondary binding of gold nanoparticles also allowed confirmatory visual inspection of the protein-sugar interaction by electron microscopy. In a slightly different detection format, the use of gold nanoparticle labelling has also been recently coupled to a field-effect transistor device by Bhalla *et al.* in order to study protein phosphorylation, kinase activity, and inhibition.²⁷⁸ In this case, the target protein (myelin basic protein, MBP) is directly bound to the glass substrate instead of a surface-bound metallic nanostructure. In other words, the gold nanoparticles act as nanoplasmonic transducers and are introduced only after the detection is completed to provide an on-off LSPR signal.

Besides nanoparticle labelling, sensitive responses can be obtained by directed binding of the biomacromolecule of interest at the most sensitive regions of the nanoplasmonic transducer such as the tips of anisotropic nanostructures as well as in the gap between adjacent nanoparticles, otherwise known as the 'hot-spot' regions.²⁹⁵⁻²⁹⁷ The LSPR signal can also be enhanced by changing the sensing platform architecture, which alters the dielectric environment around the nanoplasmonic transducers.^{287,298-300} For example, Hiep *et al.* reported that placing gold nanoparticles on a porous alumina resulted in the coupling of plasmon bands with interference bands, which enhances changes in the LSPR band.²⁸⁷ They

referred to this method as interference LSPR (iLSPR) and characterized their platform using the model protein interaction between biotin-streptavidin, before employing it to study the interactions between the anti-5FU antibody and 5FU-BSA. They found that the degree of enhancement can be tailored by controlling the thickness of the porous alumina layer. Another advantage of the plasmonic technique related to the dielectric environment is the ability for the plasmonic transducers to be coated with an adsorbing material of interest. This was recently exploited by Guerreiro *et al.* to obtain molecular imprinted polymers on gold nanodisks in order to study the binding interactions of polyphenols with a complex matrix of proteins.²⁷⁹ An advantage of coating the nanodisk with the molecular imprinted polymer is the ability to study interactions from a complex mixture of proteins in a quasi-three-dimensional format with a potentially higher measurement response.

To increase the performance of the nanoplasmonic sensing platform based on the nanohole format, Cetin *et al.* recently developed nanohole arrays on a Si₃N₄-glass hybrid substrate.²⁰³ By having Si₃N₄ as a high refractive index interlayer between the nanohole array and glass, the plasmonic resonances become more well-defined and easy to track. Indeed, using the high refractive index substrate led to higher RI sensitivity and contributed a useful design strategy for periodic nanoholes in general. Specifically, the inclusion of this layer minimized interfering plasmonic modes, which is a common challenge when using typical low refractive index, transparent materials in conventional nanohole platform designs as discussed above. They utilized it to study the IgG-A/G protein-protein interactions and demonstrated real-time monitoring of the binding interactions at sub 1 ng mL⁻¹ levels. In another approach, Lindquist *et al.* designed Bragg mirrors surrounding isolated nanohole arrays to reduce signal interference and cross-talk, and demonstrated, through real-time interactions between biotin and streptavidin, that the response sensitivity is maintained even when the size of the arrays is varied.²⁸⁴ The interior of the nanoholes can also be decorated with nanoparticles. This format was utilized by Zhang *et al.* to observe the binding of olfactory binding proteins (OBP) to β -ionone in a high-throughput manner.²⁸¹ They observed synergistic LSPR effects between the periodic array structure and nanoparticles deposited within the nanoholes, resulting in a bulk sensitivity of $\sim 10^4$ nm wavelength shift per refractive index unit change. With respect to sensor miniaturization, identifying optimal ways to utilize simple and reliable instrumentation is another important consideration alongside designing systems with excellent detection capabilities. Along this line, Escobedo *et al.* reported the use of a dual color LED light source illuminating a nanohole array structure.²⁸³ The responses from the two sources move in opposite directions during the detection of a protein binding event resulting in the elimination of drift and bulk scattering effects.

3.4. Biological applications

Another emerging application of protein binding on nanostructure arrays is the spatial and temporal mapping of protein secretion from cells. Conventional methods use fluorescent

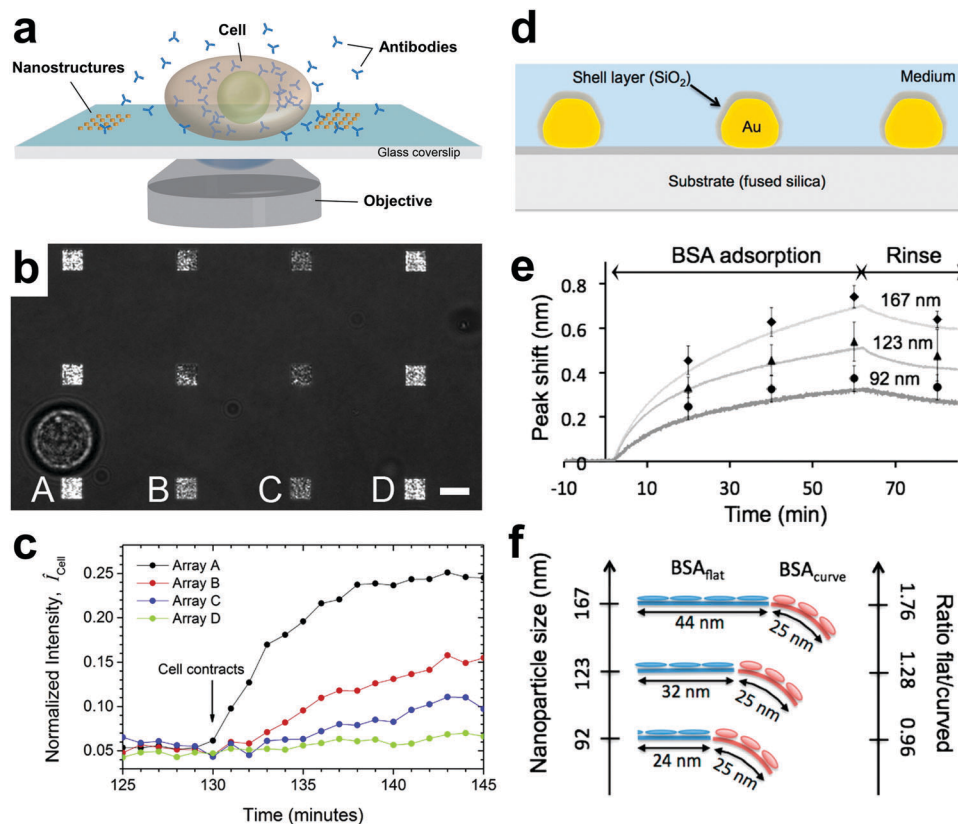


Fig. 6 (a) Illustration of an antibody-secreting cell in registry with two nanoplasmonic arrays. The chip is loaded onto an inverted microscope and the fact that the majority of the substrate is transparent glass allows for live cell imaging using transmitted light and fluorescence microscopy in parallel with the LSPR-based imaging technique used to measure the secretions. (b) Overlay of LSPR and transmitted light images with the cell visible next to Array A as a result of the transmitted light illumination, whereas the nanoplasmonic arrays are illuminated in LSPR mode. (c) Real-time variations in normalized LSPR image intensity of Arrays A–D. Reprinted from ref. 273. Copyright 2013, with permission from Elsevier. (d) Schematic representation of plasmonic core-shell nanoparticles on a sensor chip fabricated by annealing low-aspect-ratio truncated Au nanocones into faceted sphere-like particles and by subsequently coating them with a thin SiO₂ layer. Each of the core-shell nanoparticles serves two functions; as a nanoplasmonic sensing element and a mimic of dielectric engineered nanomaterials in bulk solution. (e) Real-time responses during the adsorption of BSA to the core-shell nanoparticles of different size and subsequent buffer rinse. The average response and standard deviation are indicated after 20, 40, 60, and 80 min. Each experiment was repeated three times. (f) Schematic of BSA adsorbed to flat and curved regions of the nanoparticle surfaces. Reprinted (adapted) with permission from ref. 276. Copyright 2016 American Chemical Society.

and colorimetric probes with time resolution ranging from several hours to days, hampering investigations on shorter time scales. Raphael *et al.* demonstrated the label-free, real-time mapping of antibody secretions from single hybridoma cells²⁷³ using a methodology they earlier developed¹⁶⁵ (Fig. 6a–c). In brief, secreted anti-c-myc antibodies are detected when they bind to c-myc peptides conjugated to plasmonic gold nanostructures. This method enabled the determination of fractional occupancy of binding sites as a function of time based upon LSPR kinetic measurements from an array of nanostructures. These measurements were performed based on the principle that the plasmon resonance of a metallic nanostructure exhibits both a redshift and an increase in scattering intensity when an analyte binds to the surface. When imaged on a charge-coupled device (CCD) camera, these signatures appear as an increase in brightness—therefore, the higher the fractional occupancy, the brighter the image. Changes in image brightness allowed protein secretions to be measured in real-time with a recording frequency limited only by the exposure time of the camera (typically 250–400 ms).

Beyond their significance for important biotechnology and clinical applications, proteins have also served as a useful model system to validate the measurement capabilities of nanoplasmonic sensors before extending to more complex systems involving larger biomacromolecules and self-assembled aggregates. Very recently, Frost *et al.* reported an experimental LSPR study of protein corona formation on a sensor chip surface²⁷⁶ (Fig. 6d–f). This work was achieved by preparing gold core-silica shell nanoparticles of different sizes on a fused silica substrate. The approach enabled the *in situ* monitoring of both corona formation as well as possible changes in the adsorbate properties upon incubation in biological environments. Compared to studying corona formation in the liquid phase (*i.e.*, in suspension), the LSPR approach allowed measurements to be conducted under controlled flow conditions. An important implication is the convenience and efficiency for nanoparticle surface modification. Unlike in solution, the nanoparticles do not have to be subjected to a purification step post-modification, which can itself affect the corona formation process. In turn,

these advantages allowed Frost *et al.* to discover the importance of facet-to-edge ratios in corona formation on nanoparticles of different sizes as well as the effectiveness of silanization in preventing BSA adsorption. This approach has also been extended to comparing the adsorption kinetics of BSA and IgG as well as protein adsorption in more complex biological fluids.²⁷⁷ It was found that the initial rate of IgG adsorption increased with larger nanostructure size (greater flat/curved area ratio), whereas this size-dependent effect was not observed with BSA. Xiong *et al.* have also shown that, with decreasing nanohole diameter, the sensitivity to Neutravidin binding within the nanohole became greater even though the bulk refractive index sensitivity was unaffected by the nanohole diameter.²⁰⁹

3.5. Multiplex capabilities

With regards to the use of nanoholes, a comparison between flow-through and flow-over configurations was performed by Escobedo *et al.*²²³ They found that the flow-through nanohole format significantly increased the flux of analytes to the sensing surface. This leads to flow-through nanohole arrays offering around 10-fold improvement in response time for conventional types of binding kinetics and analytes. In a follow-up work, flow-through nanohole arrays were subjected to an applied electric field in order to actively concentrate analytes prior to sensing.²²⁴ This is achieved through a combination of electric field gradient focusing (EFGF) as well as a bulk pressure-driven flow bias. They used this scheme to detect the binding of bovine serum albumin (BSA) on the sensing surface and found that the time to reach equilibrium is 10 times faster compared to a control experiment (*i.e.*, without applied potential). In addition, the magnitude of the plasmonic peak shift also increased by 5-fold. The detection of protein binding inside the nanoholes was also explored by Ferreira *et al.*, in which attomolar sensitivity was achieved.²⁷⁴

Recent efforts have also been aimed at developing multi-channel arrays with integrated microfluidics capable of high-throughput and multiplex sensing.^{166,236,275,289,301–304} The fact that nanoplasmonic transducers can be easily fabricated or deposited on glass or polymeric substrates implies that they can be conveniently adapted in currently established automated imaging platforms such as the plate reader. For example, He *et al.* demonstrated the integration of the nanoplasmonic sensing platform with microfluidics by adhering PDMS over nanostructures on glass and also fabricated a customized wall-less 96-well plate that is compatible with a conventional plate reader.²⁸² The platform was capable of simultaneously detecting a variety of proteins. Taking a step further, Couture *et al.* recently developed a multiplex plasmonic sensing platform for protein detection and drug screening, which consists of a custom 96-well plate with periodic nanohole arrays as well as a custom plate reader designed to analyze the nanohole arrays at high incident angles for increased sensitivity²²⁹ (Fig. 7). Such capabilities are relevant both for pharmaceutical as well as diagnostic applications, specifically for the development of miniaturized biosensor platforms capable of point-of-care detection. A relevant example of the latter within the context of this review

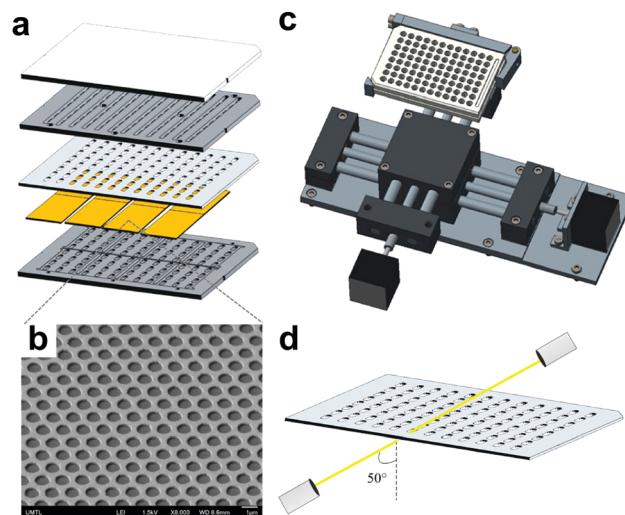


Fig. 7 (a) Design of the custom multiwell plate. From top to bottom: plexiglass slide, top aluminum part, PDMS spacer, sensors, and bottom aluminum part. (b) SEM image of the nanohole arrays. (c) Schematic of the multiwell plate reader. (d) Excitation of the multiwell plate in transmission with an incident angle of 50°. Reprinted (adapted) with permission from ref. 229. Copyright 2016 American Chemical Society.

is the work by Cappi *et al.*, which addresses end-point detection, biointerfacial kinetic analysis as well as instrumentation miniaturization.³⁰⁵ They developed a palm-sized transmission LSPR platform for the detection of the antibiotic tobramycin from serum using aptamer-functionalized gold nanoislands on a glass substrate. Besides obtaining the concentration dependent response, they also demonstrated the real-time monitoring of the association and dissociation of tobramycin recognized by the aptamer. Collectively, the findings point to continually advancing progress in the use of nanoplasmonic sensors for protein binding studies across both LSPR- and EOT-based measurement schemes.

4. Lipid membrane studies

Table 3 presents an overview of nanoplasmonic sensor studies that involve lipid membranes, including vesicle adsorption and rupture leading to supported lipid bilayer (SLB) formation as well as vesicle adsorption without rupture. Collectively, these studies highlight the capabilities of nanoplasmonic sensors to probe the dynamics of soft matter adsorbates.

4.1. Supported lipid bilayer formation

Aside from protein studies, another popular subject involves studying the formation of lipid membrane coatings on nanostructures. The design of supported lipid membrane platforms on nanoplasmonic sensors requires a delicate approach due to the geometrical and material properties of the sensing platform. The most common way to fabricate supported membrane platforms is the adsorption and spontaneous rupture of lipid vesicles after reaching a critical surface coverage.³⁴ Typically, lipid vesicles adsorb but do not rupture on noble metal surfaces and also require a critical coverage of adsorbed vesicles.³²² In the earliest

Table 3 Highlighted works that involve surface-based nanoplasmonic sensors for monitoring structural transformations associated with lipid membrane fabrication

Lipid membrane structure	Biointerfacial event	Plasmonic transducer platform	Key insights from nanoplasmonic sensing	Ref.
Intact vesicles & vesicles to SLB	Vesicle trapping and SLB formation by Ca ²⁺ addition	Nanohole in Au film on silicon oxide	Bottom of nanohole provides most sensitive response to lipid mass accumulation.	306
Single, intact vesicles	Site-selective immobilization of single tethered vesicles <i>via</i> complementary DNA strand binding	Nanohole in Au film on silicon oxide	Lower signal from single vesicle attachment inside nanohole than from SLB formation at bottom of nanohole.	307
Single, intact vesicles	Localization of single vesicles <i>via</i> interaction between biotinylated vesicles-streptavidin coated nanostructure	Embedded Au nanomenhirs in silicon nitride film	Positional information about attached intact vesicles.	308
Vesicles to SLB	SLB formation <i>via</i> spontaneous vesicle rupture	SiO ₂ -coated nanohole in Au and Ag film	Structural changes detectable through a characteristic shape of the temporal variation in the LSPR signal.	309
Vesicles to SLB	SLB formation <i>via</i> spontaneous vesicle rupture	SiO ₂ -coated nanohole in Au film	Determination of the critical surface coverage of adsorbed vesicles and relationship to the acceleration kink.	310
Vesicles to SLB	SLB formation <i>via</i> spontaneous vesicle rupture	SiO ₂ -coated Au nanodisk on glass	Signature kink in the temporal variation in the LSPR signal is associated with the onset of vesicle rupture on nanodisk array.	311
Vesicles to SLB	SLB formation <i>via</i> spontaneous vesicle rupture	Embedded Au nanodisk in optical epoxy with SiO ₂ coating	Can form SLBs on topographically flat silica surfaces with embedded nanostructures that facilitate LSPR tracking of protein binding.	133
Vesicles to SLB	SLB formation <i>via</i> spontaneous vesicle rupture	Embedded Au nanodisk with SiO ₂ coating	Compared SLB formation with embedded and protruding nanostructures, including effects on surface sensitivity.	130
Intact vesicles & vesicles to SLB	Intact vesicle adsorption and SLB formation <i>via</i> spontaneous vesicle rupture and AH peptide-induced vesicle rupture	Bare, SiO ₂ - and TiO ₂ -coated Au nanodisk on glass	LSPR measurements are influenced by membrane architecture and location of lipid mass accumulation.	312
Intact vesicles	Intact vesicle adsorption	TiO ₂ -coated Au nanodisk on glass	Influence of lipid concentration and vesicle size on vesicle adsorption in different coverage regimes.	183
Intact vesicles	Intact vesicle adsorption, temperature-dependent membrane phase state	TiO ₂ -coated Au nanodisk on glass	Increasing temperature may promote, hinder or have negligible effect on deformation of adsorbed vesicles.	313
Intact vesicles	Intact vesicle adsorption on different substrates	SiO ₂ - and TiO ₂ -coated Au nanodisk on glass	Quantitative measurement of the extent of vesicle deformation on silicon oxide <i>versus</i> titanium oxide.	314
Intact vesicles	Intact vesicle adsorption in the presence of divalent cations	SiO ₂ - and TiO ₂ -coated Au nanodisk on glass	Divalent cations promote increased deformation of adsorbed vesicles on both silicon oxide and titanium oxide.	315
Intact vesicles	Intact vesicle adsorption in the presence of increasing osmotic pressure, influence of membrane phase state	TiO ₂ -coated Au nanodisk on glass	Greater positive osmotic pressure increases vesicle deformation for fluid-phase lipid vesicles, but not gel-phase lipid vesicles.	316
Intact vesicles & vesicles to SLB	Intact vesicle adsorption and AH peptide-induced SLB formation	TiO ₂ -coated Au nanodisk on glass	Different time scales for SLB formation and complete release of bound water to bulk during vesicle rupture and SLB formation.	317
Intact vesicles	Intact vesicle adsorption	TiO ₂ -coated Au nanodisk on glass	Description of competition between steric effects and vesicle deformation during adsorption of intact vesicles.	318
Intact vesicles	SLB formation <i>via</i> spontaneous vesicle rupture	Silicate-coated Au nanoparticles on glass	SLB formation on monolayer of silicate-coated Au nanoparticles is feasible, but slower than on smooth surface.	319
Intact vesicles	Intact vesicle adsorption and ionic liquid (IL)-induced vesicle deformation	SiO ₂ - and TiO ₂ -coated Au nanodisk on glass	Observed IL binding to supported lipid membranes and membrane destabilization, including deformation in the case of lipid vesicles.	320
Vesicle to SLB	SLB formation <i>via</i> spontaneous vesicle rupture	SiO ₂ -coated Au nanodisk on glass	Variations in the separation distance between bilayer and substrate can be characterized down to the sub 1 nm level.	321

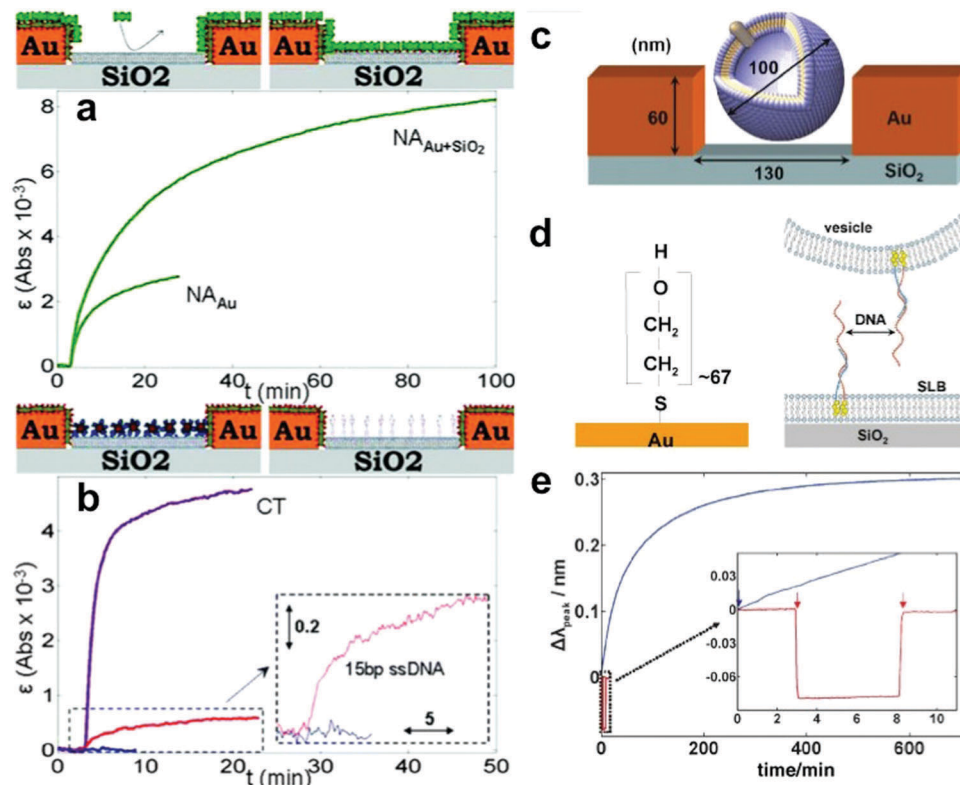


Fig. 8 (a) Temporal variation in extinction measured at the longer wavelength inflection point (725 nm) of the LSPR peak upon addition of NeutrAvidin, (NA, 0.3 μM). In both cases, Au is modified with biotin-BSA. In one case, biotin-modified SPB patches cover the SiO_2 regions ($\text{NA}_{\text{Au}+\text{SiO}_2}$), while in the other, bare SPB patches cover the SiO_2 regions (NA_{Au}). After SPB formation, EDTA (10 mM) was added to remove Ca^{2+} prior to subsequent addition steps. (b) Addition of cholera toxin (CT, 0.5 μM) to GM1-modified (5 wt%) SPBs. The inset shows a magnification of changes in extinction versus time upon addition of a 15-base long noncomplementary (0.2 μM , blue) and a fully complementary strand (0.2 μM , red) to SPB patches modified with a DNA construct carrying two cholesterol moieties at its one end and a 15-base-long single strand available for hybridization at the other. Reprinted (adapted) with permission from ref. 306. Copyright 2005 American Chemical Society. (c–e) LSPR data of DNA-hybridization mediated vesicle binding to nanoholes. (c) Schematic of a vesicle bound inside a nanohole. (d) Thiol-PEG specifically makes Au inert to vesicle binding while lipid bilayer patches can be formed (using smaller vesicles) on the bottom of the nanoholes. Cholesterol-modified DNA sequences were then used to bind vesicles to bilayers inside holes through hybridization. (e) LSPR response (peak shift) when DNA-modified vesicles (400 $\mu\text{g mL}^{-1}$, ~ 100 nm diameter) were added to a functionalized nanohole surface. In red is shown the response for vesicles with noncomplementary DNA, added at $t = 3$ min, followed by rinsing at $t = 8$ min. Response from ~ 100 nm vesicles with complementary DNA (just introduced at $t = 0$) is shown in blue. Reprinted (adapted) with permission from ref. 307. Copyright 2008 Wiley-VCH.

report of its kind, Dahlin *et al.* demonstrated the formation of supported lipid bilayers within nanoholes in a thin gold film on a glass substrate³⁰⁶ (Fig. 8a and b). As part of the design strategy, the lipid vesicles were directed to adsorb inside the nanoholes by first blocking the gold surfaces with BSA protein while leaving exposed the silicon oxide surface. One challenge with the nanohole design was that only one vesicle could reside inside the hole, thereby restricting the possibility for vesicle-vesicle interactions to trigger vesicle rupture. To overcome this challenge, the team added Ca^{2+} ions as a fusogenic agent to promote vesicle rupture and bilayer formation. Several successful examples of macromolecular binding, including proteins and nucleic acids, to functionalized variants of the supported lipid bilayer were demonstrated.

Going one step further to demonstrate site-selective immobilization of single, tethered vesicles inside the nanoholes, Dahlin *et al.* employed a thiol-functionalized polymer in order to coat the gold surface and strictly block vesicle adsorption outside the nanoholes³⁰⁷ (Fig. 8c–e). In this case, a DNA-

functionalized supported lipid bilayer was formed on the silicon oxide substrate at the bottom of the nanohole. Then, lipid vesicles functionalized with complementary DNA strands were tethered to the supported lipid bilayer through passive adsorption and complementary DNA strand binding. This platform established the successful immobilization of intact, single lipid vesicles inside nanoholes, thereby demonstrating that either supported lipid bilayers or intact vesicles can be controllably formed inside nanoholes. Kumar *et al.* have also introduced dual-mode plasmonic sensing arrays for lipid membranes by embedding asymmetric gold nanomenhirs within a silicon nitride matrix.³⁰⁸ The asymmetric structure gave rise to multiple plasmon modes and each one amplified the evanescent electromagnetic field in different regions of the nanomenhir structure, with one mode sensitive to the bottom and walls of the nanocavity and the other mode sensitive to the top and center of the nanocavity. As a result, the platform was able to localize the attachment of biotinylated vesicles to the tip of the streptavidin-coated nanomenhir. Positional sensing was demonstrated by a

large redshift in the excitation peak at the tip compared to a small blueshift at the base.

In order to overcome the challenges of working with lipid vesicles on noble metal surfaces, there has also been extensive effort to fabricate thin, conformal layers of silicon oxide on top of the nanoplasmonic sensing substrates as described above. Silicon oxide is typically chosen because it promotes spontaneous rupture of adsorbed vesicles. Using a shallow nanohole configuration fabricated from gold or silver thin films, Jonsson *et al.* demonstrated the successful formation of a supported lipid bilayer across the entire silicon oxide-coated nanoplasmonic substrate in both cases.³⁰⁹ A very interesting aspect of their work was a notable acceleration in the rate of change of the peak shift increase which was tracked in real-time during the vesicle adsorption process. Considering that the rate of vesicle adsorption is limited by bulk diffusion, the authors attributed the observed rate acceleration to vesicle rupture whereby the average net mass of adsorbed lipids moved nearer to the sensor surface which has a higher sensitivity. This result was the first demonstration of a nanoplasmonic sensor detecting a structural transformation in a macromolecular assembly. In a follow-up study, Jonsson *et al.* developed an integrated system for simultaneous nanoplasmonic and QCM-D measurements.³¹⁰ This combined platform identified that vesicle rupture simultaneously occurs inside the nanoholes and on the planar surface between the nanoholes, and also enabled measurement of the critical surface coverage of adsorbed vesicles. These findings were uniquely observed with the nanoplasmonic sensor on account of its high surface sensitivity.

Similar approaches involving conformal layers of silicon oxide have also been devised for tracking vesicle adsorption and rupture on gold nanodisks. Using hole-mask colloidal lithography, Larsson *et al.* fabricated an array of well-separated deposited gold nanodisks on a glass substrate, followed by coating with a thin silicon oxide layer.³¹¹ Vesicle adsorption could be tracked in real-time and an acceleration in the rate of the LSPR signal increase was observed during vesicle rupture, indicating vesicle rupture and bilayer formation. While most nanoplasmonic sensor substrates have complex surface topographies, Jose *et al.* creatively developed topographically flat substrates based on embedded nanoplasmonic transducers.¹³³ This nanoplasmonic sensing platform was achieved by using a template-stripping technique whereby metallic nanodisks are embedded in an optical epoxy layer, which is ultimately coated with a thin silicon oxide layer by atomic layer deposition. A supported lipid bilayer was formed on the topographically flat substrate and the formation process was tracked by changes in the LSPR peak shift signal. Comparison of bilayer formation on silica-coated surfaces with embedded *versus* protruding gold nanodisks has also been recently reported and the results showed larger measurement responses associated with bilayer formation in the case of protruding nanostructures.¹³⁰ The difference was attributed to the lower sensing volume afforded when the nanostructures are embedded. Based on the aforementioned collection of studies, there are extensive capabilities available to fabricate supported lipid membranes on nanoplasmonic substrates. However, to

date, application of these measurement platforms for functional studies on lipid membranes has remained largely limited beyond protein binding studies. Nevertheless, there is excellent potential for utilizing nanoplasmonic sensors to study membrane-related processes occurring at interfaces, in part due to the highly surface-sensitive measurement techniques that offer superior analytical capabilities over competitor technologies. Towards this goal, our group and others have recently conducted several studies that show the potential of nanoplasmonic sensors for lipid membrane studies in a variety of contexts as described in the rest of this section.

4.2. Probing vesicle deformation

As explained above, most lipid membrane-related studies have entailed fabricating silicon oxide-coated nanoplasmonic substrates in order to form supported lipid bilayers. While this approach is perfectly suited to form high-quality lipid membranes for biosensing applications, there are also additional possibilities to utilize the materials science of nanoplasmonic sensors to fabricate other types of lipid membrane platforms. Goh *et al.* investigated the adsorption of lipid vesicles onto noninteracting, bare gold nanodisks on a glass substrate as well as equivalent platforms coated with conformal layers of silicon oxide or titanium oxide.³¹² While silicon oxide promotes vesicle adsorption and rupture, titanium oxide and gold typically promote vesicle adsorption without subsequent rupture, instead leading to the formation of an adsorbed, intact vesicle layer.³²² Taking advantage of these possibilities, it was demonstrated that the materials-selective chemistry of lipid vesicle adsorption onto solid supports can be exploited to form either supported lipid bilayers or adsorbed vesicles on the nanoplasmonic substrates. Interestingly, a heterogeneous lipid membrane architecture could be achieved on the bare nanodisk substrate. It was comprised of single lipid vesicles on top of the gold nanodisks, which were surrounded by a supported lipid bilayer on the glass substrate. This unique architecture was confirmed by adding to a membrane-active AH peptide to induce vesicle rupture, whereas a negligible response was observed when the same peptide was added to a supported lipid bilayer. Another important development stemming from this work was the first detailed analysis of the rupture kinetics by analyzing the time derivative of the LSPR peak shift, which provided deeper insight into the two-stage process observed for bilayer formation as well as opened the door to quantitative studies of vesicle adsorption. The study also provided a useful comparison to see how the measurement responses, namely the $\Delta\lambda_{\text{max}}$ shifts associated with vesicle adsorption and bilayer formation, depended on the presence of a dielectric coating as well as the material composition of this coating. A clear dependence on the material properties of the coating were observed with respect to the LSPR measurement responses and correlated well with the bulk refractive index sensitivities of the different sensing platforms ranging from around 80–200 nm per RIU.

Following this line, Jackman *et al.* investigated the adsorption of lipid vesicles onto a titanium oxide-coated gold nanodisk array and the nanodisks had similar dimensions in this case.¹⁸³ One key motivation of this work was to study the role of

vesicle shape deformation in the adsorption process because LSPR is more highly surface-sensitive than other measurement techniques which are commonly used to study vesicle adsorption (*e.g.*, QCM-D and SPR). The effects of vesicle size and lipid concentration on the adsorption kinetics were experimentally scrutinized. Importantly, an extended theoretical treatment describing how vesicle adsorption is expected to affect the LSPR signal was also developed in order to derive scaling laws. Comparison of the observed experimental results with the theoretical predictions yielded new information about the vesicle adsorption process, including evidence for a multiple-stage process whereby the extent of vesicle deformation increased with greater vesicle size and at higher concentrations. Overall, the study demonstrated the utility of LSPR biosensing measurements for soft matter adsorption studies at solid–liquid interfaces. Oh *et al.* further extended the measurement capabilities of LSPR biosensing to study vesicle deformation on titanium oxide-coated gold nanodisk arrays in the context of temperature-dependent membrane phase transformations.³¹³ While LSPR biosensing at solid–liquid interfaces has been sparsely applied to temperature-dependent studies,³²³ there is a particularly useful benefit for adsorption studies being that the LSPR signal exhibits high temperature stability and is only sensitive to the well-established, temperature-dependent change in the refractive index of the solution. Depending on the particular lipid composition and corresponding membrane phase state at different temperatures, it was discovered that increasing temperature

can promote, hinder, or have negligible effect on the deformation of adsorbed vesicles. Another important contribution of this work was that general equations were developed in order to explain the effect of vesicle deformation on the LSPR signal.

While measuring vesicle deformation on one substrate is advantageous, another possibility of these LSPR measurement capabilities emerges to compare the extent of vesicle deformation on multiple substrates. Indeed, one long-standing question in vesicle adsorption studies is clarifying why adsorbed vesicles rupture on silicon oxide, but remain intact on titanium oxide when theory predicts the opposite.³²⁴ One experimental challenge has been directly measuring the extent of deformation of adsorbed vesicles in the course of the vesicle-to-bilayer structural transformation. To address this problem, Jackman *et al.* reported a nanoplasmonic ruler method in order to compare the deformation of adsorbed vesicles on silicon oxide-*versus* titanium oxide-coated gold nanodisk arrays³¹⁴ (Fig. 9). In order to compare the LSPR signals on the two substrates, the surface sensitivity of each sensor substrate was carefully considered through experimental measurements of the bulk and local refractive index sensitivities as well as 3D finite-difference time-domain (FDTD) simulations. Based on this approach, a normalization procedure was established to directly compare measurement responses across different sensing surfaces. It should be stressed that the fundamental nanodisk geometry was identical in each case and only the dielectric coating was varied. Vesicle adsorption experiments were conducted using a

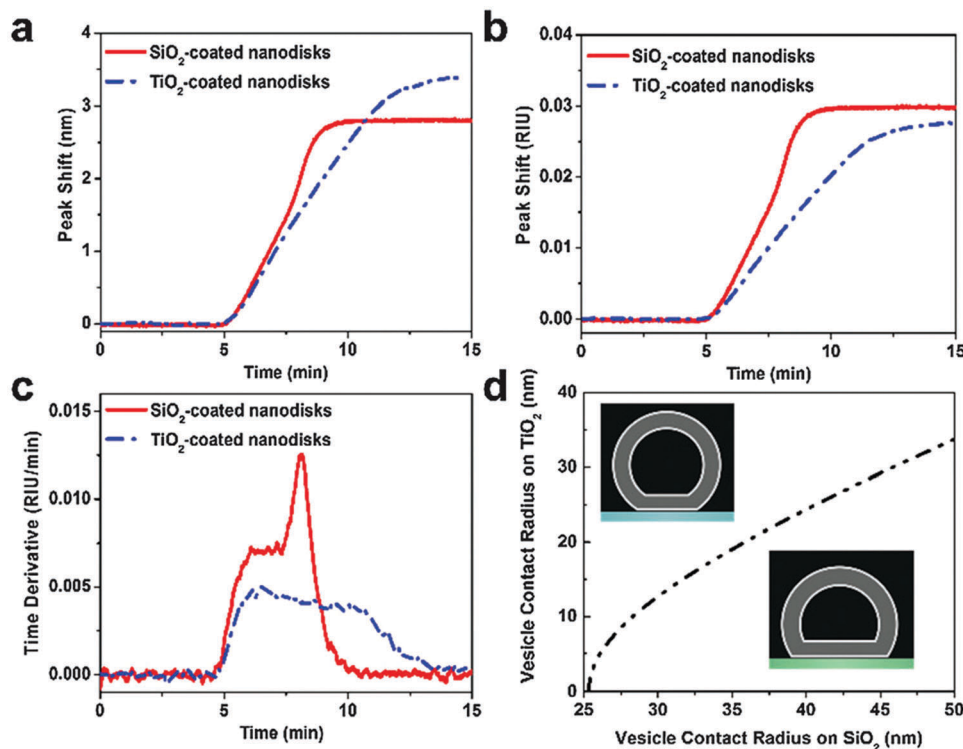


Fig. 9 Nanoplasmonic ruler to measure lipid vesicle deformation. (a) Comparison of LSPR peak shifts as a function of time upon 0.1 mg mL⁻¹ POPC lipid vesicle addition. (b) Normalized LSPR peak shifts from panel a according to the experimentally determined bulk RI sensitivity of each substrate. (c) Time derivative of the normalized peak shift from panel b. (d) Calculated variation in contact radius of adsorbed vesicles on silicon oxide *versus* titanium oxide. Reproduced (in part) from ref. 314 with permission of The Royal Society of Chemistry.

single batch of lipid vesicles on the two substrates and the resulting adsorption kinetics were compared. Because the vesicle adsorption process was identically conducted on both substrates, the diffusion flux was equivalent in both cases and any differences in the LSPR signal during the initial vesicle adsorption stage before rupture commenced were attributed to varying degrees of vesicle deformation. These measurements identified that adsorbed vesicles on silicon oxide undergo greater deformation than adsorbed vesicles on titanium oxide on account of a greater rate of change in the signal response during this initial stage, offering the first direct experimental evidence to support membrane tension-based models of vesicle rupture. A key element of the sensor design was that the decay length, l_d , was shorter than the length scale of the adsorbed lipid vesicles, thereby rendering the measurement platform sensitive to different extents of shape deformation.

Having established methodologies to utilize LSPR biosensing for the purpose of observing vesicle deformation on solid supports, more sensitive experimental parameters such as the type of divalent cation have also been investigated in the context of tracking the kinetics of vesicle adsorption and rupture. Dacic *et al.* explored the adsorption of zwitterionic lipid vesicles onto silicon oxide and titanium oxide-coated gold nanodisk surfaces in the absence and presence of magnesium, calcium, and strontium ions.³¹⁵ For this case, QCM-D experiments were performed alongside LSPR experiments in order to extract information about the viscoelastic properties and effective thickness of the adsorbed vesicle layers. While the QCM-D data provided strong initial evidence suggesting that divalent cations have significant effects on the deformation of adsorbed vesicles, it was challenging to quantitatively characterize the relative extent of vesicle deformation. In contrast, quantitative interpretation of LSPR data can directly infer the relative extent of vesicle deformation.^{183,313} The results revealed that divalent cations increase the deformation of adsorbed vesicles on silicon oxide and titanium oxide but the effects on both vesicle deformation and rupture were modest and subtle. Nevertheless, the high surface-sensitivity of the LSPR measurements provided the first direct experimental evidence that calcium ions induce the greatest vesicle deformation, and enabled a quantitative comparison of the relative deformation of adsorbed vesicles in the presence of different divalent cations (calcium > magnesium > strontium in terms of enhanced vesicle deformation). In separate work, the quantitative profiling of nanoscale vesicle deformation was validated by comparing LSPR measurements for fluid-phase, soft vesicles *versus* gel-phase, rigid vesicles, demonstrating the utility of this measurement approach for studying soft matter adsorbates.³¹⁶ Under varying osmotic pressure conditions, it was observed the fluid-phase lipid vesicles exhibited different extents of deformation based on the measurement responses, whereas gel-phase lipid vesicles had identical adsorption kinetics in different osmotic pressure conditions. In addition, LSPR measurements are capable of detecting more subtle (~ 1 nm) variations in the distance between supported lipid bilayers and underlying silica oxide surfaces.³²¹ Such variations were probed by varying the membrane composition of supported

lipid bilayers *vis-à-vis* electrostatic surface charge, thereby modulating the bilayer–substrate interaction strength (degree of electrostatic attraction/repulsion) and corresponding separation distance. With decreasing separation distance between the bilayer and sensor surface, the peak shift increased because the phospholipids in the bilayer membrane were, on average, in a region of higher field intensity, demonstrating the high surface sensitivity of the LSPR measurement approach on even such short length scales. Collectively, all the presented findings demonstrate that both nanodisks and short-range ordered nanohole arrays are suitable for detection of structural transformations associated with vesicle adsorption, deformation, and rupture on dielectric-coated plasmonic substrates.

Most recently, the combination of LSPR with a conventional QCM-D instrument was demonstrated in order to track vesicle adsorption and rupture on titanium oxide-coated gold nanodisks.³¹⁷ In particular, the difference in penetration depths between the two techniques enabled structural transformations associated with vesicle rupture to be tracked with high temporal and spatial resolution. The platform was also utilized to study the size dependency of intact vesicle adsorption on titanium oxide and found that the maximum vesicle–surface contact area occurs for intermediate-size vesicles on account of a competition between vesicle deformation and steric hindrance during the adsorption process.³¹⁸ In another related application, the interaction of ionic liquids with adsorbed lipid vesicles was probed using a similar measurement approach (dielectric-coated gold nanodisk array) and revealed insights into vesicle deformation and membrane destabilization based on the same measurement principles.³²⁰ In a separate contribution with regard to combining nanoplasmonic platforms with other techniques to characterize the process of lipid membrane fabrication, Chen *et al.* characterized vesicle–surface interactions by using LSPR combined with SALDI-MS.³¹⁹ Instead of using nanodisks or nanoholes, they deposited gold nanoparticles followed by the formation of an ultrathin silicate coating on the nanoparticles *via* the calcination of sodium silicate and monitored in real-time both intact vesicle adsorption as well as SLB formation. While surface functionalization is an important part of nanoplasmonic sensing strategies, especially in the context of detection applications, the studies in this section highlight the wide range of research opportunities that are available in the biointerfacial sciences and do not necessarily require classical surface functionalization strategies. Rather, a key design concept behind the aforementioned studies in this section is the capability to coat nanoplasmonic transducers with thin dielectric layers in order to study biomacromolecular interaction processes on different solid supports. Hence, there is a wide range of surface functionalization strategies that can be employed depending on the application.

5. Membrane protein studies

Taking advantage of emerging abilities to fabricate supported lipid membranes on plasmonic nanosensors, one of the most promising areas has been the integration of lipid membrane

platforms with membrane proteins for functional studies, as summarized in Table 4. Since membrane-associated proteins regulate key functions in living cells such as signaling and transport, an in-depth understanding of a variety of interactions between proteins and the cell membrane is a high priority. As described above, one of the earliest examples was demonstrated by Dahlin *et al.* which investigated the interaction between biotinylated lipids and Neutravidin. Specifically, they functionalized the SLB with 1% biotinylated lipids and subsequent addition of $10 \mu\text{g mL}^{-1}$ Neutravidin resulted in a shift of $\sim 1 \text{ nm}$, with a signal-to-noise ratio of 500. Furthermore, by combining the nanoplasmonic sensing platform with QCM-D measurements, the setup enabled determination of the effective thickness of the protein film as well as the optical mass of bound protein.^{310,325}

Nanohole arrays and other nanoplasmonic sensing platforms have also been utilized extensively by the Oh group in order to study membrane-protein interactions.^{133,206,237,326–329} In one of their earlier works, they demonstrated the use of surface plasmon enhanced light transmission (based on the EOT effect) through periodic nanohole arrays in order to monitor the real-time binding of streptavidin to biotinylated lipids in supported lipid bilayers.³²⁷ The addition of 300 nM streptavidin resulted in a shift of 4 nm as recorded at the transmission dip. Interestingly, when recording the change in transmitted intensity at a fixed wavelength, the periodicity of the nanoholes was shown to affect the measurement response associated with streptavidin binding kinetics and this was attributed to the slope of the transmission resonance peak at the chosen wavelength. In the same report, the authors also introduced a free-standing lipid membrane nanohole array sensor as a more advanced biomimetic platform as both sides of the lipid bilayer can be accessed. Indeed, the configuration is designed so that the lipid membrane spans over suspended nanopores that are exposed to microfluidic reservoirs on both the top and bottom sides. From a design perspective, important advantages of this measurement setup include the ability for proteins to be introduced from both sides as well as the ability to insert transmembrane proteins without compromising their functionality. In continuing work, the team also showed that the insertion of the transmembrane protein α -hemolysin (α -HL) in pore-spanning lipid membranes resulted in a redshift of the minima in the transmission spectrum³²⁶ (Fig. 10a and b). A further redshift was observed when biotinylated anti- α -HL was added implying the occurrence of a binding event. Besides using synthetic lipid bilayers, the Oh group also demonstrated the use of natural cell membranes in recessed micro- and nanowells in order to study membrane-protein interactions.³²⁸ They developed myelin and neuronal lipid raft microarrays and used the platform for detection of ganglioside GM1 *via* cholera toxin (CTX) binding and antibody recognition of cell-specific membrane antigens. They also employed nanohole SPR in order to measure the association and dissociation rate constants of natural auto-antibodies O1 and O4 binding to their lipid antigens.³²⁹ All of these works related to the determination of antibody binding kinetics and affinities motivated the development of a high-throughput sensing module. This was developed by Lee *et al.* through the utilization of large-area ($\sim \text{cm}^2$) metallic nanohole

arrays as nanohole SPR sensing substrates integrated with 50 parallel microfluidic channels.²³⁷ The ability to quantify a wide range of biomolecular interactions was demonstrated by simultaneously measuring the binding of cholera toxin b sub-unit (CTX-b) to ganglioside GM1 receptors under varying conditions such as different CTX-b concentrations. Similar capabilities have also been demonstrated for LSPR measurements whereby the formation of GM1-containing supported lipid bilayers on silicon oxide-coated nanodisk arrays, which were prepared by hole-mask colloidal lithography followed by sol-gel spin-coating of the oxide layer, enabled quantitative measurements of the binding affinity of CTX-b to membrane-embedded GM1 receptors.³³⁰

Another approach to elucidate membrane-protein interactions was developed by Groves and co-workers who utilized membrane-coated silver nanocubes^{331,332} (Fig. 10c–e). The choice of the nanocube architecture was important because its edges and corners show particularly strong electromagnetic field intensities. In their first demonstration, the silver nanocubes were immobilized onto a glass substrate and modified with an alkanethiol self-assembled monolayer (SAM).³³¹ Even after SAM coating, the nanocubes exhibited a bulk refractive index sensitivity around 165 nm per RIU, which is comparable to bare gold nanodisks described above in the preceding section. This scheme allowed phospholipid bilayers to form over the bare glass parts of the substrate and phospholipid monolayers over the functionalized nanocubes. Molecular binding/unbinding events were recorded as shifts in the LSPR peak (λ_{max}) of the absorbance spectra originating from the silver nanocubes. They showed that non-specific binding of BSA yielded a minute shift of 0.03 nm, which indicated that the nanocubes are fully coated with lipid membrane for a stable sensing platform that prevents non-specific adsorption, as expected for lipid bilayer coatings.²⁶¹ Then, by utilizing DOGS-NTA-Ni lipids which bind to a hexahistidine tag at the C-terminus of yellow fluorescent protein (YFP), they demonstrated real-time monitoring of the unbinding of YFP from a DOGS-NTA-Ni functionalized membrane based on the LSPR peak shift. Interestingly, the LSPR peak position in these experiments was fitted by a polynomial function, which enabled sensor detection down to a 0.02 nm resolution, and the surface functionalization strategy enabled a very low noise level (high signal-to-noise ratio) with minimal nonspecific binding events.³³³ In another conceptually related work, they employed silica-coated silver nanocubes in the solution phase.³³² The nanocubes were simply added to a vesicle suspension in order to promote supported lipid bilayer formation on the nanocube surface. This subsequently allowed the binding of proteins to be detected *via* LSPR peak shifts acquired through a standard laboratory spectrophotometer. This platform was developed into an assay to determine how membrane composition affects the lipid binding of Ste5, a prototypical mitogen-activated protein kinase (MAPK). This was achieved by measuring temporal shifts in the LSPR peak position as well as its dependence on Ste5 concentration, for membranes with and without 1- α -phosphatidylinositol-4,5-bisphosphate (PI(4,5)P₂). They obtained equilibrium dissociation constants (K_D) of $0.49 \pm 0.33 \mu\text{M}$ and

Table 4 Highlighted works that involve surface-based nanoplasmonic sensors for studying membrane–protein interactions

Membrane–protein interaction	Plasmonic transducer platform	Information obtained	Sensing principle	Signal readout	Ref.
Biotinylated lipids–Neutravidin	Nanohole in Au film on silicon oxide	Interaction kinetics (real-time kinetics of protein binding to lipid bilayer)	EOT	Wavelength shift of the extinction maxima	306
Biotinylated lipids–Neutravidin	Nanohole in Au film on silicon oxide	Adsorbate properties and interaction kinetics (real-time kinetics of protein binding to lipid bilayer, effective thickness of protein film, optical mass of bound protein)	EOT	Wavelength shift of the extinction maxima	310
Biotinylated lipids–Neutravidin	Silicon oxide-coated nanohole in Au film	Adsorbate properties and interaction kinetics (real-time kinetics of protein binding to lipid bilayer, effective thickness of protein film, optical mass of bound protein)	EOT	Wavelength shift of the extinction maxima	307
Biotinylated lipids–SAPE	Embedded Au nanodisk in optical epoxy and SiO ₂ coating	Adsorbate properties and interaction kinetics (real-time kinetics of protein binding to lipid bilayer, effective thickness of protein film, optical mass of bound protein)	LSPR	Wavelength shift of the extinction maxima	133
Biotinylated lipids–SAPE	Nanohole in Ag film on Si	Adsorbate properties and interaction kinetics (real-time kinetics of protein binding to lipid bilayer, effective thickness of protein film, optical mass of bound protein)	EOT	Wavelength shift of the transmission minima	198
α -HL incorporated lipid–anti- α -HL	Nanopore in free-standing silica-coated Au on Si ₃ N ₄ film	Adsorbate properties and interaction kinetics (real-time kinetics of protein binding to lipid bilayer, effective thickness of protein film, optical mass of bound protein)	EOT	Wavelength shift of the transmission minima	326
GM1 incorporated lipid–CTX-b	Nanohole in Ag film on glass	Adsorbate properties and interaction kinetics (real-time kinetics of protein binding to lipid bilayer, effective thickness of protein film, optical mass of bound protein)	EOT	Wavelength shift of the transmission maxima	237
GM1 incorporated lipid–CTX-b	Silicon oxide-coated nanodisk on glass	Adsorbate properties and interaction kinetics (real-time kinetics of protein binding to lipid bilayer)	LSPR	Wavelength shift of the extinction maxima	330
Natural cell membranes, CTX binding to GM1 on lipid rafts	Nanohole in Au film on Si	Adsorbate properties and interaction kinetics (real-time kinetics of protein binding to lipid bilayer, effective thickness of protein film, optical mass of bound protein)	EOT	Wavelength shift of the transmission minima	328
O1 and O4 IgMs binding to eggPC (2% GalC or 2% Sulf) YFP unbinding from DOGS-NTA-Ni lipid membrane	Nanohole in Au film on glass Ag nanocube on glass	Interaction kinetics (real-time kinetics of protein binding to lipid bilayer) Interaction kinetics (real-time kinetics of protein unbinding from lipid bilayer)	EOT LSPR	Wavelength shift of the transmission minima Wavelength shift of the absorbance maxima	329 331

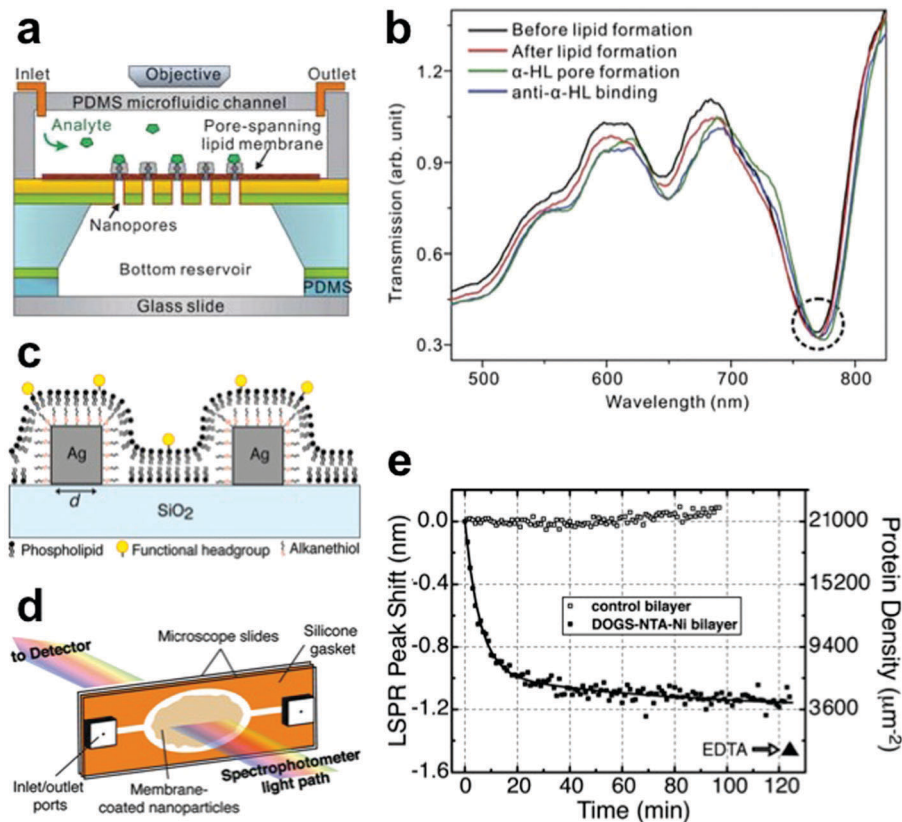


Fig. 10 (a) A free-standing nanopore array chip supporting pore-spanning lipid membrane integrated with microfluidic channels. (b) Transmission spectra change before (black line) and after the formation of pore spanning lipid membrane (red line), after the formation of α -HL pore on the lipid membrane (green line), and after the binding of anti- α -HL (blue line). Reproduced (in part) from ref. 326 with permission of The Royal Society of Chemistry. (c) Schematic of nanocubes with edge length d embedded in the membrane substrate. A supported bilayer exists over glass, while a hybrid phospholipid/alkanethiol bilayer is over the silver nanocubes. (d) The silver nanocube on glass sensing platform is integrated with a flow device. The device is placed in the light path of a spectrophotometer and allows easy exchange of solution surrounding the substrate. (e) YFP unbinding monitored by LSPR peak shift. Observed shift in λ_{\max} position compared with $t = 0$ min for a nanocube-embedded bilayer with (dark squares) or without (open squares) DOGS-NTA-Ni lipids. Reprinted (adapted) with permission from ref. 331. Copyright 2009 American Chemical Society.

$1.6 \pm 0.45 \mu\text{M}$ for PI(4,5) P_2 -containing and PI(4,5) P_2 -free bilayers, respectively. A similar approach was exploited by Castellana *et al.* in order to study the capture of lipophilic drug Amphotericin B and lipopeptide myristoyl-Lys-Arg-Thr-Leu-Arg by lipid membranes tethered on the surface of gold nanorods.³³⁴ In this case, the longitudinal LSPR peak was used for sensing purposes on account of its particularly high sensitivity and analyte binding caused a redshift, as confirmed by mass spectrometry measurements. Messersmith *et al.* also used thiol-anchored lipid-coated spherical gold nanoparticles (AuNPs) to study protein binding *via* changes in multiple features of the LSPR spectral signature.¹⁵⁷ The authors added oleate, phosphatidylcholine (PC) as well as alkanethiols propanethiol (PT) and decanethiol (DT) to citrate-capped gold nanoparticles in order to form a hybrid membrane surrounding the nanoparticles. When C-reactive protein (CRP) was added, instead of just observing LSPR peak shifts, they observed changes in three characteristic parameters of the LSPR signal, namely the FWHM, the resonant wavelength and the optical density, allowing the binding of CRP to the PC membrane to be quantified in a more detailed manner. As a result, they could temporally

distinguish the CRP-membrane binding event from the CRP-induced membrane rearrangement event. This distinction would be beneficial in terms of gaining insights into the kinetics of conformational changes associated with membrane-protein interactions, including towards more applied research topics. Another important point concerns the nanoparticle shape. In the study, the SAM-coated spherical gold nanoparticles had a bulk refractive index sensitivity around 38 nm per RIU. While this detection sensitivity was sufficient to achieve the measurement goals, it is about 5-times lower than the sensitivities reported for SAM-coated silver nanocubes described in ref. 331, highlighting the connection between nanoparticle structure and sensing possibilities.

6. Exosomes and viruses

Table 5 presents an overview of nanoplasmonic sensor studies for virus and exosome detection applications, as well as for

Table 5 Highlighted works that involve analysis of virus or virus-like particles or exosomes via surface-based nanoplasmonic sensors. n.a. means not applicable

Virus/virus-like particles or exosome	Bio-recognition elements	Plasmonic transducer platform	Information obtained	Sensing principle	Signal readout	Ref.
Vesicular stomatitis, Ebola & vaccinia virus	8G5, M-DA01-A5 & A33L antibodies	Nanopore in free-standing Au on Ti & nitride film (periodic)	Binding avidity (end-point virus detection)	EOT	Wavelength shift of the transmission maxima	337
Virus-like streptavidin coated beads	Biotinylated thiol	Nanopore in free-standing Au on nitride film (periodic)	Interaction kinetics and binding avidity (real-time detection kinetics, concentration dependency)	EOT	Wavelength shift of the transmission maxima	338
Multiple HIV subtypes	Anti-gp120 antibody	Au nanoparticle on polystyrene	Binding avidity (end-point virus detection)	LSPR	Wavelength shift of the extinction maxima	339
HIV-1 virus-like particles	Anti-gp120 monoclonal antibody fragments	Au nanodots on ITO	Binding avidity (end-point virus detection, concentration dependency)	LSPR	Wavelength shift of the absorbance maxima	340
Avian influenza (AI) virus	Genetically engineered GBP-fusion protein	Au-capped silica nanoparticles on gold on glass	Binding avidity (end-point virus detection, concentration dependency)	LSPR	Wavelength shift of the absorbance maxima	341
Adenovirus particles	n.a.	Ag nanoislands on Ag/Cr film	Binding avidity (end-point virus detection, concentration dependency)	LSPR	Change in reflectance intensity	342
Dengue virus particle mimic	n.a.	Nanohole in Au film on glass (periodic)	Interaction kinetics, binding avidity and adsorbate properties (real-time detection kinetics, real-time rupture kinetics by AH peptide)	EOT	Wavelength shift of the transmission maxima	343
Norovirus particles	Glycosphingolipids	Silica-coated nanohole in Au film on Nb ₂ O ₅ on glass (non-periodic)	Interaction kinetics, binding avidity and adsorbate properties (real-time detection kinetics, positional information)	EOT	Wavelength shifts of the extinction maxima and minima	177
Ovarian cancer cell-derived exosomes	Antibodies for EpCAM, CD24, CD63	Nanohole in Au film on glass (periodic)	Interaction kinetics, binding avidity and adsorbate properties (real-time detection kinetics, concentration dependency & molecular profile)	EOT	Wavelength shift of the transmission maxima & changes in transmission intensity	344
Pancreatic cancer cell-derived exosomes	Antibodies for CD63 and CD9	Gold nanospheres and nanorods on glass	Interaction kinetics, binding avidity and adsorbate properties (real-time detection kinetics, concentration dependency & molecular profile)	LSPR	Change in extinction (scattering) intensity	345

biophysical investigations of virus binding and antiviral drug evaluation.

6.1. Detection applications

An emerging topic in nanoplasmonic biosensing applications is clinical diagnostics, with recent work demonstrating strong potential in the areas of virus and exosome detection. Virus infections call for rapid and sensitive diagnostic measures in order to treat the infection and prevent pandemic outbreaks.³³⁵ Likewise, exosomes are small particles secreted in large quantities by cancer cells and carry molecular information about tumors that can be obtained without the need for invasive biopsies.³³⁶ Conventionally, these kinds of biological specimens are profiled by molecular biology techniques such as an enzyme-linked immunosorbent assay (ELISA), which identifies antigens (*e.g.*, surface proteins) based on antibody binding, or the polymerase chain reaction (PCR), which detects nucleic acid fragments. However, such techniques require extensive sample preparation and processing, and may take several hours to perform. As an alternative, a label-free nanoplasmonic sensor is feasible because exosomes and many types of virus particles are in the range of 50 to 150 nm diameter which is suitable for detection.

Yanik *et al.* reported the first nanoplasmonic sensor to detect virus specimens in biological media.³³⁷ The sensor took advantage of the EOT effect, and was comprised of plasmonic gold nanoholes which were functionalized with antibodies that recognize surface proteins of specific virus types. From a fabrication perspective, another interesting aspect of the platform was that a lift-off free nanofabrication technique³⁴⁶ combining positive resist e-beam lithography and direct deposition of metal coatings was utilized, thereby enabling a narrow FWHM (15–20 nm) and high FOM (~ 40) for improved sensing performance. When a virus attaches to the antibody-functionalized surface, a wavelength shift in the transmission maximum was recorded enabling highly sensitive and rapid detection. The sensor platform was tested for three viruses, vesicular stomatitis virus, Ebola virus, and vaccinia virus, and yielded promising results. A three order-of-magnitude dynamic range over clinically relevant virus concentrations was identified, and the redshift at high virus concentrations was large enough (~ 100 nm) for visual detection. Interestingly, the spectral shifts recorded for viruses of different sizes was similar, suggesting that enhanced electromagnetic fields are highly confined to the surface and only virus material near the surface influences the sensor response. In biological media, virus detection at low concentrations was also demonstrated, and the recorded shift was three-fold higher than a reference sensor. From this proof-of-concept study, there are two areas of improvement that can be suggested. First, an incubation time of 90 min was needed due to the slow diffusion of viruses. In order to improve mass transport properties in this sensing format, Huang *et al.* introduced an actively controlled fluidic system with a suspended nanohole array.³³⁸ This design significantly improves mass transport of analytes because the flow passes through the nanoholes, yielding a one to two order-of-magnitude reduction

in measurement response time. Second, surface passivation of the nanohole array was achieved by protein blocking, although some nonspecific adsorption of serum proteins was detected. This issue could be addressed by employing an optimized surface passivation strategy, as discussed below.

Motivated by the potential of nanoplasmonic sensors for virus detection in point-of-care settings, Inci *et al.* demonstrated that the approach is suitable for identifying HIV subtypes in unprocessed blood samples obtained from patients.³³⁹ To establish this system, plasmonic gold nanoparticles were deposited on a substrate that was pre-coated with poly-L-lysine (PLL) at an optimal concentration (0.05 mg mL^{-1} PLL) to yield a high extinction coefficient that resulted in the highest recorded amount of gold nanoparticle binding to the PLL-coated surface. As a result, the deposited nanoparticles achieved a high surface coverage and were functionalized with Neutravidin before adding a biotinylated HIV-specific antibody, which recognizes the gp120 envelope protein on the HIV virus surface. When virus specimens in whole blood were incubated for 1 hour on the sensor surface, a statistically significant shift in the extinction maximum of the LSPR signal was measured, as compared to a control blood sample without virus. Depending on the HIV subtype, a limit of detection down to 98 ± 39 copies per mL was achieved. A repeatability parameter of between 56% and 90% was also obtained, which indicates that the sensor performance is accurate and reproducible.

Impressively, quantitative detection of HIV viral load in patient samples showed a correlation with real-time PCR measurements, with the added benefits of simpler instruments, minimal processing, and faster response.³⁴⁷ In another related report, Lee *et al.* demonstrated label-free LSPR detection of HIV-1 virus-like particles (VLPs) based on tracking the shift in the absorbance maximum.³⁴⁰ The signal arises from the binding of HIV-1 VLPs to gold nanodots (*i.e.*, the LSPR sensing component) functionalized with gp120 monoclonal antibody fragments, on indium tin oxide (ITO)-coated glass substrates. A detection limit of around 200 fg mL^{-1} was achieved with a dynamic range between 200 fg mL^{-1} to 125 pg mL^{-1} . The latter has a correlation coefficient of 0.990, proving the robustness of the LSPR platform to produce linear concentration-dependent responses over several orders of magnitude, even at very low concentration ranges. A similar label-free LSPR sensing format relying on antigen binding to immobilized antibodies on deposited gold nanostructures have likewise been earlier exploited for the detection of avian influenza (AI) virus.³⁴¹ In related work, Yu *et al.* have also demonstrated the high-sensitivity detection of adenovirus particles based on the locally amplified electromagnetic field afforded by randomly arranged silver nanoislands in a total internal reflection configuration.³⁴² Altogether, these studies illustrate the possibilities of nanoplasmonic sensors for virus detection.

Nanoplasmonic sensors have also demonstrated strong merit for label-free detection of exosomes. There have been at least four reports on the subject, including two studies^{2,348} involving conventional SPR systems based on total internal reflection and one study³⁴⁴ by Im *et al.* which employed an EOT-based periodic nanohole array (Fig. 11). Here, we focus our discussion on the latter study as there were several particularly

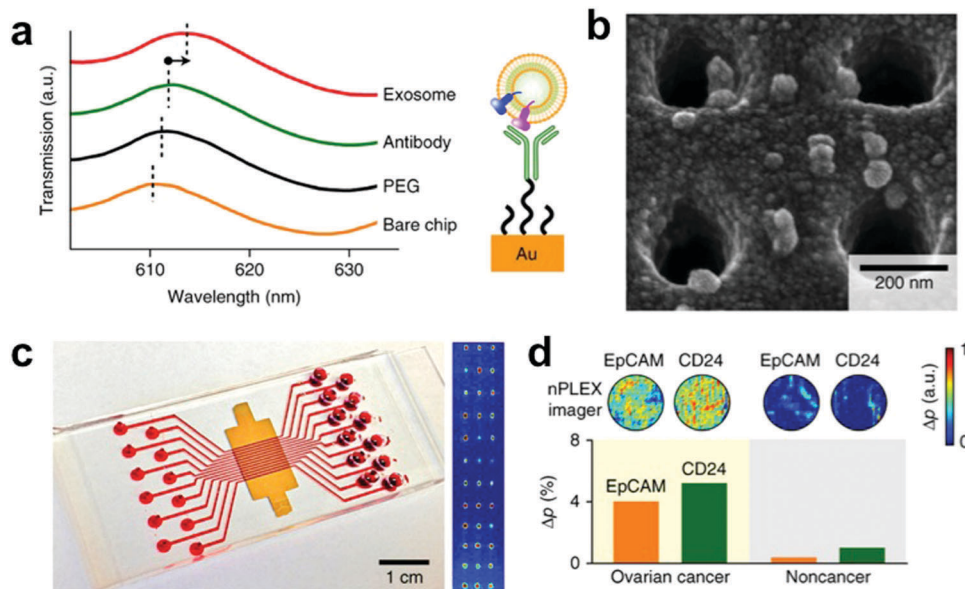


Fig. 11 (a) A representative schematic of changes in transmission spectra showing exosome detection with the nanoplasmonic exosome (nPLEX) sensor. The gold surface is pre-functionalized by a layer of polyethylene glycol (PEG), and antibody conjugation and specific exosome binding were monitored by transmission spectral shifts as measured by nPLEX. (b) SEM indicates specific exosome capture by functionalized nPLEX. (c) A photograph of nPLEX chip integrated with a multichannel microfluidic cell for independent and parallel analyses. (right) Transmission intensities of 12×3 nanohole arrays were measured simultaneously using the imaging setup. (d) Ascites-derived exosomes from ovarian cancer and noncancer patients were evaluated by the nPLEX sensor. Cancer exosomes were captured on EpCAM and CD24-specific sensor sites, which led to intensity changes in the transmitted light. Reprinted by permission from Macmillan Publishers Ltd: ref. 344, copyright 2014.

impressive components of the work with regards to nanoplasmonic sensor design. The transmission setup utilized a miniaturized, high-throughput system, based on measurement strategies previously established in ref. 236 and 349, for parallel detection of exosome attachment to various antibodies that identify specific proteins on the exosome surface. As the exosomes were measured to be around 100 nm diameter, the EOT sensing platform was designed to have nanoholes with 200 nm diameter and 200 nm height (within gold film on glass substrate) based on simulation studies that indicated the amplified electromagnetic field intensity in this particular design best overlapped the exosome size, which is line with discussion points raised in Section 2.3 about optimal l_d values. Furthermore, the platform's detection sensitivity was optimized by systematically adjusting the periodicity to be 450 nm between holes. Spectral shifts and intensity changes were proportional to the amount of target protein, and the entire array could be imaged simultaneously. The limit of detection was around 3000 exosomes, demonstrating two orders-of-magnitude improved sensitivity over ELISA while also requiring lower sample quantities. Importantly, exosome samples obtained from cancer patients and a control group could be screened in the multiplexed array and the levels of two exosome proteins were significantly higher in the cancer patient samples. Based on this finding, it was recommended that the two proteins need to be further investigated as potential biomarkers for ovarian cancer. While further testing is required to validate the clinical utility of the

n nanoplasmonic sensor system, the massively parallel capabilities lend strong potential to the refinement of these technologies for next-generation microarrays. Indeed, as recently reported, exosome capture onto antibody-functionalized glass slides followed by labeling with antibody-conjugated gold nanospheres and nanorods, enabled direct quantification of pancreatic tumor-derived exosomes from very small ($\sim 1 \mu\text{L}$) plasma samples.³⁴⁵ Taken together, the recent progress in virus and exosome detection platforms is evidence of how nanofabrication, sensor design, and clinical motivation can come together to achieve state-of-the-art advances for clinical diagnostics to detect nanoscale particulates as well as larger bacteria.³⁵⁰

6.2. Bioanalytical platforms

Most recently, there have been growing efforts to explore new applications of nanoplasmonic sensors for virus analysis beyond detection, using virus-like and virus particles as macromolecular models to investigate new analysis strategies for nanoplasmonic sensing. Together with the Oh group, we recently reported the development of a transmission mode EOT-based plasmonic nanohole sensor in order to selectively immobilize single lipid vesicles and virus-like particles in a periodic configuration that is suitable for molecular binding and membrane rupture analysis³⁴³ (Fig. 12a and b). In the work, a periodic gold nanohole array with suitable size dimensions to host virus-like particles was fabricated and coated with a passivating poly(ethylene glycol) spacing layer on the top surface between the nanoholes and on the nanohole

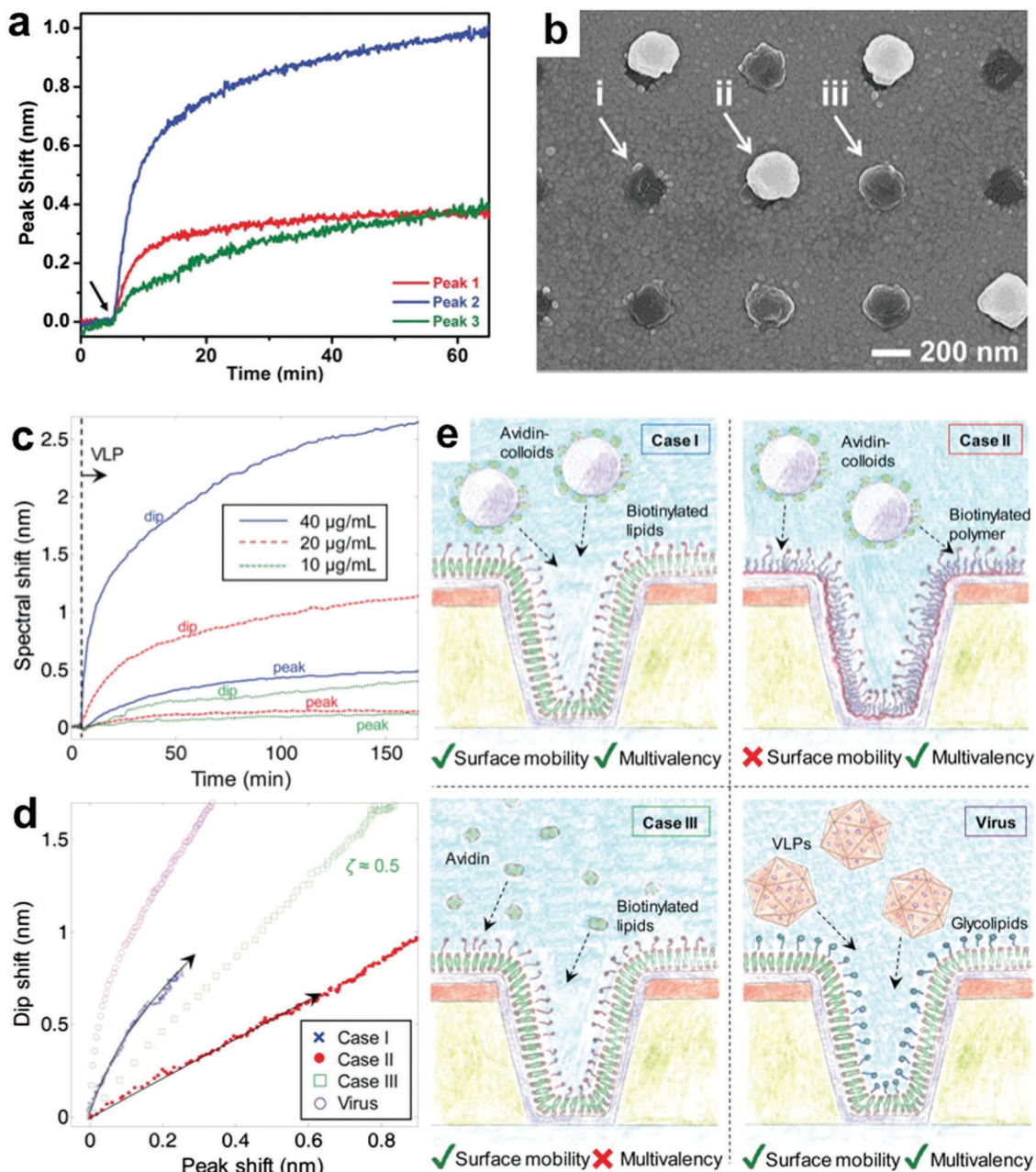


Fig. 12 (a and b) Selective adsorption of virus-like particles into functionalized nanoholes. Nanohole SPR experiments were performed on (a) mPEG-SH-functionalized nanohole arrays. Spectral shifts as a function of time were recorded for three transmission peaks. The baseline signal corresponds to aqueous buffer solution. Then, 0.3 mg mL^{-1} virus-like particles were added (denoted by arrow) and the particle rupture process was tracked. (b) SEM image obtained at $40\,000\times$ magnification demonstrate that single virus-like particles adsorbed into individual nanoholes on the mPEG-SH-functionalized nanohole array. Arrows indicate the three cases: (i) no particle in the nanohole; (ii) one particle partially inside the nanohole; and (iii) one particle predominately inside the nanohole. Aside from the nanohole positions, nonspecific adsorption of virus-like particles was not observed on the mPEG-SH-functionalized gold surface. Reprinted (adapted) with permission from ref. 343. Copyright 2016 Wiley-VCH. (c and d) VLP binding to nanowells and the influence from surface diffusivity and multivalency. (c) Kinetics (dip and peak) of different concentrations of virus capsids binding to a membrane with glycosphingolipids following the contour of silica coated nanowells. The VLPs are introduced by an injection and binding monitored with stagnant solution. (d) Scatter plots of peak and dip shifts for binding of avidin-coated particles, avidin and VLPs ($40 \mu\text{g mL}^{-1}$). (e) Illustrations of the measured interactions using silica-coated nanowells. Reproduced (in part) with permission from ref. 177 with permission from The Royal Society of Chemistry.

sidewalls, but not on the bottom surface of the nanoholes. As such, this passivation scheme enabled the passive and selective immobilization of cholesterol-enriched model virus

particles only inside the nanoholes. One key advantage of this approach is that it permits analysis of lipid vesicles and virus particles in isolation, bypassing potential measurement artifacts

arising from crowded populations where membrane–membrane fusion events can occur. At the same time, the nanoplasmonic sensing platform is label-free unlike other related single-particle approaches and does not require specific attachment chemistries for immobilizing vesicles or viruses on the surface. Due to the combination of these benefits, the single-particle approach proved advantageous for evaluating the performance of a membrane-active antiviral peptide that ruptures enveloped viruses.³⁵¹ When the peptide interacted with individual model virus particles, a clear rupture signature was detected based on a negative peak shift corresponding to the loss of lipid mass from the sensor surface. As previously mentioned, kinetic analysis in EOT-based measurements is challenging due to the complex spectral features and different transmission peaks and minima which correspond to the Bragg resonance orders at various interfaces of the nanohole geometry.²¹⁵ While changes in the bulk reflective index arising from exchange of graded glycerol–water mixtures were most sensitive at the gold–substrate interface, membrane rupture was most sensitively detected at the gold–water interface, offering empirical insight into how different features in the spectral signature can be utilized for measurement analysis.

Other improvements in measurement analysis for nanoplasmonic sensing have been reported by the Dahlin group which studied the binding of norovirus particles to glycosphingolipid receptors in lipid bilayer-coated nanoholes¹⁷⁷ (Fig. 12c and d). The approximately 100 nm diameter nanoholes were formed by mask-on-metal colloidal lithography²⁰⁰ in double-layer gold (30 nm thick) and niobia (Nb₂O₅; 200 nm thick) films. The nanohole array exhibited short-range ordering and was coated with a thin layer of silica in order to facilitate bilayer formation. Of note, it was remarked that the walls of the nanoholes were not vertical, but rather had an increasing degree of negative surface curvature towards the bottom of the hole, which likely aided formation of contiguous bilayers following the surface contour. Based on the spectral characteristics of the silica-coated plasmonic nanoholes in the study, an analytical method was developed in order to determine if analyte binding occurs on the top surface of the substrate and/or inside the nanoholes. Specifically, supported lipid bilayers on the top surface exhibited a planar geometry while the bilayer coating the nanohole walls possessed negative membrane curvature. Hence, selective binding to one region or the other would offer insight into membrane curvature preferences of macromolecules. The key sensing element behind this measurement capability is that the plasmonic nanowells have an asymmetric resonance with one peak and dip in the extinction spectrum. The peak is more sensitive to binding events on the top surface, whereas the dip is more sensitive to binding events inside the nanohole. The ratio of the peak shifts at the two spectral positions could be compared in order to determine the relative binding preference for different membrane curvatures. Using this platform, it was determined that norovirus particles prefer binding to negative membrane curvature, which was attributed to multivalent interactions between glycosphingolipid receptors and viral proteins. Overall, these two recent investigations highlight how geometrical features of nanoplasmonic

sensor design can be utilized for answering important biological questions, and the potential of surface functionalization strategies for conferring selective binding of target macromolecules on the basis of particle size or molecular interactions.

7. Nucleic acid studies

There is a long and rich history of detecting nucleic acids, including various types of deoxyribonucleic acid (DNA) and ribonucleic acid (RNA) molecules, with nanoplasmonic sensors, as extensively reviewed up to 2013 in ref. 352. Most measurement strategies revolve around hybridization of complementary nucleic acid strands, and key measurement considerations include response time, sensitivity, and the capability to detect subtle discrepancies such as single-base mismatches. While early nanoplasmonic sensing platforms involved colorimetric responses caused by hybridization-induced nanoparticle aggregation in bulk solution, Charrier *et al.* reported the two-dimensional aggregation of oligonucleotide-modified gold nanoparticles resulting from hybridization with complementary single-stranded DNA molecules, as detected by absorbance measurements.³⁵³ From the biointerfacial science perspective, an important design element of this study was that the nanoparticles were adsorbed onto a supported lipid bilayer-coated glass beads and hence retained lateral fluidity. Since then, most surface-based nanoplasmonic sensing platforms for nucleic acid detection have focused on measuring changes in the LSPR scattering intensity of individual, oligonucleotide-modified gold nanoparticles (generally >40 nm diameter).^{354–356} To achieve high sensitivity, dark field microscopy has often been employed to investigate the plasmonic responses of individual nanoparticles as well as more complex events like hybridization-induced dimerization of nanoparticles.^{357,358} At the same time, while dark field microscopy imaging is a promising technique to study nanoplasmonic phenomena at a very detailed level and has some practical merits,³⁵⁹ ensemble-averaged nanoplasmonic measurement capabilities represent a complementary approach with strong translational potential, and there have been recent advances on this front, including the design of nanostructures with high sensitivity and FOM,³⁶⁰ as well as emerging applications that will be discussed in the rest of this section. While the primary focus of the following application examples is aimed at LSPR measurements that are conducted in transmission mode, we wish to note that certain promising examples of nucleic acids studied from related measurement approaches (*e.g.*, LSPR scattering studies by dark field microscopy as well as surface-enhanced Raman spectroscopy or SERS) are also presented, including description of surface functionalization strategies that can be utilized in conjunction with other measurement strategies. Moreover, to the best of our knowledge, no EOT-based nanoplasmonic sensing studies have been conducted on nucleic acid systems. Hence, this section is designed to introduce the latest examples of nucleic acid investigations as well as motivate future research opportunities aimed at understanding biointerfacial science aspects of nucleic acids, including conformational changes and nucleic acid origami designs.

In the presence of monovalent cations, guanine-rich DNA strands can fold into a four-stranded G-quadruplex structure, and this transition from an unfolded to folded state is detectable on the basis of conformational changes in the DNA structure. Functionally, the folded structure can also bind to nucleolin, and high levels of this protein are associated with certain types of cancer; hence G-quadruplexes are also being considered as agents for cancer therapy. Motivated by these interesting features of G-quadruplexes, Cao *et al.* developed a U-shaped metamaterial sensing platform with a gold coating for transmission measurements, and the corresponding experiments indicated that there was a resonance dip corresponding to the electric resonance with a bulk refractive index sensitivity of 339 nm per RIU, which is comparable to conventional LSPR biosensors.³⁶⁰ A redshift was observed upon covalent immobilization of a thiolated guanine-rich DNA in water and another redshift occurred when the solvent was exchanged to a potassium-containing buffer solution. Based on control experiments along with SERS measurements and circular dichroism spectroscopy experiments, it was verified that part of the second redshift arose from potassium-triggered conformational changes in the DNA structure as G-quadruplex formation, resulting in a local electromagnetic enhancement as the molecular density of DNA strands became, on average, closer to the sensor surface. The platform was also able to measure the binding of a small peptide derived from nucleolin and the equilibrium disassociation constant of the peptide: G-quadruplex interaction was determined. Similar capabilities for probing conformational changes in G-quadruplexes have been achieved in the presence of different triggers (potassium ions or hydrogen peroxide) by dark field microscopy for guanine-rich DNA molecules immobilized *via* gold–thiol bonding onto individual, surface-adsorbed gold nanoparticles.³⁶¹ In this case, quadruplex formation again involved potassium-mediated compaction of the DNA structure, resulting in a redshift as explained in the previous example. Other recent SERS studies have investigated G-quadruplexes on nanoporous gold disks for small molecule sensing (*e.g.*, malachite green analyte;³⁶² in this study, 6-mercaptohexanol was added to the gold nanodisks after DNA binding in order to block nonspecific adsorption of small molecules in subsequent stages) as well as a breast cancer DNA biomarker.³⁶³ The importance of the G-quadruplex structure was supported by additional studies showing that single-stranded and double-stranded DNA strands have lower sensing performance.³⁶⁴

Recently, Rapisarda *et al.* conducted LSPR measurements in transmission mode to study the binding of complementary DNA strands, including those with a single base mismatch, to immobilized DNA strands on gold nanodisks that were attached to a glass substrate.³⁶⁵ The bulk refractive index sensitivity of the sensor chip was reported to be 72 nm per RIU and the corresponding decay length of the electromagnetic field intensity was estimated to be around 27 nm. $\Delta\lambda_{\max}$ shifts were recorded and corresponded to around 1 nm shifts for DNA immobilization and around 0.2–0.6 nm shifts for binding of complementary DNA strands. Importantly, the adsorption kinetics of the complementary DNA strand binding were analyzed in order to determine the hybridization rate constant. The

rate constant was three-times higher for the perfectly matched complementary DNA strand as compared to the strand with a single base mismatch. Hence, even in a measurement configuration with a relatively low measurement sensitivity, the results demonstrate that the adsorption kinetics of nucleic acid strands can be quantitatively monitored by the LSPR measurements.

From a biomedical perspective, there has also been interest in applying nanoplasmonic sensor technologies to study nucleic acid–drug interactions as well as detecting RNA biomarkers extracted from biological fluids (Fig. 13). In the first example, Frolov *et al.* investigated the interaction between an antibiotic called neomycin B and an RNA strand mimicking the ribosomal decoding site to which this particular antibiotic binds.³⁶⁶ The antibiotic was functionalized with polyethylene glycol (PEG)–thiol linkers, and the conjugate was then immobilized on gold island films on a glass substrate. The LSPR measurements were conducted in transmission mode and demonstrated selective binding of the target RNA molecule with a $\Delta\lambda_{\max}$ shift around 3 nm. The adsorption kinetics of different RNA strands binding to the sensing platform were evaluated in order to understand how RNA structure influences the binding kinetics and the antibiotic–RNA interaction was much stronger (as reflected in an order of magnitude higher binding constant) in the case of the bacterial RNA as compared to an analogous human RNA construct. This case is particularly interesting because the recognition element on the sensor surface was a small-molecule antibiotic and, by utilizing an appropriate surface functionalization strategy, it was possible to achieve selective and quantitative detection of the target RNA molecules, including binding affinity information. In another series of studies, Joshi *et al.* developed an LSPR sensing platform to detect microRNAs (miRs)—a diagnostic and prognostic disease marker—to detect subfemtomolar concentrations of miRs in human plasma from cancer patients.^{367,368} The LSPR measurements were conducted in transmission mode. The platform was based on thiolated DNA probe molecules (incubated in a 1 : 1 molar ratio with thiolated PEG molecules to passivate the sensor surface) that were attached to anisotropically shaped gold nanoprisms on a glass substrate. With increasing edge length of the nanoprisms, the limit of miR-10b detection in human plasma improved from 47.5 to 0.083 fM and this improvement was attributed to the increase in sensing volume. Importantly, the sensing platform could precisely quantify miR concentrations without requiring an extraction step and distinguish between patients with certain diseases and normal controls. Hence, there are a wide range of nucleic acid studies that demonstrate the broad potential of nanoplasmonic sensors for the biointerfacial sciences, including nucleic acid conformation, strand hybridization, nucleic acid–drug interactions, and clinically relevant nucleic acid detection applications.

The aforementioned studies reported in this section largely focus on ensemble-averaged LSPR measurements in transmission mode and hence embody one of the core focuses of this review. At the same time, several recent and exciting nanoplasmonic studies have been reported based on dark field microscopy experiments on individual nanoparticles (hence,

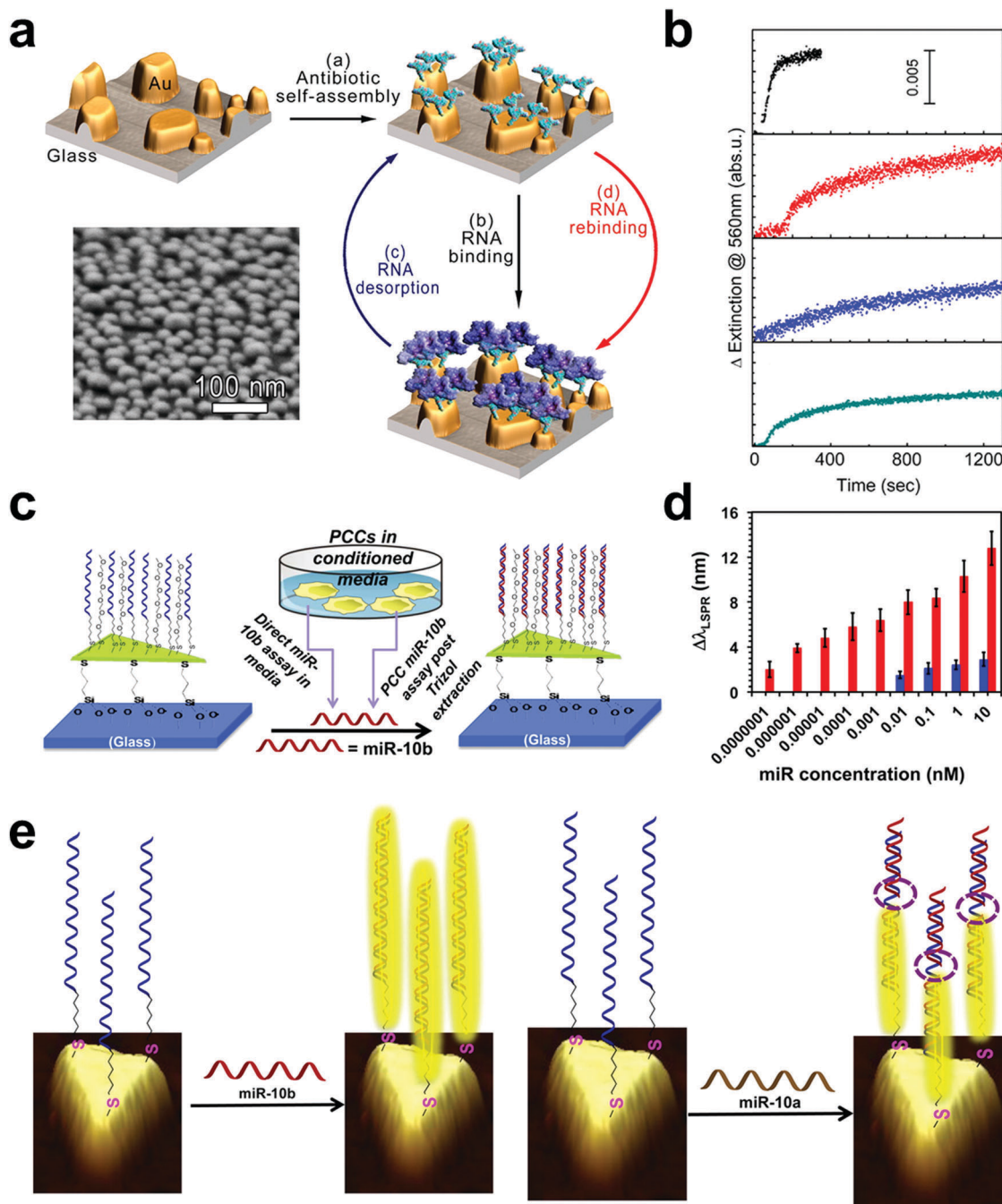


Fig. 13 (a) Schematic illustration of antibiotic–RNA binding detection scheme. Part a: self-assembly of antibiotic monolayer on gold island transducers; part b: RNA recognition; part c: RNA desorption; part d: RNA rebinding. Inset shows a tilted SEM micrograph of a 5 nm (nominal thickness) gold island transducer. (b) Representative LSPR binding curves for 1 μM RNA binding to antibiotic-functionalized gold transducers. Kinetic data were obtained by measuring the change in the extinction intensity at a constant wavelength of 560 nm in a micro flow cell. The data correspond to bacterial 16SA-site RNA (black), mutant bacterial site A-mod RNA (red), G-site RNA (blue), and *H. sapiens* 18S RNA (gray). Reprinted (adapted) with permission from ref. 366. Copyright 2013 American Chemical Society. (c) Schematic illustration of the fabrication of mixed -S-PEG6:-SC6-ssDNA-functionalized gold nanoprisms for LSPR detection of miR-10b RNA from different biological environments. (d) Comparison of concentration-dependent LSPR responses for detection of miR-10b (red) and miR-10a (blue) RNA. (e) Schematic representation illustrates electron-transport through duplex DNA in LSPR-based sensor which was fabricated with -SC6-ssDNA-10b:-S-PEG6 in hybridization with miR-10b and miR-10a RNA. Reprinted (adapted) with permission from ref. 368. Copyright 2015 American Chemical Society.

measuring changes in LSPR scattering intensity) and the scope of these studies deserves attention with respect to the biointerfacial sciences, including but not limited to detailed studies on

the thermodynamics of G-quadruplex folding.³⁶⁹ Indeed, the progress represented in these studies is a harbinger of what is possible for the nanoplasmonic sensor field as a whole and the

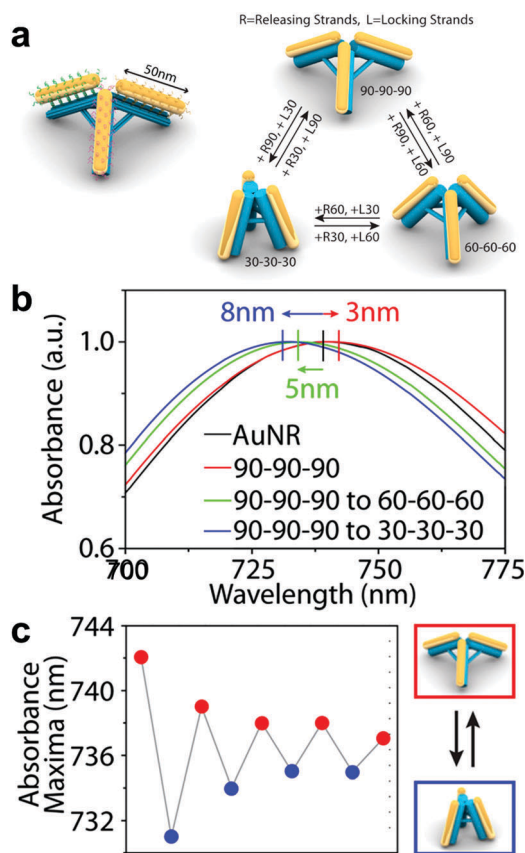


Fig. 14 (a) Schematic illustration of the reconfigurable DNA origami tripod with gold nanorods. Sets of releasing strands (R) and locking strands (L) are employed stepwise to change the angle between the DNA arms. (b) Absorbance spectra of free-DNA-conjugated AuNR (black line), AuNR-assembled 90–90–90 tripod (red line), and 30–30–30 (blue line) and 60–60–60 (green line) tripods converted from the 90–90–90 tripod with an absorbance peak shift in comparison to DNA-conjugated AuNR (black line). (c) Absorbance maxima shifts showing reconfiguration cycling between the 90–90–90 and the 30–30–30 AuNR-tripods. Reprinted (adapted) with permission from ref. 370. Copyright 2017 American Chemical Society.

feasibility and merits of performing similar types of experiments with ensemble-averaged nanoplasmonic sensor techniques based on the LSPR and EOT phenomena should be considered. One of the most interesting recent examples comes from the field of DNA origami, in which Zhan *et al.* designed a 3D reconfigurable DNA tripod nanostructure that exhibited reversible conformational changes based on the inter-rod angle³⁷⁰ (Fig. 14). A gold nanorod was attached to each leg of the tripod and conformational changes in DNA structure induced a shift in the plasmonic properties on account of the relative spatial proximity of the gold nanorods to one another and concomitant effects on near-field coupling. In addition to dark field microscopy experiments, ensemble-averaged measurements on the DNA nanostructures in bulk solution were also carried out by UV-vis spectroscopy and indicated that the conformational changes induce a $\Delta\lambda_{\max}$ shift of up to 8 nm.

From a diagnostic perspective, using gold nanoparticles functionalized with peptide nucleic acid probes, Nguyen *et al.*

demonstrated LSPR detection of circulating tumor DNA (ctDNA)—derived from tumors or circulating tumor cells—as a noninvasive approach for cancer assessment, including identification of tumor-specific mutations and methylation with a limit of detection around 50 fM.³⁷¹ Also, in another recent example, Lee *et al.* developed a multiplexed LSPR biosensing platform based on probing antibody–antigen interactions on single gold nanoparticles to detect protein biomarker of various cancers with detection levels down to ~ 10 fM for certain proteins in serum conditions.³⁷² While the detectable concentrations in these cases are quite low and likely enabled from the fact that the measurements are carried out on individual nanoparticles, translating these LSPR sensing technologies into clinical diagnostics will probably benefit from the ensemble-averaged measurement strategies discussed above (especially the virus and exosome diagnostic platforms) as the key detection capabilities will be distinguishing marker concentrations suggestive of disease from concentrations associated with normal controls.

In addition to measurements conducted on single nanoparticles, several interesting experiments have been designed whereby conformational changes in nucleic acid structures have been detected on the basis of how these conformational changes influence the gap distance between two nucleic acid-functionalized nanoparticles and hence affect the plasmonic response. Morimura *et al.* utilized this approach to measure conformational changes in DNA structure associated with binding to protein transcription factors.³⁷³ Subtle changes in gap distance have also been detected by studying ionic strength-dependent changes in DNA structure.³⁷⁴ Nguyen *et al.* also utilized plasmonic coupling to detect RNA splicing events on account of changes in RNA folding and assembly as well as pharmacological inhibition of the splicing event.³⁷⁵ In a particularly intriguing example of biointerfacial science principles, Chen *et al.* measured time-dependent fluctuations in the gap distance between DNA-functionalized nanoparticles adsorbed onto a fluid lipid membrane in order to determine how DNA tether properties (*e.g.*, length and number of strands) affect tether stiffness and conformational flexibility.³⁷⁶ As such, there is excellent potential for continuing to explore nanoplasmonic sensors for biointerfacial science applications involving nucleic acids.

8. Conclusions and outlook

The recent developments described in this review demonstrate the growing utility of nanoplasmonic sensors for applications across the biointerfacial sciences. These capabilities primarily arise from the small sensing volume and short electromagnetic field decay length or penetration depth which is on the same length scale as many medically important biomacromolecules. This feature makes nanoplasmonic sensors ideal for tracking shape and conformational changes of deformable mesoscale biomacromolecules (*e.g.*, lipid vesicles, protein aggregates) at the sensing substrate. However, despite the apparent success and attractiveness of nanoplasmonic biosensors in this direction,

there are several general considerations that must be taken into account in order to fully exploit the potential of nanoplasmonic sensors moving forward.

The first issue is the fabrication of nanoplasmonic substrates towards establishing standardized measurement platforms. It is clear that nanoplasmonic sensing platforms with well-controlled fabrication standards and measurement sensitivities would be advantageous for many researchers, especially those in the biointerfacial sciences who may not have technical expertise in nanofabrication. However, at present, most research groups fabricate their own sensing substrates. While this can be perceived as an advantage since each group has the flexibility to develop tunable or customizable plasmonic sensing platforms with the best sensing performance for specific applications of interest, it gives rise to great variability between different measurement platforms developed by different groups, both in terms of sensing format and corresponding measurement readouts. As a result, quantitative responses from different platforms cannot be practically compared in many cases. While this is less consequential in application-specific studies, it is more so in fundamental studies because developing a general knowledge of biointerfacial science topics is a largely collective effort that requires the integration of findings from across different research groups. Measurement standards for nanoplasmonic sensors would facilitate the building of a common knowledge base and stimulate more active discussion across groups. For example, surface-sensitive measurement techniques such as the QCM-D instrument have become largely standardized due to commercial instruments such as the Biolin Scientific Q-Sense instrument series with standardized 5 MHz AT-cut quartz crystal sensors that possess well-defined measurement sensitivities.³⁷⁷ Commercial LSPR sensors for research applications (Insplorion AB) and point-of-care applications (LamdaGen) are beginning to emerge so there is promise in this direction, albeit continued attention is needed in order to translate this promise into established measurement standards.^{378,379} Indeed, a standardized approach to the fabrication of nanoplasmonic substrates, which produces sensors of a standard format with clearly-defined sensing capabilities, is an important factor that could stimulate the growth of nanoplasmonic sensors for studying the biointerfacial sciences, in terms of both the number of users and the range of applications. At the same time, developing scalable strategies to produce nanoplasmonic sensing substrates remains an important goal on the materials science side. For LSPR-based sensors, an optimal strategy will likely involve some combination of nanofabrication directly on the surface together with colloidal templating to define the nanoparticle shape. Controlling the orientation of the immobilized nanostructures is particularly important in order to ensure well-defined spectral signatures so relatively simple structures like spheres and disks are preferable. In order to enhance measurement reproducibility, the presence of a thin dielectric coating on top of the nanoplasmonic sensing array is another favorable step to provide physical stability and also open the door to a wide range of surface functionalization possibilities. On the other hand, for EOT-based sensors, the key challenge is to identify a fabrication route that enables large-scale

patterning at affordable costs. Based on the available methods, template stripping is probably the most attractive, currently available method because it enables making a large number of sensor substrates to be made from a single master template. Here again, the presence of dielectric coatings on the metallic nanohole surfaces further enables surface functionalization and this is emerging as a common theme for both LSPR- and EOT-based nanoplasmonic sensors—the capability to interface sensing substrates with biologically relevant surface functionalization strategies.

The second issue relates to the collection of nanoplasmonic sensor data and its interpretation. While nanoplasmonic sensors have been widely utilized, one growing question involves asking whether such advanced measurement capabilities are needed or if a simpler, more conventional measurement approach would suffice. Indeed, the high bulk refractive index sensitivity of SPR sensors is commonly cited in this regard and has led to questions about why one might be interested in using nanoplasmonic sensors instead. From a detection perspective, such questions are reasonable but, at the same time, they also fail to capture the potential that lies ahead for integrating nanoplasmonic sensors with nanofabrication capabilities and integrated functions such as flow-through sensing. Moreover, as nanoplasmonic sensor applications extend beyond detection towards more advanced applications such as adsorption studies and conformational analysis, the analytical models used to interpret measurement data need to be extended. While there has been some progress in the recent years, more concerted effort in this direction would greatly aid the field and provide researchers with a set of tools for not only collecting data but also analyzing data. To this end, the future prospects for LSPR-based sensors are probably farther ahead than those of EOT-based sensors due to the differences in the spectral signatures of the two sensing strategies. On the whole, the EOT optical phenomenon results in more complex spectral signatures than the LSPR optical phenomenon, although this complexity also creates more opportunities for detailed analysis in the long term. Analytical models that address these issues would improve our knowledge of biomacromolecular processes occurring at solid-liquid interfaces, offering a highly surface-sensitive optical characterization tool to complement optical sensor techniques with longer penetration depths (*e.g.*, SPR) as well as acoustic sensor techniques (*e.g.*, QCM-D). Such promise highlights the potential of nanoplasmonic sensors across the biointerfacial sciences, including newly demonstrated applications such as DNA sequencing³⁸⁰ and nucleic acid structural switches.³⁶⁹

As seen throughout this review article, nanoplasmonic sensors are revealing new insights into the dynamic behavior of biomacromolecules at solid-liquid interfaces and leading to innovations for clinical diagnostics and pharmaceutical drug evaluation. Ultimately, continued progress in this field will be stimulated by the fertilization of ideas across the biointerfacial sciences and nanoplasmonic sensor communities, with a key focus on utilizing these advanced measurement capabilities to answer scientifically important questions and address key technical needs.

Acknowledgements

This work was supported by the National Research Foundation of Singapore through a Competitive Research Programme grant (NRF-CRP10-2012-07) and a Proof-of-Concept grant (NRF2015NRF-POC0001-19) as well as Nanyang Technological University through a start-up grant (M4080751.070). The authors would like to thank their colleagues and collaborators for discussions that helped motivate this work as well as the anonymous Reviewers who offered many excellent suggestions. The authors would also like to acknowledge the assistance of Mr Zackary Gromko in compiling information about different nanoplasmonic sensing strategies.

References

- 1 P. Kukura, H. Ewers, C. Müller, A. Renn, A. Helenius and V. Sandoghdar, *Nat. Methods*, 2009, **6**, 923–927.
- 2 D. L. Rupert, C. Lässer, M. Eldh, S. Block, V. P. Zhdanov, J. Lotvall, M. Bally and F. Höök, *Anal. Chem.*, 2014, **86**, 5929–5936.
- 3 J. Andrecka, K. M. Spillane, J. Ortega-Arroyo and P. Kukura, *ACS Nano*, 2013, **7**, 10662–10670.
- 4 W. P. Hall, J. Modica, J. Anker, Y. Lin, M. Mrksich and R. P. Van Duyne, *Nano Lett.*, 2011, **11**, 1098–1105.
- 5 X. Zhu, J. Li, H. He, M. Huang, X. Zhang and S. Wang, *Biosens. Bioelectron.*, 2015, **74**, 113–133.
- 6 R. Viswambari Devi, M. Doble and R. S. Verma, *Biosens. Bioelectron.*, 2015, **68**, 688–698.
- 7 A. W. Martinez, S. T. Phillips, G. M. Whitesides and E. Carrilho, *Anal. Chem.*, 2010, **82**, 3–10.
- 8 W. Zhou, X. Gao, D. Liu and X. Chen, *Chem. Rev.*, 2015, **115**, 10575–10636.
- 9 A. Qureshi, Y. Gurbuz and J. H. Niazi, *Sens. Actuators, B*, 2012, **171–172**, 62–76.
- 10 S. Geschwindner, J. F. Carlsson and W. Knecht, *Sensors*, 2012, **12**, 4311–4323.
- 11 A. Gonçalves, A. Pedro, F. Santos, L. Martins, C. Maia, J. Queiroz and L. Passarinha, *Molecules*, 2014, **19**, 12461.
- 12 R. Macarron, M. N. Banks, D. Bojanic, D. J. Burns, D. A. Cirovic, T. Garyantes, D. V. S. Green, R. P. Hertzberg, W. P. Janzen, J. W. Paslay, U. Schopfer and G. S. Sittampalam, *Nat. Rev. Drug Discovery*, 2011, **10**, 188–195.
- 13 F. Long, A. Zhu and H. Shi, *Sensors*, 2013, **13**, 13928.
- 14 R. Hurk and S. Evoy, *Sensors*, 2015, **15**, 14045.
- 15 X. Cetó, N. H. Voelcker and B. Prieto-Simón, *Biosens. Bioelectron.*, 2016, **79**, 608–626.
- 16 K. E. Sapsford, C. Bradburne, J. B. Delehanty and I. L. Medintz, *Mater. Today*, 2008, **11**, 38–49.
- 17 E. B. Bahadır and M. K. Sezginçtürk, *Anal. Biochem.*, 2015, **478**, 107–120.
- 18 E. K. Sackmann, A. L. Fulton and D. J. Beebe, *Nature*, 2014, **507**, 181–189.
- 19 G. Luka, A. Ahmadi, H. Najjaran, E. Alocilja, M. DeRosa, K. Wolthers, A. Malki, H. Aziz, A. Althani and M. Hoorfar, *Sensors*, 2015, **15**, 29783.
- 20 L. Nicu and T. Leïchlé, *J. Appl. Phys.*, 2008, **104**, 111101.
- 21 L. Yuan, Q. Yu, D. Li and H. Chen, *Macromol. Biosci.*, 2011, **11**, 1031–1040.
- 22 Q. Yu, L. K. Ista, R. Gu, S. Zauscher and G. P. Lopez, *Nanoscale*, 2016, **8**, 680–700.
- 23 C. Blaszykowski, S. Sheikh and M. Thompson, *Chem. Soc. Rev.*, 2012, **41**, 5599–5612.
- 24 C. Blaszykowski, S. Sheikh and M. Thompson, *Biomater. Sci.*, 2015, **3**, 1335–1370.
- 25 R. Ogaki and M. Foss, *Langmuir*, 2014, **30**, 7014–7023.
- 26 Q. Yu, Y. Zhang, H. Wang, J. Brash and H. Chen, *Acta Biomater.*, 2011, **7**, 1550–1557.
- 27 D. Li, Q. Zheng, Y. Wang and H. Chen, *Polym. Chem.*, 2014, **5**, 14–24.
- 28 O. Tokel, F. Inci and U. Demirci, *Chem. Rev.*, 2014, **114**, 5728–5752.
- 29 J. A. Goode, J. V. H. Rushworth and P. A. Millner, *Langmuir*, 2015, **31**, 6267–6276.
- 30 B. Kasemo, *Surf. Sci.*, 2002, **500**, 656–677.
- 31 F. Höök, B. Kasemo, M. Grunze and S. Zauscher, *ACS Nano*, 2008, **2**, 2428–2436.
- 32 A. Mashaghi, S. Mashaghi, I. Reviakine, R. M. Heeren, V. Sandoghdar and M. Bonn, *Chem. Soc. Rev.*, 2014, **43**, 887–900.
- 33 S. Löfås, *Handbook of Biosensors and Biochips*, 2007.
- 34 C. Keller and B. Kasemo, *Biophys. J.*, 1998, **75**, 1397–1402.
- 35 Y. Wu, H. Ma, D. Gu and J. A. He, *RSC Adv.*, 2015, **5**, 64520–64525.
- 36 N.-J. Cho, C. W. Frank, B. Kasemo and F. Höök, *Nat. Protoc.*, 2010, **5**, 1096–1106.
- 37 P. Bingen, G. Wang, N. F. Steinmetz, M. Rodahl and R. P. Richter, *Anal. Chem.*, 2008, **80**, 8880–8890.
- 38 I. Reviakine, F. F. Rossetti, A. N. Morozov and M. Textor, *J. Chem. Phys.*, 2005, **122**, 204711.
- 39 I. Reviakine, D. Johannsmann and R. P. Richter, *Anal. Chem.*, 2011, **83**, 8838–8848.
- 40 C. Grunewald, M. Schmutde, C. N. Noufele, C. Graf and T. Risse, *Anal. Chem.*, 2015, **87**, 10642–10649.
- 41 A. L. Olsson, I. R. Quevedo, D. He, M. Basnet and N. Tufenkji, *ACS Nano*, 2013, **7**, 7833–7843.
- 42 I. Reviakine, M. Gallego, D. Johannsmann and E. Tellechea, *J. Chem. Phys.*, 2012, **136**, 084702.
- 43 E. Tellechea, D. Johannsmann, N. F. Steinmetz, R. P. Richter and I. Reviakine, *Langmuir*, 2009, **25**, 5177–5184.
- 44 C. O'Sullivan and G. Guilbault, *Biosens. Bioelectron.*, 1999, **14**, 663–670.
- 45 K. A. Marx, *Biomacromolecules*, 2003, **4**, 1099–1120.
- 46 J. Homola, *Chem. Rev.*, 2008, **108**, 462–493.
- 47 J. Fang, C. Ren, T. Zhu, K. Wang, Z. Jiang and Y. Ma, *Analyst*, 2015, **140**, 1323–1336.
- 48 J. Fang, P. Wang, X. Du and D.-M. Zhu, *J. Phys. Chem. C*, 2009, **113**, 16121–16127.
- 49 J. Homola, S. S. Yee and G. Gauglitz, *Sens. Actuators, B*, 1999, **54**, 3–15.
- 50 A. Abbas, M. J. Linman and Q. Cheng, *Biosens. Bioelectron.*, 2011, **26**, 1815–1824.

- 51 E. Reimhult, C. Larsson, B. Kasemo and F. Höök, *Anal. Chem.*, 2004, **76**, 7211–7220.
- 52 E. Reimhult, M. Zäch, F. Höök and B. Kasemo, *Langmuir*, 2006, **22**, 3313–3319.
- 53 M. Piliarik and V. Sandoghdar, *Nat. Commun.*, 2014, **5**, 4495.
- 54 J. Ortega Arroyo, J. Andrecka, K. M. Spillane, N. Billington, Y. Takagi, J. R. Sellers and P. Kukura, *Nano Lett.*, 2014, **14**, 2065–2070.
- 55 A. G. Brolo, *Nat. Photonics*, 2012, **6**, 709–713.
- 56 A. B. Dahlin, N. J. Wittenberg, F. Höök and S.-H. Oh, *Nanophotonics*, 2013, **2**, 83–101.
- 57 M.-C. Estevez, M. A. Otte, B. Sepulveda and L. M. Lechuga, *Anal. Chim. Acta*, 2014, **806**, 55–73.
- 58 K. A. Willets and R. P. Van Duyne, *Annu. Rev. Phys. Chem.*, 2007, **58**, 267–297.
- 59 E. Hutter and J. H. Fendler, *Adv. Mater.*, 2004, **16**, 1685–1706.
- 60 H. Liu and P. Lalanne, *Nature*, 2008, **452**, 728–731.
- 61 T. W. Ebbesen, H. J. Lezec, H. F. Ghaemi, T. Thio and P. A. Wolff, *Nature*, 1998, **391**, 667–669.
- 62 L. Martín-Moreno, F. J. García-Vidal, H. J. Lezec, K. M. Pellerin, T. Thio, J. B. Pendry and T. W. Ebbesen, *Phys. Rev. Lett.*, 2001, **86**, 1114–1117.
- 63 J. N. Anker, W. P. Hall, O. Lyandres, N. C. Shah, J. Zhao and R. P. Van Duyne, *Nat. Mater.*, 2008, **7**, 442–453.
- 64 J. Langer, S. M. Novikov and L. M. Liz-Marzán, *Nanotechnology*, 2015, **26**, 322001.
- 65 B. Sepúlveda, P. C. Angelomé, L. M. Lechuga and L. M. Liz-Marzán, *Nano Today*, 2009, **4**, 244–251.
- 66 S. Unser, I. Bruzas, J. He and L. Sagle, *Sensors*, 2015, **15**, 15684.
- 67 M. Sriram, K. Zong, S. Vivekchand and J. Gooding, *Sensors*, 2015, **15**, 25774.
- 68 M. R. Jones, K. D. Osberg, R. J. Macfarlane, M. R. Langille and C. A. Mirkin, *Chem. Rev.*, 2011, **111**, 3736–3827.
- 69 M. Jahn, S. Patze, I. J. Hidi, R. Knipper, A. I. Radu, A. Muhligh, S. Yuksel, V. Peksa, K. Weber, T. Mayerhofer, D. Cialla-May and J. Popp, *Analyst*, 2016, **141**, 756–793.
- 70 M. E. Stewart, C. R. Anderton, L. B. Thompson, J. Maria, S. K. Gray, J. A. Rogers and R. G. Nuzzo, *Chem. Rev.*, 2008, **108**, 494–521.
- 71 E. M. Larsson, S. Syrenova and C. Langhammer, *Nanophotonics*, 2012, **1**, 249–266.
- 72 L. Polavarapu and L. M. Liz-Marzán, *Phys. Chem. Chem. Phys.*, 2013, **15**, 5288–5300.
- 73 W. W. Zheng, H. C. Chiamori, G. L. Liu, L. W. Lin and F. F. Chen, *Nanotechnol. Rev.*, 2012, **1**, 213–233.
- 74 P. Strobbia, E. Languirand and B. M. Cullum, *OPTICE*, 2015, **54**, 100902.
- 75 N. Michieli, B. Kalinic, C. Scian, T. Cesca and G. Mattei, *Biosens. Bioelectron.*, 2015, **65**, 346–353.
- 76 A. B. Dahlin, *Analyst*, 2015, **140**, 4748–4759.
- 77 G. A. Lopez, M. Estevez, M. Soler and L. M. Lechuga, *Nanophotonics*, 2017, **6**, 123–136.
- 78 B. Špačková, P. Wrobel, M. Bocková and J. Homola, *Proc. IEEE*, 2016, **104**, 2380–2408.
- 79 J. Bingham, W. P. Hall and R. Van Duyne, in *Nanoplasmonic Sensors*, ed. A. Dmitriev, Springer, New York, 2012, ch. 2, pp. 29–58.
- 80 V. Claudio, A. B. Dahlin and T. J. Antosiewicz, *J. Phys. Chem. C*, 2014, **118**, 6980–6988.
- 81 W. L. Barnes, A. Dereux and T. W. Ebbesen, *Nature*, 2003, **424**, 824–830.
- 82 B. Liedberg, C. Nylander and I. Lunström, *Sens. Actuators*, 1983, **4**, 299–304.
- 83 D. K. Kambhampati and W. Knoll, *Curr. Opin. Colloid Interface Sci.*, 1999, **4**, 273–280.
- 84 W. Knoll, *Annu. Rev. Phys. Chem.*, 1998, **49**, 569–638.
- 85 S. Ekgasit, C. Thammacharoen, F. Yu and W. Knoll, *Appl. Spectrosc.*, 2005, **59**, 661–667.
- 86 M. Piliarik and J. Homola, *Opt. Express*, 2009, **17**, 16505–16517.
- 87 A. Liu, J. Peng and G. Li, *Appl. Phys. Lett.*, 2014, **104**, 211103.
- 88 D. L. Rupert, G. V. Shelke, G. Emilsson, V. Claudio, S. Block, C. Lässer, A. Dahlin, J. O. Lötvall, M. Bally and V. P. Zhdanov, *Anal. Chem.*, 2016, **88**, 9980–9988.
- 89 H. H. Nguyen, J. Park, S. Kang and M. Kim, *Sensors*, 2015, **15**, 10481–10510.
- 90 S. G. Patching, *Biochim. Biophys. Acta, Biomembr.*, 2014, **1838**, 43–55.
- 91 H. Šipová and J. Homola, *Anal. Chim. Acta*, 2013, **773**, 9–23.
- 92 F. Mazzotta, T. W. Johnson, A. B. Dahlin, J. Shaver, S.-H. Oh and F. Höök, *ACS Photonics*, 2015, **2**, 256–262.
- 93 L. Guo, J. A. Jackman, H.-H. Yang, P. Chen, N.-J. Cho and D.-H. Kim, *Nano Today*, 2015, **10**, 213–239.
- 94 M. Svedendahl, S. Chen, A. Dmitriev and M. Kall, *Nano Lett.*, 2009, **9**, 4428–4433.
- 95 M. I. Stockman, *Science*, 2015, **348**, 287–288.
- 96 E. Martinsson, M. M. Shahjamali, K. Enander, F. Boey, C. Xue, D. Aili and B. Liedberg, *J. Phys. Chem. C*, 2013, **117**, 23148–23154.
- 97 A. B. Dahlin, *Plasmonic Biosensors: An Integrated View of Refractometric Detection*, Ios Press, 2012.
- 98 O. Kedem, A. Vaskevich and I. Rubinstein, *J. Phys. Chem. C*, 2014, **118**, 8227–8244.
- 99 J. S. Wilson, *Sensor Technology Handbook*, Elsevier, 2004.
- 100 J. Homola and M. Piliarik, in *Surface Plasmon Resonance Based Sensors*, Springer, 2006, pp. 45–67.
- 101 K. A. Willets and R. P. Van Duyne, *Annu. Rev. Phys. Chem.*, 2007, **58**, 267–297.
- 102 G. Mie, *Ann. Phys.*, 1908, **330**, 377–445.
- 103 C. L. Nehl and J. H. Hafner, *J. Mater. Chem.*, 2008, **18**, 2415–2419.
- 104 U. Kreibig and M. Vollmer, *Optical Properties of Metal Clusters*, Springer Science & Business Media, 2013.
- 105 S. Link and M. A. El-Sayed, *J. Phys. Chem. B*, 1999, **103**, 8410–8426.
- 106 C. F. Bohren and D. R. Huffman, *Absorption and Scattering of Light by Small Particles*, John Wiley & Sons, 2008.
- 107 A. J. Haes and R. P. Van Duyne, *Anal. Bioanal. Chem.*, 2004, **379**, 920–930.
- 108 P. K. Jain, K. S. Lee, I. H. El-Sayed and M. A. El-Sayed, *J. Phys. Chem. B*, 2006, **110**, 7238.

- 109 M. Piliarik, P. Kvasnicka, N. Galler, J. R. Krenn and J. Homola, *Opt. Express*, 2011, **19**, 9213–9220.
- 110 P. R. West, S. Ishii, G. V. Naik, N. K. Emani, V. M. Shalae and A. Boltasseva, *Laser Photonics Rev.*, 2010, **4**, 795–808.
- 111 M. W. Knight, N. S. King, L. Liu, H. O. Everitt, P. Nordlander and N. J. Halas, *ACS Nano*, 2013, **8**, 834–840.
- 112 W. Li, K. Ren and J. Zhou, *TrAC, Trends Anal. Chem.*, 2016, **80**, 486–494.
- 113 K. L. Kelly, E. Coronado, L. L. Zhao and G. C. Schatz, *J. Phys. Chem. B*, 2003, **107**, 668–677.
- 114 L. Feuz, M. P. Jonsson and F. Höök, *Nano Lett.*, 2012, **12**, 873–879.
- 115 M. W. Knight, Y. Wu, J. B. Lassiter, P. Nordlander and N. J. Halas, *Nano Lett.*, 2009, **9**, 2188–2192.
- 116 E. Martinsson, M. A. Otte, M. M. Shahjamali, B. Sepulveda and D. Aili, *J. Phys. Chem. C*, 2014, **118**, 24680–24687.
- 117 M. A. Otte and B. Sepulveda, in *Nanoplasmonic Sensors*, Springer, 2012, pp. 317–331.
- 118 T. J. Antosiewicz and T. Tarkowski, *ACS Photonics*, 2015, **2**, 1732–1738.
- 119 J. Li, C. Chen, L. Lagae and P. Van Dorpe, *J. Phys. Chem. C*, 2015, **119**, 29116–29122.
- 120 T. Felicia, B. Monica, B. Lucian and A. Simion, *Nanotechnology*, 2007, **18**, 255702.
- 121 S. Kinge, M. Crego-Calama and D. N. Reinhoudt, *Chem-PhysChem*, 2008, **9**, 20–42.
- 122 A. Friedl, P. Adam, S. Leshkov and J. Homola, *J. Nanosci. Nanotechnol.*, 2011, **11**, 2528–2532.
- 123 P. A. Mosier-Boss and S. H. Lieberman, *Appl. Spectrosc.*, 1999, **53**, 862–873.
- 124 T. G. Habteyes, S. Dhuey, E. Wood, D. Gargas, S. Cabrini, P. J. Schuck, A. P. Alivisatos and S. R. Leone, *ACS Nano*, 2012, **6**, 5702–5709.
- 125 T. Siegfried, Y. Ekinci, O. J. Martin and H. Sigg, *ACS Nano*, 2013, **7**, 2751–2757.
- 126 L. Guo, Y. Huang, Y. Kikutani, Y. Tanaka, T. Kitamori and D.-H. Kim, *Lab Chip*, 2011, **11**, 3299–3304.
- 127 Y. Lu, G. L. Liu and L. P. Lee, *Nano Lett.*, 2005, **5**, 5–9.
- 128 C. L. Haynes and R. P. Van Duyne, *J. Phys. Chem. B*, 2001, **105**, 5599–5611.
- 129 H. Fredriksson, Y. Alaverdyan, A. Dmitriev, C. Langhammer, D. S. Sutherland, M. Zäch and B. Kasemo, *Adv. Mater.*, 2007, **19**, 4297–4302.
- 130 F. A. A. Nugroho, R. Frost, T. J. Antosiewicz, J. Fritzsche, E. M. Larsson Langhammer and C. Langhammer, *ACS Sens.*, 2016, **2**, 119–127.
- 131 J. Henzie, J. Lee, M. H. Lee, W. Hasan and T. W. Odom, *Annu. Rev. Phys. Chem.*, 2009, **60**, 147–165.
- 132 M. A. Otte, M. C. Estevez, L. G. Carrascosa, A. B. Gonzalez-Guerrero, L. M. Lechuga and B. Sepulveda, *J. Phys. Chem. C*, 2011, **115**, 5344–5351.
- 133 J. Jose, L. R. Jordan, T. W. Johnson, S. H. Lee, N. J. Wittenberg and S.-H. Oh, *Adv. Funct. Mater.*, 2013, **23**, 2812–2820.
- 134 C. Langhammer, E. M. Larsson, B. Kasemo and I. Zoric, *Nano Lett.*, 2010, **10**, 3529–3538.
- 135 S. Szunerits and R. Boukherroub, *Chem. Commun.*, 2012, **48**, 8999–9010.
- 136 S. Szunerits, S. Ghodbane, J. Niedziółka-Jönsson, E. Galopin, F. Klauser, A. Akjouj, Y. Pennec, B. Djafari-Rouhani, R. Boukherroub and D. Steinmüller-Nethl, *J. Phys. Chem. C*, 2010, **114**, 3346–3353.
- 137 E. Galopin, L. Touahir, J. Niedziółka-Jönsson, R. Boukherroub, A. C. Gouget-Laemmel, J.-N. Chazalviel, F. Ozanam and S. Szunerits, *Biosens. Bioelectron.*, 2010, **25**, 1199–1203.
- 138 S. Gao, N. Koshizaki, E. Koyama, H. Tokuhisa, T. Sasaki, J.-K. Kim, Y. Cho, D.-S. Kim and Y. Shimizu, *Anal. Chem.*, 2009, **81**, 7703–7712.
- 139 S. Gao, N. Koshizaki, H. Tokuhisa, E. Koyama, T. Sasaki, J. K. Kim, J. Ryu, D. S. Kim and Y. Shimizu, *Adv. Funct. Mater.*, 2010, **20**, 78–86.
- 140 S. Gao and N. Koshizaki, *Anal. Bioanal. Chem.*, 2011, **399**, 91–101.
- 141 L. Guo, G. Chen and D.-H. Kim, *Anal. Chem.*, 2010, **82**, 5147–5153.
- 142 A. B. Dahlin, M. P. Jonsson and F. Höök, *Adv. Mater.*, 2008, **20**, 1436–1442.
- 143 A. Degiron, H. Lezec, N. Yamamoto and T. Ebbesen, *Opt. Commun.*, 2004, **239**, 61–66.
- 144 C. Genet and T. Ebbesen, *Nature*, 2007, **445**, 39–46.
- 145 Y. Lin, Y. Zou, Y. Mo, J. Guo and R. G. Lindquist, *Sensors*, 2010, **10**, 9397–9406.
- 146 J. García, D. Monzón-Hernández, J. Manríquez and E. Bustos, *Opt. Mater.*, 2016, **51**, 208–212.
- 147 A. Gowri and V. Sai, *Sens. Actuators, B*, 2016, **230**, 536–543.
- 148 O. Kedem, A. Vaskevich and I. Rubinstein, *J. Phys. Lett.*, 2011, **2**, 1223–1226.
- 149 Y. Lin, Y. Zou and R. G. Lindquist, *Biomed. Opt. Express*, 2011, **2**, 478–484.
- 150 K. Huang, W. Pan, J. Zhu, J. Li, N. Gao, C. Liu, L. Ji, E. Yu and J. Kang, *Sci. Rep.*, 2015, **5**, 18331.
- 151 X. Zhang, M. A. Young, O. Lyandres and R. P. Van Duyne, *J. Am. Chem. Soc.*, 2005, **127**, 4484–4489.
- 152 B. Sciacca and T. M. Monro, *Langmuir*, 2014, **30**, 946–954.
- 153 M. Sanders, Y. Lin, J. Wei, T. Bono and R. G. Lindquist, *Biosens. Bioelectron.*, 2014, **61**, 95–101.
- 154 A. B. Dahlin, J. O. Tegenfeldt and F. Höök, *Anal. Chem.*, 2006, **78**, 4416–4423.
- 155 J. M. Bingham, J. N. Anker, L. E. Kreno and R. P. Van Duyne, *J. Am. Chem. Soc.*, 2010, **132**, 17358–17359.
- 156 K. M. Mayer and J. H. Hafner, *Chem. Rev.*, 2011, **111**, 3828–3857.
- 157 R. E. Messersmith, G. J. Nusz and S. M. Reed, *J. Phys. Chem. C*, 2013, **117**, 26725–26733.
- 158 J. Becker, A. Trügler, A. Jakab, U. Hohenester and C. Sönnichsen, *Plasmonics*, 2010, **5**, 161–167.
- 159 N. Nath and A. Chilkoti, *Anal. Chem.*, 2004, **76**, 5370–5378.
- 160 A. B. Dahlin and M. P. Jonsson, in *Nanoplasmonic Sensors*, Springer, 2012, pp. 231–265.
- 161 P. Chen, N. T. Tran, X. Wen, Q. Xiong and B. Liedberg, *ACS Sens.*, 2017, **2**, 235–242.
- 162 J. E. Millstone, S. Park, K. L. Shuford, L. Qin, G. C. Schatz and C. A. Mirkin, *J. Am. Chem. Soc.*, 2005, **127**, 5312–5313.

- 163 S. Link, M. Mohamed and M. El-Sayed, *J. Phys. Chem. B*, 1999, **103**, 3073–3077.
- 164 W. Ni, X. Kou, Z. Yang and J. Wang, *ACS Nano*, 2008, **2**, 677–686.
- 165 M. P. Raphael, J. A. Christodoulides, S. P. Mulvaney, M. M. Miller, J. P. Long and J. M. Byers, *Anal. Chem.*, 2012, **84**, 1367–1373.
- 166 J. A. Ruemmele, W. P. Hall, L. K. Ruvuna and R. P. Van Duyne, *Anal. Chem.*, 2013, **85**, 4560–4566.
- 167 K. Hamamoto, R. Micheletto, M. Oyama, A. Ali Umar, S. Kawai and Y. Kawakami, *J. Opt. A: Pure Appl. Opt.*, 2006, **8**, 268.
- 168 K. Lodewijks, W. Van Roy, G. Borghs, L. Lagae and P. Van Dorpe, *Nano Lett.*, 2012, **12**, 1655–1659.
- 169 V. Kravets, F. Schedin, R. Jalil, L. Britnell, R. Gorbachev, D. Ansell, B. Thackray, K. Novoselov, A. Geim and A. V. Kabashin, *Nat. Mater.*, 2013, **12**, 304–309.
- 170 C. Lambertz, A. Martos, A. Henkel, A. Neiser, T.-T. Kliesch, A. Janshoff, P. Schuille and C. Sönnichsen, *Nano Lett.*, 2016, **16**, 3540–3544.
- 171 J. Fritzsche, D. Albinsson, M. Fritzsche, T. J. Antosiewicz, F. Westerlund and C. Langhammer, *Nano Lett.*, 2016, **16**, 7857–7864.
- 172 N. Fairbairn, A. Christofidou, A. G. Kanaras, T. A. Newman and O. L. Muskens, *Phys. Chem. Chem. Phys.*, 2013, **15**, 4163–4168.
- 173 X. Wang, Y. Cui and J. Irudayaraj, *ACS Nano*, 2015, **9**, 11924–11932.
- 174 D. Zopf, J. Jatschka, A. Dathe, N. Jahr, W. Fritzsche and O. Stranik, *Biosens. Bioelectron.*, 2016, **81**, 287–293.
- 175 Y. Cui, X. Wang, W. Ren, J. Liu and J. Irudayaraj, *ACS Nano*, 2016, **10**, 3132–3143.
- 176 L. S. Jung, C. T. Campbell, T. M. Chinowsky, M. N. Mar and S. S. Yee, *Langmuir*, 1998, **14**, 5636–5648.
- 177 J. Junesch, G. Emilsson, K. Xiong, S. Kumar, T. Sannomiya, H. Pace, J. Voros, S.-H. Oh, M. Bally and A. B. Dahlin, *Nanoscale*, 2015, **7**, 15080–15085.
- 178 J. Li, J. Ye, C. Chen, Y. Li, N. Verellen, V. V. Moshchalkov, L. Lagae and P. Van Dorpe, *ACS Photonics*, 2015, **2**, 425–431.
- 179 C. Langhammer, Z. Yuan, I. Zoric and B. Kasemo, *Nano Lett.*, 2006, **6**, 833–838.
- 180 I. Zorić, M. Zäch, B. Kasemo and C. Langhammer, *ACS Nano*, 2011, **5**, 2535–2546.
- 181 G. F. Bertsch and R. A. Broglia, *Oscillations in Finite Quantum Systems*, Cambridge University Press, 1994.
- 182 L. Landau, E. Lifshitz and L. Pitaevskii, *Electrodynamics of Continuous Media*, 1984.
- 183 J. A. Jackman, V. P. Zhdanov and N.-J. Cho, *Langmuir*, 2014, **30**, 9494–9503.
- 184 A. Christ, T. Zentgraf, S. Tikhodeev, N. Gippius, J. Kuhl and H. Giessen, *Phys. Rev. B: Condens. Matter Mater. Phys.*, 2006, **74**, 155435.
- 185 D. Nau, A. Schönhardt, C. Bauer, A. Christ, T. Zentgraf, J. Kuhl, M. Klein and H. Giessen, *Phys. Rev. Lett.*, 2007, **98**, 133902.
- 186 C. Rockstuhl, F. Lederer, T. Zentgraf and H. Giessen, *Appl. Phys. Lett.*, 2007, **91**, 151109.
- 187 R. Gordon, D. Sinton, K. L. Kavanagh and A. G. Brolo, *Acc. Chem. Res.*, 2008, **41**, 1049–1057.
- 188 T. Sannomiya, O. Scholder, K. Jefimovs, C. Hafner and A. B. Dahlin, *Small*, 2011, **7**, 1653–1663.
- 189 S. G. Tikhodeev, A. Yablonskii, E. Muljarov, N. Gippius and T. Ishihara, *Phys. Rev. B: Condens. Matter Mater. Phys.*, 2002, **66**, 045102.
- 190 W. Kuang, A. English, Z.-C. Chang, M.-H. Shih, W. B. Knowlton, J. Lee, W. L. Hughes and B. Yurke, *Opt. Commun.*, 2010, **283**, 4090–4093.
- 191 D. Pacifici, H. J. Lezec, L. A. Sweatlock, R. J. Walters and H. A. Atwater, *Opt. Express*, 2008, **16**, 9222–9238.
- 192 A. Agrawal, T. Matsui, Z. V. Vardeny and A. Nahata, *Opt. Express*, 2008, **16**, 6267–6273.
- 193 J. Bravo-Abad, A. Fernandez-Dominguez, F. Garcia-Vidal and L. Martin-Moreno, *Phys. Rev. Lett.*, 2007, **99**, 203905.
- 194 F. Przybilla, C. Genet and T. W. Ebbesen, *Opt. Express*, 2012, **20**, 4697–4709.
- 195 N. C. Lindquist, P. Nagpal, K. M. McPeak, D. J. Norris and S.-H. Oh, *Rep. Prog. Phys.*, 2012, **75**, 036501.
- 196 B. Brian, B. Sepúlveda, Y. Alaverdyan, L. M. Lechuga and M. Käll, *Opt. Express*, 2009, **17**, 2015–2023.
- 197 S. H. Lee, K. C. Bantz, N. C. Lindquist, S.-H. Oh and C. L. Haynes, *Langmuir*, 2009, **25**, 13685–13693.
- 198 H. Im, N. C. Lindquist, A. Lesuffleur and S.-H. Oh, *ACS Nano*, 2010, **4**, 947–954.
- 199 H. Im, N. J. Wittenberg, N. C. Lindquist and S.-H. Oh, *J. Mater. Res.*, 2012, **27**, 663–671.
- 200 J. Junesch, T. Sannomiya and A. B. Dahlin, *ACS Nano*, 2012, **6**, 10405–10415.
- 201 Y. Ikenoya, M. Susa, J. Shi, Y. Nakamura, A. B. Dahlin and T. Sannomiya, *J. Phys. Chem. C*, 2013, **117**, 6373–6382.
- 202 A. B. Dahlin, M. Mapar, K. Xiong, F. Mazzotta, F. Höök and T. Sannomiya, *Adv. Opt. Mater.*, 2014, **2**, 556–564.
- 203 A. E. Cetin, D. Etezadi, B. C. Galarreta, M. P. Busson, Y. Eksioğlu and H. Altug, *ACS Photonics*, 2015, **2**, 1167–1174.
- 204 M. P. Jonsson, A. B. Dahlin, L. Feuz, S. Petronis and F. Höök, *Anal. Chem.*, 2010, **82**, 2087–2094.
- 205 J. Junesch and T. Sannomiya, *ACS Appl. Mater. Interfaces*, 2014, **6**, 6322–6331.
- 206 H. Im, S. H. Lee, N. J. Wittenberg, T. W. Johnson, N. C. Lindquist, P. Nagpal, D. J. Norris and S.-H. Oh, *ACS Nano*, 2011, **5**, 6244–6253.
- 207 F. Eftekhari, C. Escobedo, J. Ferreira, X. Duan, E. M. Girotto, A. G. Brolo, R. Gordon and D. Sinton, *Anal. Chem.*, 2009, **81**, 4308–4311.
- 208 J. Braun, B. Gompf, G. Kobiela and M. Dressel, *Phys. Rev. Lett.*, 2009, **103**, 203901.
- 209 K. Xiong, G. Emilsson and A. B. Dahlin, *Analyst*, 2016, **141**, 3803–3810.
- 210 Y. Eksioğlu, A. E. Cetin and J. Petráček, *Plasmonics*, 2015, 1–6.
- 211 A. E. Cetin, M. Dršata, Y. Eksioğlu and J. Petráček, *Plasmonics*, 2016, 1–7.
- 212 A. Cetin, M. Dršata, Y. Eksioğlu and J. Petráček, *Effect of lattice geometry on optical transmission through subwavelength*

- nanohole arrays*, The 10th International Congress on Advanced Electromagnetic Materials in Microwaves and Optics – Metamaterials, 2016, pp. 280–282.
- 213 J.-F. Masson, M.-P. Murray-Methot and L. S. Live, *Analyst*, 2010, **135**, 1483–1489.
- 214 S. Kumar, S. Cherukulappurath, T. W. Johnson and S.-H. Oh, *Chem. Mater.*, 2014, **26**, 6523–6530.
- 215 S. H. Lee, T. W. Johnson, N. C. Lindquist, H. Im, D. J. Norris and S. H. Oh, *Adv. Funct. Mater.*, 2012, **22**, 4439–4446.
- 216 P. Nagpal, N. C. Lindquist, S.-H. Oh and D. J. Norris, *Science*, 2009, **325**, 594–597.
- 217 J. H. Park, P. Nagpal, S.-H. Oh and D. J. Norris, *Appl. Phys. Lett.*, 2012, **100**, 081105.
- 218 T. Thio, H. Lezec and T. Ebbesen, *Phys. B*, 2000, **279**, 90–93.
- 219 A. Dhawan and J. F. Muth, *J. Mater. Sci. Eng. B*, 2008, **149**, 237–241.
- 220 X. Lan, B. Cheng, Q. Yang, J. Huang, H. Wang, Y. Ma, H. Shi and H. Xiao, *Sens. Actuators, B*, 2014, **193**, 95–99.
- 221 A. Peer and R. Biswas, *Nanoscale*, 2016, **8**, 4657–4666.
- 222 C. Escobedo, *Lab Chip*, 2013, **13**, 2445–2463.
- 223 C. Escobedo, A. G. Brolo, R. Gordon and D. Sinton, *Anal. Chem.*, 2010, **82**, 10015–10020.
- 224 C. Escobedo, A. G. Brolo, R. Gordon and D. Sinton, *Nano Lett.*, 2012, **12**, 1592–1596.
- 225 A. Barik, L. M. Otto, D. Yoo, J. Jose, T. W. Johnson and S.-H. Oh, *Nano Lett.*, 2014, **14**, 2006–2012.
- 226 A. De Leebeeck, L. S. Kumar, V. de Lange, D. Sinton, R. Gordon and A. G. Brolo, *Anal. Chem.*, 2007, **79**, 4094–4100.
- 227 J. P. Monteiro, L. B. Carneiro, M. M. Rahman, A. G. Brolo, M. J. Santos, J. Ferreira and E. M. Girotto, *Sens. Actuators, B*, 2013, **178**, 366–370.
- 228 M. Couture, Y. Liang, H.-P. P. Richard, R. Faid, W. Peng and J.-F. Masson, *Nanoscale*, 2013, **5**, 12399–12408.
- 229 M. Couture, K. K. Ray, H.-P. Poirier-Richard, A. Crofton and J.-F. Masson, *ACS Sens.*, 2016, **1**, 287–294.
- 230 K. Nakamoto, R. Kurita, O. Niwa, T. Fujii and M. Nishida, *Nanoscale*, 2011, **3**, 5067–5075.
- 231 K. Nakamoto, R. Kurita and O. Niwa, *Anal. Chem.*, 2012, **84**, 3187–3191.
- 232 N. C. Lindquist, T. W. Johnson, J. Jose, L. M. Otto and S. H. Oh, *Ann. Phys.*, 2012, **524**, 687–696.
- 233 M. Couture, L. S. Live, A. Dhawan and J.-F. Masson, *Analyst*, 2012, **137**, 4162–4170.
- 234 J. Junesch and T. Sannomiya, *J. Phys. Lett.*, 2013, **5**, 247–252.
- 235 T.-Y. Chang, M. Huang, A. A. Yanik, H.-Y. Tsai, P. Shi, S. Aksu, M. F. Yanik and H. Altug, *Lab Chip*, 2011, **11**, 3596–3602.
- 236 H. Im, A. Lesuffleur, N. C. Lindquist and S.-H. Oh, *Anal. Chem.*, 2009, **81**, 2854–2859.
- 237 S. H. Lee, N. C. Lindquist, N. J. Wittenberg, L. R. Jordan and S.-H. Oh, *Lab Chip*, 2012, **12**, 3882–3890.
- 238 S. T. Seiler, I. S. Rich and N. C. Lindquist, *Nanotechnology*, 2016, **27**, 184001.
- 239 A. E. Cetin, A. F. Coskun, B. C. Galarreta, M. Huang, D. Herman, A. Ozcan and H. Altug, *Light: Sci. Appl.*, 2014, **3**, e122.
- 240 A. F. Coskun, A. E. Cetin, B. C. Galarreta, D. A. Alvarez, H. Altug and A. Ozcan, *Sci. Rep.*, 2014, **4**, 6789.
- 241 S. Quint and C. Pacholski, *J. Mater. Chem. C*, 2014, **2**, 7632–7638.
- 242 Z. S. Ballard, D. Shir, A. Bhardwaj, S. Bazargan, S. Sathianathan and A. Ozcan, *ACS Nano*, 2017, **11**, 2266–2274.
- 243 Y. Shen, J. Zhou, T. Liu, Y. Tao, R. Jiang, M. Liu, G. Xiao, J. Zhu, Z.-K. Zhou and X. Wang, *Nat. Commun.*, 2013, **4**, 2381.
- 244 J. Li, J. Ye, C. Chen, L. Hermans, N. Verellen, J. Ryken, H. Jans, W. Van Roy, V. V. Moshchalkov, L. Lagae and P. Van Dorpe, *Adv. Opt. Mater.*, 2015, **3**, 176–181.
- 245 M. A. Otte, B. Sepulveda, W. Ni, J. P. Juste, L. M. Liz-Marzán and L. M. Lechuga, *ACS Nano*, 2009, **4**, 349–357.
- 246 S. J. Zalyubovskiy, M. Bogdanova, A. Deinega, Y. Lozovik, A. D. Pris, K. H. An, W. P. Hall and R. A. Potyrailo, *J. Opt. Soc. Am. A*, 2012, **29**, 994–1002.
- 247 A. J. Haes and R. P. Van Duyne, *J. Am. Chem. Soc.*, 2002, **124**, 10596–10604.
- 248 B. Špačková and J. Homola, *Opt. Express*, 2013, **21**, 27490–27502.
- 249 E. Reimhult and F. Höök, *Sensors*, 2015, **15**, 1635–1675.
- 250 F. Rusmini, Z. Zhong and J. Feijen, *Biomacromolecules*, 2007, **8**, 1775–1789.
- 251 H. Wang, R. Yang, L. Yang and W. Tan, *ACS Nano*, 2009, **3**, 2451–2460.
- 252 J.-Y. Byun, Y.-B. Shin, T. Li, J.-H. Park, D.-M. Kim, D.-H. Choi and M.-G. Kim, *Chem. Commun.*, 2013, **49**, 9497–9499.
- 253 G. L. Kenausis, J. Vörös, D. L. Elbert, N. Huang, R. Hofer, L. Ruiz-Taylor, M. Textor, J. A. Hubbell and N. D. Spencer, *J. Phys. Chem. B*, 2000, **104**, 3298–3309.
- 254 L. Ruiz-Taylor, T. Martin, F. Zaugg, K. Witte, P. Indermuhle, S. Nock and P. Wagner, *Proc. Natl. Acad. Sci. U. S. A.*, 2001, **98**, 852–857.
- 255 F. Mazzotta, G. Wang, C. Häggglund, F. Höök and M. P. Jonsson, *Biosens. Bioelectron.*, 2010, **26**, 1131–1136.
- 256 J. H. Park, T. N. Sut, J. A. Jackman, A. R. Ferhan, B. K. Yoon and N.-J. Cho, *Phys. Chem. Chem. Phys.*, 2017, **19**, 8854–8865.
- 257 M. Svedendahl, R. Verre and M. Käll, *Light: Sci. Appl.*, 2014, **3**, e220.
- 258 K. Fujiwara, H. Watarai, H. Itoh, E. Nakahama and N. Ogawa, *Anal. Bioanal. Chem.*, 2006, **386**, 639–644.
- 259 J. Wei, Z. Zeng and Y. Lin, *Biosensors and Biodetection: Methods and Protocols: Optical-Based Detectors*, 2017, vol. 1, pp. 1–14.
- 260 M. Soler, M.-C. Estevez, R. Villar-Vazquez, J. I. Casal and L. M. Lechuga, *Anal. Chim. Acta*, 2016, **930**, 31–38.
- 261 K. Glasmästar, C. Larsson, F. Höök and B. Kasemo, *J. Colloid Interface Sci.*, 2002, **246**, 40–47.
- 262 F. Persson, J. Fritzsche, K. U. Mir, M. Modesti, F. Westerlund and J. O. Tegenfeldt, *Nano Lett.*, 2012, **12**, 2260–2265.
- 263 M. D. Malinsky, K. L. Kelly, G. C. Schatz and R. P. Van Duyne, *J. Am. Chem. Soc.*, 2001, **123**, 1471–1482.
- 264 A. A. Volkert and A. J. Haes, *Analyst*, 2014, **139**, 21–31.
- 265 A. Das, J. Zhao, G. C. Schatz, S. G. Sligar and R. P. Van Duyne, *Anal. Chem.*, 2009, **81**, 3754–3759.

- 266 W. P. Hall, J. N. Anker, Y. Lin, J. Modica, M. Mrksich and R. P. Van Duyne, *J. Am. Chem. Soc.*, 2008, **130**, 5836–5837.
- 267 W. P. Hall, S. N. Ngatia and R. P. Van Duyne, *J. Phys. Chem. C*, 2011, **115**, 1410–1414.
- 268 C. R. Yonzon, E. Jeoung, S. Zou, G. C. Schatz, M. Mrksich and R. P. Van Duyne, *J. Am. Chem. Soc.*, 2004, **126**, 12669–12676.
- 269 A. G. Brolo, R. Gordon, B. Leathem and K. L. Kavanagh, *Langmuir*, 2004, **20**, 4813–4815.
- 270 J.-C. Yang, J. Ji, J. M. Hogle and D. N. Larson, *Nano Lett.*, 2008, **8**, 2718–2724.
- 271 H. Im, J. N. Sutherland, J. A. Maynard and S.-H. Oh, *Anal. Chem.*, 2012, **84**, 1941–1947.
- 272 M. Bhagawati, C. You and J. Piehler, *Anal. Chem.*, 2013, **85**, 9564–9571.
- 273 M. P. Raphael, J. A. Christodoulides, J. B. Delehanty, J. P. Long and J. M. Byers, *Biophys. J.*, 2013, **105**, 602–608.
- 274 J. Ferreira, M. J. L. Santos, M. M. Rahman, A. G. Brolo, R. Gordon, D. Sinton and E. M. Girotto, *J. Am. Chem. Soc.*, 2009, **131**, 436–437.
- 275 S. S. Acimović, M. A. Ortega, V. Sanz, J. Berthelot, J. L. Garcia-Cordero, J. Renger, S. J. Maerkl, M. P. Kreuzer and R. Quidant, *Nano Lett.*, 2014, **14**, 2636–2641.
- 276 R. Frost, C. Wadell, A. Hellman, S. Molander, S. Svedhem, M. Persson and C. Langhammer, *ACS Sens.*, 2016, **1**, 798–806.
- 277 R. Frost, C. Langhammer and T. Cedervall, *Nanoscale*, 2017, **9**, 3620–3628.
- 278 N. Bhalla, M. Di Lorenzo, G. Pula and P. Estrela, *Sci. Rep.*, 2015, **5**, 8687.
- 279 J. R. L. Guerreiro, V. E. Bochenkov, K. Runager, H. Aslan, M. Dong, J. J. Enghild, V. De Freitas, M. G. Ferreira Sales and D. S. Sutherland, *ACS Sens.*, 2016, **1**, 258–264.
- 280 J. R. L. Guerreiro, M. Frederiksen, V. E. Bochenkov, V. De Freitas, M. G. Ferreira Sales and D. S. Sutherland, *ACS Nano*, 2014, **8**, 7958–7967.
- 281 D. Zhang, Y. Lu, Q. Zhang, Y. Yao, S. Li, H. Li, S. Zhuang, J. Jiang, G. L. Liu and Q. Liu, *Sens. Actuators, B*, 2015, **221**, 341–349.
- 282 J. He, M. Boegli, I. Bruzas, W. Lum and L. Sagle, *Anal. Chem.*, 2015, **87**, 11407–11414.
- 283 C. Escobedo, S. Vincent, A. I. K. Choudhury, J. Campbell, A. G. Brolo, D. Sinton and R. Gordon, *J. Micromech. Microeng.*, 2011, **21**, 115001.
- 284 N. C. Lindquist, A. Lesuffleur, H. Im and S.-H. Oh, *Lab Chip*, 2009, **9**, 382–387.
- 285 J. Lazar, R. R. Rosencrantz, L. Elling and U. Schnakenberg, *Anal. Chem.*, 2016, **88**, 9590–9596.
- 286 T. Nagatsuka, H. Uzawa, K. Sato, S. Kondo, M. Izumi, K. Yokoyama, I. Ohsawa, Y. Seto, P. Neri, H. Mori, Y. Nishida, M. Saito and E. Tamiya, *ACS Appl. Mater. Interfaces*, 2013, **5**, 4173–4180.
- 287 H. M. Hiep, H. Yoshikawa and E. Tamiya, *Anal. Chem.*, 2010, **82**, 1221–1227.
- 288 J. N. Anker, W. P. Hall, M. P. Lambert, P. T. Velasco, M. Mrksich, W. L. Klein and R. P. Van Duyne, *J. Phys. Chem. C*, 2009, **113**, 5891–5894.
- 289 X. R. Cheng, G. Q. Wallace, F. Lagugné-Labarthe and K. Kerman, *ACS Appl. Mater. Interfaces*, 2015, **7**, 4081–4088.
- 290 G. Bellapadrona, A. B. Tesler, D. Grünstein, L. H. Hossain, R. Kikkeri, P. H. Seeberger, A. Vaskevich and I. Rubinstein, *Anal. Chem.*, 2012, **84**, 232–240.
- 291 H. Kitano, Y. Takahashi, K. Mizukami and K. Matsuura, *Colloids Surf., B*, 2009, **70**, 91–97.
- 292 C. Yonzon and R. P. Van Duyne, *Localized and propagating surface plasmon resonance sensors: A study using carbohydrate binding protein*, Materials Research Society Symposium Proceedings, 2005, vol. 876E, pp. R7.3.1–R7.3.6.
- 293 S. Chah, M. R. Hammond and R. N. Zare, *Chem. Biol.*, 2005, **12**, 323–328.
- 294 J. H. Teichroeb, J. A. Forrest and L. W. Jones, *Eur. Phys. J. E: Soft Matter Biol. Phys.*, 2008, **26**, 411–415.
- 295 S. R. Beeram and F. P. Zamborini, *J. Phys. Chem. C*, 2011, **115**, 7364–7371.
- 296 L. Feuz, M. P. Jonsson and F. Höök, *Nano Lett.*, 2012, **12**, 873–879.
- 297 L. Feuz, P. Jönsson, M. P. Jonsson and F. Höök, *ACS Nano*, 2010, **4**, 2167–2177.
- 298 M. E. Stewart, N. H. Mack, V. Malyarchuk, J. A. N. T. Soares, T.-W. Lee, S. K. Gray, R. G. Nuzzo and J. A. Rogers, *Proc. Natl. Acad. Sci. U. S. A.*, 2006, **103**, 17143–17148.
- 299 A. Vázquez-Guardado, A. Smith, W. Wilson, J. Ortega, J. M. Perez and D. Chanda, *Opt. Express*, 2016, **24**, 25785–25796.
- 300 X. Zhao, M. M.-K. Wong, S.-K. Chiu and S. W. Pang, *Biosens. Bioelectron.*, 2015, **74**, 799–807.
- 301 Y. Wang, A. Kar, A. Paterson, K. Kourentzi, H. Le, P. Ruchhoeft, R. Willson and J. Bao, *ACS Photonics*, 2014, **1**, 241–245.
- 302 D.-K. Kim, S. M. Yoo, T. J. Park, H. Yoshikawa, E. Tamiya, J. Y. Park and S. Y. Lee, *Anal. Chem.*, 2011, **83**, 6215–6222.
- 303 B.-R. Oh, P. Chen, R. Nidetz, W. McHugh, J. Fu, T. P. Shanley, T. T. Cornell and K. Kurabayashi, *ACS Sensors*, 2016, **1**, 941–948.
- 304 L. Pang, G. M. Hwang, B. Slutsky and Y. Fainman, *Appl. Phys. Lett.*, 2007, **91**, 123112.
- 305 G. Cappi, F. M. Spiga, Y. Moncada, A. Ferretti, M. Beyeler, M. Bianchessi, L. Decosterd, T. Buclin and C. Guiducci, *Anal. Chem.*, 2015, **87**, 5278–5285.
- 306 A. Dahlin, M. Zäch, T. Rindzevicius, M. Käll, D. S. Sutherland and F. Höök, *J. Am. Chem. Soc.*, 2005, **127**, 5043–5048.
- 307 A. B. Dahlin, M. P. Jonsson and F. Höök, *Adv. Mater.*, 2008, **20**, 1436–1442.
- 308 K. Kumar, A. B. Dahlin, T. Sannomiya, S. Kaufmann, L. Isa and E. Reimhult, *Nano Lett.*, 2013, **13**, 6122–6129.
- 309 M. P. Jonsson, P. Jönsson, A. B. Dahlin and F. Höök, *Nano Lett.*, 2007, **7**, 3462–3468.
- 310 M. P. Jonsson, P. Jönsson and F. Höök, *Anal. Chem.*, 2008, **80**, 7988–7995.
- 311 E. M. Larsson, M. E. M. Edvardsson, C. Langhammer, I. Zorić and B. Kasemo, *Rev. Sci. Instrum.*, 2009, **80**, 125105.
- 312 G. H. Zan, J. A. Jackman, S.-O. Kim and N.-J. Cho, *Small*, 2014, **10**, 4828–4832.
- 313 E. Oh, J. A. Jackman, S. Yorulmaz, V. P. Zhdanov, H. Lee and N.-J. Cho, *Langmuir*, 2015, **31**, 771–781.

- 314 J. A. Jackman, B. Spackova, E. Linarydy, M. C. Kim, B. K. Yoon, J. Homola and N.-J. Cho, *Chem. Commun.*, 2016, **52**, 76–79.
- 315 M. Dacic, J. A. Jackman, S. Yorulmaz, V. P. Zhdanov, B. Kasemo and N.-J. Cho, *Langmuir*, 2016, **32**, 6486–6495.
- 316 J. A. Jackman, S. Yorulmaz Avsar, A. R. Ferhan, D. Li, J. H. Park, V. P. Zhdanov and N.-J. Cho, *Anal. Chem.*, 2016, **89**, 1102–1109.
- 317 A. R. Ferhan, J. A. Jackman and N.-J. Cho, *Anal. Chem.*, 2016, **88**, 12524–12531.
- 318 A. R. Ferhan, J. A. Jackman and N.-J. Cho, *Phys. Chem. Chem. Phys.*, 2017, **19**, 2131–2139.
- 319 C.-Y. Chen, S. S. Hinman, J. Duan and Q. Cheng, *Anal. Chem.*, 2014, **86**, 11942–11945.
- 320 J. Witos, G. Russo, S.-K. Ruokonen and S. K. Wiedmer, *Langmuir*, 2017, **33**, 1066–1076.
- 321 A. R. Ferhan, J. A. Jackman and N.-J. Cho, *Anal. Chem.*, 2017, DOI: 10.1021/acs.analchem.7b00370.
- 322 E. Reimhult, F. Höök and B. Kasemo, *Langmuir*, 2003, **19**, 1681–1691.
- 323 G. K. Joshi, K. A. Smith, M. A. Johnson and R. Sardar, *J. Phys. Chem. C*, 2013, **117**, 26228–26237.
- 324 R. Tero, T. Ujihara and T. Urisu, *Langmuir*, 2008, **24**, 11567–11576.
- 325 A. B. Dahlin, P. Jönsson, M. P. Jonsson, E. Schmid, Y. Zhou and F. Höök, *ACS Nano*, 2008, **2**, 2174–2182.
- 326 H. Im, N. J. Wittenberg, A. Lesuffleur, N. C. Lindquist and S.-H. Oh, *Chem. Sci.*, 2010, **1**, 688–696.
- 327 A. Lesuffleur, L. Kwan Seop, N. C. Lindquist, I. Hyungsoon, A. E. Warrington, M. Rodriguez and S.-H. Oh, *Plasmonic nanohole arrays for label-free kinetic biosensing in a lipid membrane environment*, Engineering in Medicine and Biology Society, EMBC 2009 Annual International Conference of the IEEE, 2009, pp. 1481–1484.
- 328 N. J. Wittenberg, H. Im, T. W. Johnson, X. Xu, A. E. Warrington, M. Rodriguez and S.-H. Oh, *ACS Nano*, 2011, **5**, 7555–7564.
- 329 N. J. Wittenberg, H. Im, X. Xu, B. Wootla, J. Watzlawik, A. E. Warrington, M. Rodriguez and S.-H. Oh, *Anal. Chem.*, 2012, **84**, 6031–6039.
- 330 I. Bruzas, S. Unser, S. Yazdi, E. Ringe and L. Sagle, *Anal. Chem.*, 2016, **88**, 7968–7974.
- 331 W. J. Galush, S. A. Shelby, M. J. Mulvihill, A. Tao, P. Yang and J. T. Groves, *Nano Lett.*, 2009, **9**, 2077–2082.
- 332 H.-J. Wu, J. Henzie, W.-C. Lin, C. Rhodes, Z. Li, E. Sartorel, J. Thorner, P. Yang and J. T. Groves, *Nat. Methods*, 2012, **9**, 1189–1191.
- 333 L. J. Sherry, S.-H. Chang, G. C. Schatz, R. P. Van Duyne, B. J. Wiley and Y. Xia, *Nano Lett.*, 2005, **5**, 2034–2038.
- 334 E. T. Castellana, R. C. Gamez and D. H. Russell, *J. Am. Chem. Soc.*, 2011, **133**, 4182–4185.
- 335 H. Fawcett, M. S. Ünlü and J. H. Connor, *ACS Infect. Dis.*, 2016, **2**, 378–381.
- 336 H. Im, H. Shao, R. Weissleder, C. M. Castro and H. Lee, *Expert Rev. Mol. Diagn.*, 2015, **15**, 725–733.
- 337 A. A. Yanik, M. Huang, O. Kamohara, A. Artar, T. W. Geisbert, J. H. Connor and H. Altug, *Nano Lett.*, 2010, **10**, 4962–4969.
- 338 M. Huang, B. C. Galarreta, A. E. Cetin and H. Altug, *Lab Chip*, 2013, **13**, 4841–4847.
- 339 F. Inci, O. Tokel, S. Wang, U. A. Gurkan, S. Tasoglu, D. R. Kuritzkes and U. Demirci, *ACS Nano*, 2013, **7**, 4733–4745.
- 340 J.-H. Lee, B.-C. Kim, B.-K. Oh and J.-W. Choi, *Nanomedicine*, 2013, **9**, 1018–1026.
- 341 T. J. Park, S. J. Lee, D.-K. Kim, N. S. Heo, J. Y. Park and S. Y. Lee, *Talanta*, 2012, **89**, 246–252.
- 342 H. Yu, K. Kim, K. Ma, W. Lee, J.-W. Choi, C.-O. Yun and D. Kim, *Biosens. Bioelectron.*, 2013, **41**, 249–255.
- 343 J. A. Jackman, E. Linarydy, D. Yoo, J. Seo, W. B. Ng, D. J. Klemme, N. J. Wittenberg, S.-H. Oh and N.-J. Cho, *Small*, 2016, **12**, 1159–1166.
- 344 H. Im, H. Shao, Y. I. Park, V. M. Peterson, C. M. Castro, R. Weissleder and H. Lee, *Nat. Biotechnol.*, 2014, **32**, 490–495.
- 345 K. Liang, F. Liu, J. Fan, D. Sun, C. Liu, C. J. Lyon, D. W. Bernard, Y. Li, K. Yokoi and M. H. Katz, *Nat. Biomed. Eng.*, 2017, **1**, 0021.
- 346 A. A. Yanik, M. Huang, A. Artar, T.-Y. Chang and H. Altug, *Appl. Phys. Lett.*, 2010, **96**, 021101.
- 347 F. Inci, C. Filippini, M. Baday, M. O. Ozen, S. Calamak, N. G. Durmus, S. Wang, E. Hanhauser, K. S. Hobbs and F. Juillard, *Proc. Natl. Acad. Sci. U. S. A.*, 2015, **112**, E4354–E4363.
- 348 L. Zhu, K. Wang, J. Cui, H. Liu, X. Bu, H. Ma, W. Wang, H. Gong, C. Lausted, L. Hood, G. Yang and Z. Hu, *Anal. Chem.*, 2014, **86**, 8857–8864.
- 349 A. Lesuffleur, H. Im, N. C. Lindquist, K. S. Lim and S.-H. Oh, *Opt. Express*, 2008, **16**, 219–224.
- 350 M. Soler, A. Belushkin, A. Cavallini, C. Kebbi-Beghdadi, G. Greub and H. Altug, *Biosens. Bioelectron.*, 2017, **94**, 560–567.
- 351 J. A. Jackman, J. Lee and N.-J. Cho, *Small*, 2016, **12**, 1133–1139.
- 352 K. E. Fong and L.-Y. L. Yung, *Nanoscale*, 2013, **5**, 12043–12071.
- 353 A. Charrier, N. Candoni, N. Liachenko and F. Thibaudau, *Biosens. Bioelectron.*, 2007, **22**, 1881–1886.
- 354 R. A. Reynolds, C. A. Mirkin and R. L. Letsinger, *J. Am. Chem. Soc.*, 2000, **122**, 3795–3796.
- 355 T. A. Taton, G. Lu and C. A. Mirkin, *J. Am. Chem. Soc.*, 2001, **123**, 5164–5165.
- 356 S. J. Oldenburg, C. C. Genick, K. A. Clark and D. A. Schultz, *Anal. Biochem.*, 2002, **309**, 109–116.
- 357 A. D. McFarland and R. P. Van Duyne, *Nano Lett.*, 2003, **3**, 1057–1062.
- 358 J. I. Chen, Y. Chen and D. S. Ginger, *J. Am. Chem. Soc.*, 2010, **132**, 9600–9601.
- 359 T. Li, X. Wu, F. Liu and N. Li, *Analyst*, 2017, **142**, 248–256.
- 360 C. Cao, J. Zhang, X. Wen, S. L. Dodson, N. T. Dao, L. M. Wong, S. Wang, S. Li, A. T. A. Phan and Q. Xiong, *ACS Nano*, 2013, **7**, 7583–7591.
- 361 Y. Zhao, Y.-K. He, J. Zhang, F.-B. Wang, K. Wang and X.-H. Xia, *Chem. Commun.*, 2014, **50**, 5480–5483.
- 362 S. Qiu, F. Zhao, O. Zenasni, J. Li and W.-C. Shih, *ACS Appl. Mater. Interfaces*, 2016, **8**, 29968–29976.
- 363 F. Zhao, S. Qiu and W.-C. Shih, *Nanoplasmonic sensing on DNA topological structure functionalized nanoporous gold*

- disks, 2016 International Conference on Optical MEMS and Nanophotonics (OMN), 2016, pp. 1–2.
- 364 S. Qiu, F. Zhao, G. M. Santos and W.-C. Shih, *Plasmonic biosensor for label-free G-quadruplexes detection*, SPIE BiOS, 2016, pp. 97250F–97250F-4.
- 365 A. Rapisarda, N. Giambianco and G. Marletta, *J. Colloid Interface Sci.*, 2017, **487**, 141–148.
- 366 L. Frolov, A. Dix, Y. Tor, A. B. Tesler, Y. Chaikin, A. Vaskevich and I. Rubinstein, *Anal. Chem.*, 2013, **85**, 2200–2207.
- 367 G. K. Joshi, S. Deitz-McElyea, M. Johnson, S. Mali, M. Korc and R. Sardar, *Nano Lett.*, 2014, **14**, 6955–6963.
- 368 G. K. Joshi, S. Deitz-McElyea, T. Liyanage, K. Lawrence, S. Mali, R. Sardar and M. Korc, *ACS Nano*, 2015, **9**, 11075–11089.
- 369 Y. Tian, L. Zhang, J. Shen, L. Wu, H. He, D. L. Ma, C. H. Leung, W. Wu, Q. Fan and W. Huang, *Small*, 2016, **12**, 2913–2920.
- 370 P. Zhan, P. K. Dutta, P. Wang, G. Song, M. Dai, S.-X. Zhao, Z.-G. Wang, P. Yin, W. Zhang and B. Ding, *ACS Nano*, 2017, **11**, 1172–1179.
- 371 A. H. Nguyen and S. J. Sim, *Biosens. Bioelectron.*, 2015, **67**, 443–449.
- 372 J. U. Lee, A. H. Nguyen and S. J. Sim, *Biosens. Bioelectron.*, 2015, **74**, 341–346.
- 373 H. Morimura, S.-I. Tanaka, H. Ishitobi, T. Mikami, Y. Kamachi, H. Kondoh and Y. Inouye, *ACS Nano*, 2013, **7**, 10733–10740.
- 374 L. Lermusiaux, V. Maillard and S. B. Bidault, *ACS Nano*, 2015, **9**, 978–990.
- 375 A. H. Nguyen, J. U. Lee and S. J. Sim, *Nanoscale*, 2016, **8**, 4599–4607.
- 376 T. Chen, Y. Hong and B. R. M. Reinhard, *Nano Lett.*, 2015, **15**, 5349–5357.
- 377 M. Rodahl and B. Kasemo, *Rev. Sci. Instrum.*, 1996, **67**, 3238–3241.
- 378 D. Gerion, presented in part at the SPIE BiOS, 2012.
- 379 R. T. Hill, *Wiley Interdiscip. Rev.: Nanomed. Nanobiotechnol.*, 2015, **7**, 152–168.
- 380 M. Belkin, S.-H. Chao, M. P. Jonsson, C. Dekker and A. Aksimentiev, *ACS Nano*, 2015, **9**, 10598–10611.